UNIVERSITÀ DEGLI STUDI DI PADOVA

Dipartimento di Fisica e Astronomia

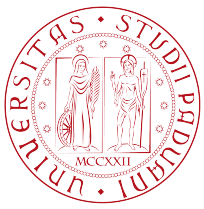

Tesi di Laurea Magistrale in Fisica

Analytical and numerical models and first operations on the negative ion source NIO1

Relatore:
Dr. Gianluigi Serianni

Correlatori:
Dr. Marco Cavenago
Dr. Pierluigi Veltri

Controrelatore:
Dr. Enrico Fagotti

Candidato:
Marta Cazzador
matricola: 1058270

7 Ottobre 2014 - A. A. 2013-2014

Abstract

The development and optimization of neutral beam injectors (NBI) as heating systems of fusion plasmas are crucial in the perspective of the experimental reactor ITER under realization in Cadarache (France). In this framework the recently installed negative ion source NIO1, resulting from a collaboration between Consorzio RFX and INFN-LNL (Legnaro, Italy), can provide a test bench for source and beam optics optimization thanks to its high modularity.

In this thesis fast tools, able to model the main physical phenomena taking place inside the NIO1 source and accelerating column, have been developed in order to qualitatively describe the response of the whole system to variations in the external operation parameters; comparison of the results was possible with the experimental findings obtained during the first ever NIO1 operation, showing a good agreement between the model and the experiment.

In detail in this thesis, after an introduction on the basic concepts of thermonuclear fusion and neutral beam injectors, a detailed description of the negative ion source NIO1 is given, together with the commissioning tests on the source itself and some of the first experimental results.

An analytic model for the RF coupling is proposed, which gives an estimate of the power coupling efficiency as a function of the plasma temperature and density and allows dimensioning the matching circuit used to couple RF power supply to the plasma. Plasma heating is due to local and non local effects, which have been introduced in the model by the use of an effective collision frequency, defined as the sum of the electron collision frequencies with ions and neutrals and a stochastic collision frequency.

A model for the profile of plasma parameters, which considers the electron diffusion and energy equation and a multipole magnetic confinement, has been implemented numerically for hydrogen, nitrogen and oxygen gases: the results well agree with other numerical simulations and experimental measurements.

By adopting a Monte Carlo approach, a sample of maxwellian electrons has then been evolved through the magnetic filter field in NIO1 in order to calculate the electron temperature and density as a function of the distance from the plasma grid: the simulation confirms that there is an effective electron cooling, that could be further improved by increasing the magnetic field strength.

As a last step in the experiment modelization, a hydrogen and an oxygen beam have been simulated in the case of a low current density, typical of the first operations of NIO1 without caesium. The optimal electrode potentials have been studied and the results show the necessity of an appropriate scaling in the strength of the permanent magnets when operating in hydrogen.

Sommario

In prospettiva del reattore a fusione ITER in fase di realizzazione a Cadarache (Francia), lo sviluppo e l'ottimizzazione di iniettori di fasci di neutri (NBI) come meccanismo di riscaldamento addizionale nell'ambito di plasmi fusionistici sono cruciali. In questo contesto la sorgente di ioni negativi NIO1, recentemente installata nell'ambito di una collaborazione tra Consorzio RFX e INFN-LNL di Legnaro, è un utile strumento per l'ottimizzazione della sorgente e dell'ottica del fascio grazie alla sua alta modularità.

In questa tesi sono stati sviluppati strumenti veloci in grado di modellizzare i principali fenomeni fisici che avvengono nella sorgente e nel sistema di accelerazione di NIO1, con l'obiettivo di dare una descrizione qualitativa della risposta dell'intero sistema a variazioni nei parametri sperimentali; i risultati dei modelli numerici sono sati confrontati con le misure effettuate durante la prima campagna sperimentale svolta con NIO1, dimostrando un buon accordo tra modello ed esperimento.

In dettaglio in questa tesi, dopo una prima introduzione sui concetti base della fisica della fusione termonucleare e sugli iniettori di fasci di neutri, viene fornita una descrizione dettagliata di NIO1, seguita dai test eseguiti durante la messa in funzione della sorgente e da alcuni dei primi risultati sperimentali.

Viene poi proposto un modello analitico per l'accoppiamento RF, che dà una stima dell'efficienza nell'accoppiamento della potenza al plasma in funzione di densità e temperatura elettronica e permette di dimensionare i componenti del circuito di accoppiamento. Il riscaldamento del plasma è dovuto ad effetti locali e non locali, che sono stati modellizzati mediante una frequenza di collisione efficace, definita come la somma della frequenza di collisione degli elettroni con ioni e particelle neutre e una frequenza di collisione stocastica.

È stato poi implementato numericamente un modello per il calcolo del profilo dei parametri di plasma per plasmi di idrogeno, azoto e ossigeno, che considera le equazioni di diffusione e dell'energia per gli elettroni e l'effetto confinante dei multipoli magnetici: i risultati ottenuti sono in buon accordo con altre simulazioni e risultati sperimentali.

Seguendo un approccio di tipo Monte Carlo, un campione maxwelliano di elettroni è stato fatto quindi evolvere attraverso il filtro magnetico di NIO1 con l'obiettivo di calcolare la temperatura e la densità elettronica in funzione della distanza dalla plasma grid: la simulazione mostra come ci sia un efficace raffreddamento elettronico, che può essere ulteriormente migliorato aumentando l'intensità del campo magnetico.

Come ultimo passo nella modellizzazione dell'esperimento, un fascio di idrogeno e uno di ossigeno sono stati simulati in condizioni di basse densità di corrente, tipiche delle prime operazioni di NIO1 che avverranno senza cesio. Sono stati studiati i valori ottimali di tensione da applicare alle griglie e i risultati ottenuti mostrano la necessità di un appropriato riscalamento dell'intensità dei magneti quando si operi in idrogeno.

Contents

CHAPTER 1

Introduction

In recent years one of the most pressing problems has been and still is the energetic problem, that has to comply with the growing energy needs of human mankind. Several scenarios have been developed addressing the relationship between electricity demand and supply on both a regional and a global scale: studies carried out by the International Institute for Applied Systems Analysis (IIASA) show that by the year 2050, the global electricity demand can grow up to a factor 3 with respect to the present consumption [1]. Such growth in the developing world is going to put an enormous demand on primary energy resources, which cannot be sustained by the decreasing reserves of fossil fuels. Alternative energy sources have to be investigated, in particular controlled thermonuclear fusion can be a serious candidate to meet these needs because not only the fusion reactions involve light nuclides that are naturally abundant, but also the fusion process itself does not leave long-lived radioactive products and the problem of radioactive-waste disposal is much less serious than that for fission reactors.

1.1 Thermonuclear fusion

In a fusion reaction two reactant nuclei fuse into a heavier one with the release of other products: the energy comes out in the form of the kinetic energy of the product nuclei, which usually stop into the plasma or the surrounding walls (depending on products), with production of heat and possibly electricity. While a discussion of electricity production efficiency is outside the scope of this thesis, a general overview of fusion condition is necessary to understand the need for Neutral Beam Injectors and thereof the specifications of the negative ion sources.

For fusion to occur, the protons or heavier reactant nuclei (which are positively charged and naturally repulsive) must be brought close enough to overcome the electrostatic repulsion, so that the nuclear strong force helps them fuse by a quantum mechanical tunnelling process: this is possible when the nuclei are heated to very high thermonuclear temperatures, in the order of $10^7 - 10^8$ K, such that the reactants are in the plasma state.

By far the most promising fusion reaction [2] is that in which the nuclei of deuterium (^{2}H) and tritium (^{3}H) fuse to produce an alpha particle with the release of a neutron, that is:

$$^2\mathrm{H} + {}^3\mathrm{H} \longrightarrow {}^4\mathrm{He}\ (3.5\,\mathrm{MeV}) + \mathrm{n}\ (14.1\,\mathrm{MeV}) \tag{1.1}$$

with a total 17.6 MeV produced in each reaction. Deuterium is a stable isotope and constitutes the 0.015% of the total hydrogen, on the other hand tritium has a 12.3 year lifetime, so it has to be artificially produced for example from lithium:

$$\begin{aligned} \mathrm{n} + {}^6\mathrm{Li} &\longrightarrow {}^4\mathrm{He} + {}^3\mathrm{H} + 4.8\,\mathrm{MeV} \\ \mathrm{n} + {}^7\mathrm{Li} &\longrightarrow {}^4\mathrm{He} + {}^3\mathrm{H} + \mathrm{n} - 2.5\,\mathrm{MeV} \end{aligned} \tag{1.2}$$

The power balance in a thermonuclear plasma in stationary conditions can be written as:

$$p_\mathrm{H} + p_\alpha = p_\mathrm{R} + p_\mathrm{L} \tag{1.3}$$

where p_H is the power supplied to the system, p_α is the power heating due to the α particles (the neutrons produced escape from the plasma), p_R is the power lost in radiative processes (mainly bremsstrahlung) and p_L is the power lost in transport processes.

The power heating due to the α particles can be calculated by considering that the maximum thermonuclear power density in a D-T plasma is

$$p_\mathrm{f} = \frac{1}{4}\, n^2 \langle \sigma v \rangle E_\mathrm{f} \tag{1.4}$$

where n is the sum of deuterium and tritium density, $\langle \sigma v \rangle$ is the average over the particles distribution function of the cross section times the nuclei relative velocity (see Figure 1.1) and $E_\mathrm{f} = 17.6\,\mathrm{MeV}$. From this expression then it follows:

$$p_\alpha = \frac{1}{4}\, n^2 \langle \sigma v \rangle E_\alpha \tag{1.5}$$

where $E_\alpha = 3.5\,\mathrm{MeV}$. The power lost in transport processes in a plasma with uniform density n and temperature T can be written as:

$$p_\mathrm{L} = \frac{w}{\tau_\mathrm{E}} = \frac{3nT}{\tau_\mathrm{E}} \tag{1.6}$$

where the energy density w takes into account both ions and electrons and τ_E is an empirical parameter called confinement time. The ideal operation condition is the ignition, in which the losses are fully compensated by the α-particle heating: this

translates in a requirement on the product $n\,\tau_{\mathrm{E}}$ (see Figure 1.2), which is

$$n\,\tau_{\mathrm{E}} > \frac{12\,T}{\langle\sigma v\rangle\,E_\alpha} \tag{1.7}$$

where the radiation losses have been neglected. In the $10-20$ keV energy range in particular, the ignition condition becomes

$$n\,T\,\tau_{\mathrm{E}} > 3\cdot 10^{21}\,\mathrm{m}^{-3}\,\mathrm{keV\,s} \tag{1.8}$$

The ignition is the ideal operation condition for a fusion reactor, however external

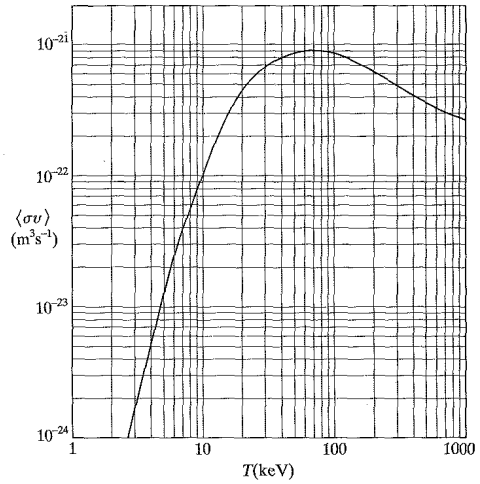

Figure 1.1: $\langle\sigma v\rangle$ for D-T reactions as a function of plasma temperature [3].

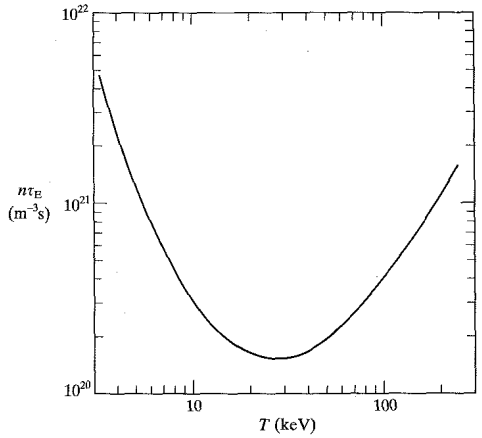

Figure 1.2: $n\,\tau_{\mathrm{E}}$ value required to obtain ignition, as a function of plasma temperature [3].

heating can be used to sustain the thermonuclear reactions provided that the total power produced exceeds the power injected into the system. A measure of the success in approaching reactor conditions is given by the ratio of the thermonuclear power produced to the heating power supplied:

$$Q = \frac{P_{\mathrm{f}}}{P_{\mathrm{H}}} \tag{1.9}$$

Ignition corresponds to $Q\to\infty$, but a $Q\geq 10$ is practically necessary to operate a fusion reactor.

The triple product in (1.8) sets a criterion that has to be satisfied by a fusion reactor: a plasma with a temperature of about 10 keV has to be confined for a sufficient amount of time at a certain density so that $n\,\tau_{\mathrm{E}} > 3\cdot 10^{20}\,\mathrm{m}^{-3}\,\mathrm{s}$. This condition can be achieved by the use of two different types of confinement:

- *Inertial confinement*: the plasma density n is maximized. A pellet of dense solid

fusion fuel is symmetrically and uniformly heated to the temperatures required for ignition by a giant laser pulse or a pulsed heavy ion beam from a particle accelerator. This intense heating creates an inward implosion of the fuel as the surface layer ablates and explodes outward: in this approach confinement is achieved by the inertia of the hot fuel that keeps it together for a finite time and the high plasma density is achieved during the fuel compression.

- *Magnetic confinement*: the confinement time τ_{E} is maximized. The hot plasma with densities in the order of $10^{19} - 10^{20}$ m^{-3} is confined by intense magnetic fields: a typical machine is the tokamak (from the russian toroidal'naya kamera s magnitnymi katushkami, which means literally toroidal chamber with magnetic coils [4]), where plasma is confined in a toroidal chamber. The principal magnetic field is the toroidal field, however this field alone does not allow confinement of the plasma: the addition of a poloidal magnetic field is necessary to have a stable equilibrium in which the plasma pressure is balanced by the magnetic forces [5]; the combination of the toroidal and the poloidal fields give rise to magnetic field lines which have a helical trajectory around the torus, which oppose to the particles drift motion towards the walls. This a promising path to developing future fusion reactors, which have to confine the plasma in a steady state for long durations. Among other magnetic configurations there are RFP (Reversed Field Pinch) [6] and the stellarator [7, 8].

1.1.1 The ITER project

One of the more explored configurations for magnetic confinement is the tokamak, in which the toroidal magnetic field B_{ϕ} is the stronger component and is generated by the current flowing in a set of coils that link the plasma. The poloidal magnetic field B_{θ} is generated by the toroidal plasma current driven by the electric field induced by transformer action in which a flux change through the torus. This is the configuration used by ITER (Latin word for "the way" or "the road"), a large-scale scientific experiment under construction in Cadarache (France) that aims to demonstrate the technological and scientific feasibility of fusion energy [9]. From 50 MW of input power, the ITER machine is designed to produce 500 MW of fusion power ($Q = 10$), the first of all fusion experiments to produce net energy.

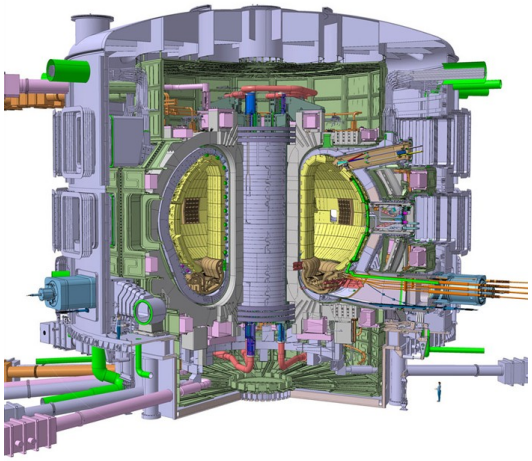

Major radius	6.2 m
Minor radius	2.0 m
Plasma current	15 MA
Toroidal field on axis	5.3 T
Discharge duration	>400 s
Energy confinement τ_E	3.7 s
Heating power	40 MW
Fusion power	500 MW
Q	10

Figure 1.3: Schematic overview (man on the bottom right for scale) and main parameters in the ITER reactor [9].

1.2 Plasma heating and neutral beam injection

For the fusion reactions to occur inside the reactor, the plasma has to be heated to temperatures in the order of 10 keV: since for a fully ionized plasma the resistivity falls with the plasma temperature as $T^{-3/2}$ [10], a simple ohmic heating using the plasma current is not sufficient. Other heating mechanisms then have to be used, among which there are:

- *Radio frequency heating*: it transfers energy from an external source to the plasma by means of electromagnetic waves with frequencies corresponding to the resonant frequencies in the magnetized plasma under consideration;
- *Neutral beam injection*: neutral beams are used since charged particles beams would be deviated from the tokamak magnetic field; conversely, energetic neutral atoms injected into a plasma travel in straight lines, but are trapped in the magnetic field when ionized through collisions with the plasma particles. In this way the plasma electrons and ions gain energy through Coulomb collisions with the injected ions, which are initially slowed and then thermalized. This is the method that will be described now in order to introduce the experiment on which this thesis is based.

In detail, the neutral beam is trapped into the plasma through the following reactions:

$$\begin{aligned} &H_b + H_p^+ \longrightarrow H_b^+ + H_p \quad \text{(charge exchange)} \\ &H_b + H_p^+ \longrightarrow H_b^+ + H_p^+ + e^- \quad \text{(ionization by ions)} \\ &H_b + e^- \longrightarrow H_b^+ + 2e^- \quad \text{(ionization by electrons)} \end{aligned} \tag{1.10}$$

where H stands for the neutral hydrogen isotope used, which can be hydrogen or deuterium, and the subscript b and p stand for beam and plasma.

The beam energy has to be significantly above the energy of the plasma particles it has to heat, and the beam has to penetrate sufficiently into the plasma to deposit its energy in the center, where the energy is lost more slowly. In order to penetrate the dense plasmas in the large future fusion devices such as ITER, the required neutral beam energy is at least 300 keV, but if one aims to use neutral beams also to drive a current in the plasma a very high energy of the order of 1 MeV or more is required [11]. At these high energies the neutralization efficiency of positive ions is too low, while in negative ion beams a neutralization efficiency of almost 60% can be achieved by regulating the gas pressure in the neutralization region (see Figure 1.4). For this reason the neutral beam in injectors aimed to heat large volume plasmas is produced by the neutralization of accelerated negative ions.

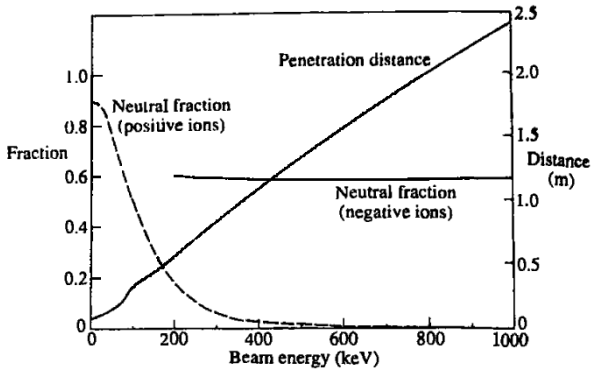

Fig. 1.4: Equilibrium neutral fraction in a deuterium beam formed from positive and negative ion beams and penetration of the neutrals in a plasma with $n = 10^{20}\mathrm{m}^{-3}$ [3].

1.3 Negative ion beams

A scheme of a typical negative ion source and of its beam acceleration system is given in Figure 1.6, where radiofrequency is used to heat the plasma, which is confined in the source by a multipolar cusp magnetic field.

Negative ion production in the source region can be achieved through two main mechanisms:

- *volume production* (Figure 1.5(a)). Hydrogen molecules are efficiently vibrationally excited by collisions with high energy electrons (E_e >20 eV)

$$\mathrm{H}_2 + e_{\mathrm{fast}} \longrightarrow \mathrm{H}_2^*(\nu) + e_{\mathrm{fast}} \tag{1.11}$$

  and negative hydrogen ions are produced by dissociative attachment of low-energy electrons (E_e <2 eV) to vibrationally excited molecules

$$\mathrm{H}_2^*(\nu) + e_{\mathrm{slow}} \longrightarrow \mathrm{H}^- + \mathrm{H}^0 \tag{1.12}$$

  The cross section for the process (1.11) is larger for highly excited states ($\nu \geq 7$) and high electron energies, on the other hand the negative ions produced by (1.12)

are easily destroyed by collisions with electrons with energies greater than 2 eV [5]. The source then has to be divided in two parts, a hotter upstream region called *driver*, where is located the main plasma heating and the electrons produce vibrationally excited molecules, and a colder downstream region called *extraction region*, where negative ions are produced and extracted. The plasma cooling can be obtained both by expansion of the source volume in the extraction region and by a transverse magnetic filter field, which reflects back the high energy electrons given their low collisionality.

- *surface production* (Figure 1.5(b)): fast atoms (H^0) or ions (H^+) are converted to H^- ions when colliding on the source walls. It has been shown that injection of caesium vapor in the source leads to a 3-10 times enhancement in H^- production [5]: this is due to the low work function of caesium (below 2 eV) that forms a thin layer on the source walls thus lowering the work function of the metal surface itself. Since the H^- ions are easily destroyed in collisions with electrons, surface production has to be localized in the extraction region, where plasma electrons are colder as noted before, in particular on the plasma grid (the first grid in the acceleration system) rear surface.

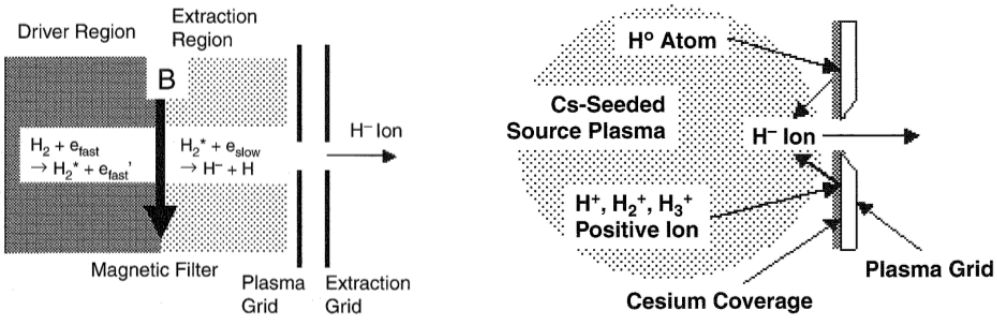

(a) Volume production. **(b)** Surface production.

Figure 1.5: H^- production mechanisms in a negative ion source [5].

The ions produced are then extracted through a multi-aperture system of circular holes, carefully designed to minimize the aberrations of each beamlet and accelerated by a grid system at increasingly higher potential, whose main components are:

- *plasma grid* (PG): grid facing the source plasma, is held at the source voltage;
- *extraction grid* (EG): the voltage drop between this grid and the PG determines the extracted current from the source;
- *grounded grid* (GG), connected to ground. The voltage drop between the PG and the GG determines the ions final energy;
- *repeller* (REP): additional electrode at a slightly positive voltage whose function

is to suppress the backstreaming of positive ions created after the acceleration column.

In high energy ion beam sources a multi-stage acceleration is necessary to avoid a voltage breakdown, so other intermediate electrodes are placed between the EG and the GG.

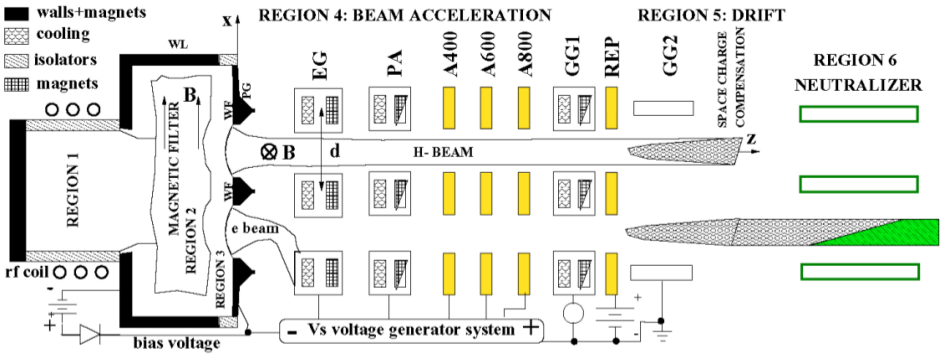

Figure 1.6: Scheme of an RF negative ion source and its accelerating column.

The two main problems when dealing with negative ion beams are the presence of a co-extracted current of electrons and the stripping reactions between the accelerated H^- and the background hydrogen gas. The first problem is solved by embedding small permanent magnets in the extraction grid, which deflect the co-extracted electrons on the EG itself; permanent magnets are optionally inserted also in the post-acceleration grid PA. Since the gas pumped through the accelerator comes directly from the source, the second problem is solved by operating at the lowest source pressure possible, compatibly with the requirements on the ion current density.

After the grounded grid, there is a region where the beam becomes space charge compensated by ionizing collisions with the background H_2 molecules, so that the repulsive forces between the negative ions are screened and the beam optics is not altered during the beam propagation. Finally conversion from fast H^- to fast H^0 through charge exchange happens in the neutralizer, whose length and gas pressure are optimized in order to achieve the highest fraction of neutralized particles.

The fusion experimental reactor ITER will operate with a D-T plasma, so the beam species that has to be used to heat the plasma and to avoid plasma dilution is D^0. Two neutral beam injectors are planned to be built and installed in ITER and space for a third one is reserved inside its shielded building. The required performance of the negative ion sources for the neutral beam injectors designed for ITER is summarized in Table 1.1, where these values are the result of a compromise between the technological limits on ion extraction and acceleration and the necessity of a 16.5 MW neutral beam power (for each injector) transferred to the ITER plasma in order to achieve effective plasma heating [12].

A test facility for the ITER neutral beams named PRIMA (the Padua Research on

Table 1.1: Required performance of the ITER negative ion source.

Beam energy	1 MeV
Negative ion current	40 A
Current density	200 A m^{-2}
Ion extraction area	576 mm × 1534 mm
Operating pressure	<0.3 Pa
Co-extracted electron current (I_e/I_{D^-})	$\simeq 1$

ITER Megavolt Accelerator) is being built at the Consorzio RFX in Padua, Italy, and consists mainly of two test stands, the ion source SPIDER and the neutral beam injector MITICA. SPIDER (Source for the Production of Ions of Deuterium Extracted from an RF plasma, see Figure 1.7) will operate an ITER-scale radio-frequency negative ion source running pulses of up to 3600 seconds at maximum power with hydrogen or deuterium discharges, in order to demonstrate all the critical aspects of the ion sources for ITER's heating and diagnostic neutral beam injectors. MITICA (Megavolt ITER Injector and Concept Advancement, see Figure 1.8) on the other hand will test the 1:1-scale neutral beam injector at full acceleration voltage and power, so that the problems, expected and unexpected, that might be found when operating this very high power system can be studied and solved before the implementation on ITER.

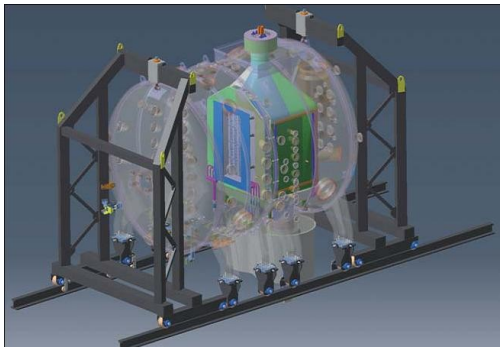

Figure 1.7: SPIDER ion source test facility [9].

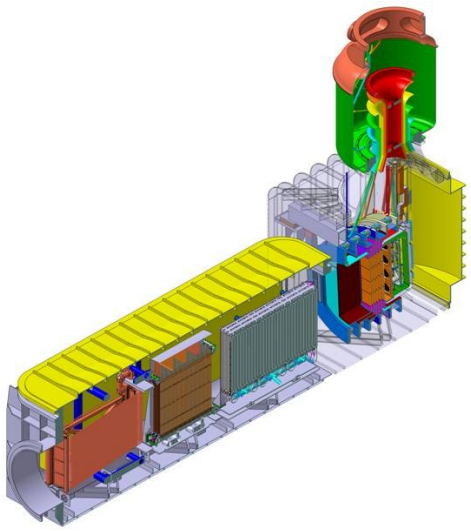

Figure 1.8: MITICA neutral beam injector test facility [9].

1.4 Thesis motivation and outline

The development of neutral beam injectors for the ITER project and the beam test facilities under construction at Consorzio RFX are a strong motivation to further investigate the ion production mechanisms and the beam extraction in negative ion sources, in order to maximize the heating efficiency. For this purpose a relatively small ion source called NOI1 (Negative Ion Optimization try 1) has been developed by Consorzio RFX and INFN-LNL (Legnaro, Italy) and will represent a test bench for source optimizations thanks to its high modularity.

A high effort has been put in these years in building sophisticated models of negative ion sources, which however are usually computationally heavy and aimed at the description of a specific region of the source or acceleration system.
Conversely the purpose of this thesis is to develop fast tools that can model the main physical phenomena taking place inside the NIO1 negative ion source and accelerating column, thus allowing a qualitative description of the whole system response to variations in the external operation parameters. During this thesis I also took part to the first experimental measurements made on NIO1, which allowed a comparison with the trends expected from the developed models.

The thesis is outlined as follows:
Chapter 2: a complete description of the NIO1 experiment is first given. Then the commissioning tests on the source itself and some of the first experimental results obtained during the first experimental campaign (source operation only at low power and air gas) are presented.
Chapter 3: an analytical model for the inductive coupling between the RF coil and the source plasma is proposed; by assuming a uniform electron temperature and density the power deposition is calculated in two electron density regimes, one at high density which uses the transformer formalism and one at low density.
Chapter 4: a relatively simple model which considers the diffusion and energy equations in a plasma with one ion species only is presented. This has been implemented in a multiphysics simulation software in order to obtain the electron density and temperature profiles in the source region in different experimental conditions.
Chapter 5: the effect of the magnetic filter field in NIO1 on the electron temperature in the extraction region is investigated by the use of a code written in C++, which calculates the electron trajectories by the implementation of the Boris algorithm and the inclusion of collisions by using a Monte Carlo approach.
Chapter 6: lastly a description of the numerical simulations done on the beam acceleration is given. The two codes used, the well tested SLACCAD and EAMCC, have been run postulating an extracted ion current compatible with the first experimental conditions in NIO1, in particular the absence of Cs gas seeding.

CHAPTER 2

NIO1 experiment

2.1 Experiment description

The negative ion beam source NIO1 (Negative Ion Optimization try 1) is designed according to the principles of inductively coupled plasma sources (ICP) with RF coil external to the plasma, which is the kind of source selected for ITER applications thanks to its greater reliability compared to filament sources. NIO1 is the result of a collaboration between Consorzio RFX and INFN (LNL) and aims to produce a total 130 mA H^- current, where the ions are accelerated up to an energy of 60 keV; it operates at an RF frequency 2 ± 0.2 MHz and a maximum power coupled to the source of 2.5 kW.

Since its main aim is to investigate the optimal configurations for ion beam production, it is more compact and modular than the negative ion sources for beam injection such as SPIDER and MITICA, thus allowing for relatively quick changes in the experimental configurations; a schematic view of NIO1 conceptual design is given in Figure 2.1, showing the source and the acceleration regions.

The plasma inside the source, which is a chamber with a 100 mm internal diameter, is inductively coupled to an external RF coil with 7 turns, which is wound around a 78 mm long ceramic tube: the coil is water cooled, while the ceramic tube is air cooled. The radiofrequency generator is matched to the coil circuit through the matching box outlined in Figure 2.3, featuring an adjustable capacitor C_A (40 turns maximum and 60 pF for turn, giving a maximum capacity of 2.4 nF) in series and three capacitors in parallel with the RF coil: C_B is adjustable (with the same characteristics as C_A) and the other two have fixed capacitance ($C_1 = C_2 \simeq 2$ nF).

The accelerating column in NIO1 consists of four grids, each one with a 3×3 matrix of apertures (radius of the PG apertures 3.8 mm) equally spaced by 14 mm:

- plasma grid PG (Figure 2.2): it is the grid which faces the plasma and is held at the source voltage (−60 kV nominal);
- extraction grid EG: it is held at a voltage higher than that of the PG (about −52 kV) to extract and accelerate the negative ions. Its voltage can be tuned in

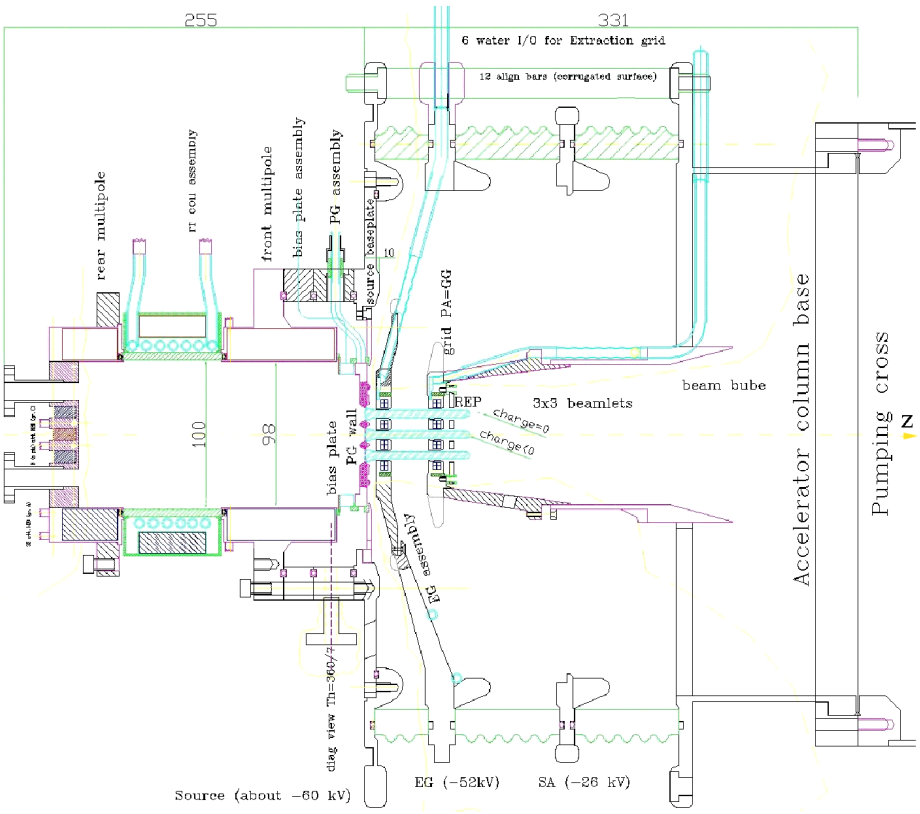

Figure 2.1: NIO1 source and accelerating column conceptual design [13].

order to optimize the beamlet optics;

- post-acceleration grid PA: it coincides with the grounded grid GG and is held at ground potential;
- repeller: also held at ground potential or at slightly positive voltage to prevent positive ions from being accelerated back into the source.

All grids as well as the source walls are adequately cooled by water; the plasma grid can be heated by air to optimise the generation of negative ions.

To deflect the co-extracted electrons, 4 permanent magnets are embedded in the EG with magnetization along the $\hat{z}$ direction (along the beam axis) alternatively positive or negative from one row to the other, centered at $y = \pm\ 7\,\text{mm}$ and $y = \pm\ 21\,\text{mm}$: the resulting B_y field between the holes is equalized by two iron shimming bars centered at $y = \pm\ 27\,\text{mm}$ which produce a reversed image of the permanent magnets. Even though the deflection experienced by the ion beam is small, it can be corrected not only by

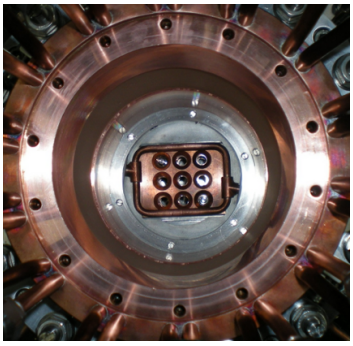

Figure 2.2: Bias plate and PG.

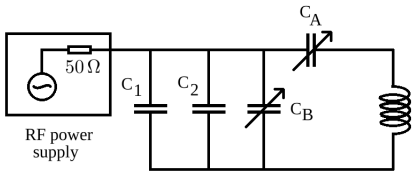

Figure 2.3: Scheme for the NIO1 matching circuit between the RF power supply and the coil.

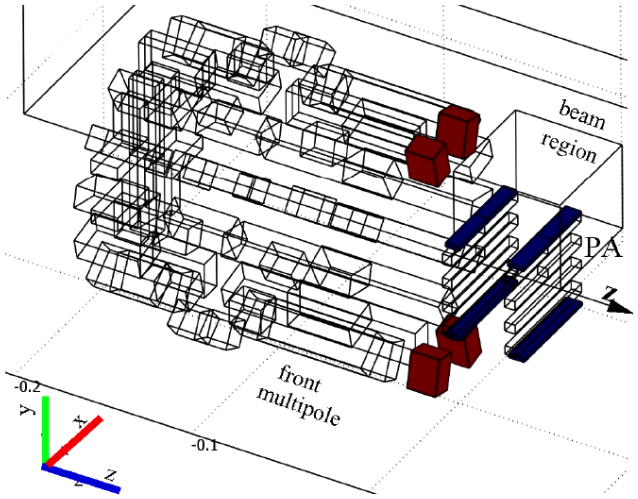

Figure 2.4: Permanent magnet system in NIO1 [14].

the focusing effect of the PA and GG potentials, but also by a reversed magnetic field in the y direction. To this purpose, four permanent magnets are inserted also in the PA electrode, with a reversed polarity with respect to those in the EG. In Figure 2.4 the permanent magnet system used in NIO1 is represented, where the blue bars are the iron shims. The brown bars in the same figure are the filter magnets, whose field smoothly merges with the multipole magnetic field used to confine the plasma inside the source: the multipole arrays are organized in the rear and front multipole assemblies and generate a 14 cusp magnetic field; optional permanent magnets can also be installed behind the coil to supplement plasma confinement.

In order to enhance the negative ion production and reach an extracted current $j_{H^-} > 280\,\mathrm{A\,m^{-2}}$ (equivalent to $200\,\mathrm{A\,m^{-2}}$ of D^-, the ITER design value), NIO1 has been designed to include an external Caesium oven, that can inject Cs gas into the source

through a port placed in the plasma grid assembly.

The source is equipped with four lines of sight (LOS) parallel to the plasma grid, which pass between the multipole bars at a 26 mm distance from the PG, and two LOS perpendicular to the plasma grid, installed on the back of the RF driver: these are used for diagnostic purposes, in particular to measure the plasma impurity content, the electron temperature and the density of electrons, H^-, Cs and neutral hydrogen inside the source.

After acceleration, the beam travels inside a 84 mm internal diameter tube called beam tube to the pumping cross and then to the diagnostic chamber (a 1.5 m long tube with a 350 mm internal diameter) where various ports allow different kinds of beam diagnostic. NIO1 does not include a neutralizer and the beam is terminated on a 180 mm diameter copper beam dump which is used also for calorimetric measurements [15].

In order to reduce the stripping losses during the acceleration, the source operation pressure will be between 0.3 Pa and 1 Pa; a turbomolecular and a rotary pump connected to the diagnostic chamber pump the gas that passed through the electrodes grid and through the large lateral windows between the arms that support the grids themselves. The gas is fed into the sorce by a feedback-controlled valve: the resulting source pressure is measured with a Pirani vacuum gauge installed in the plasma grid assembly, while the pressure reached in the vacuum chamber is measured with a combined Pirani-ionisation vacuum gauge downstream the vacuum pumps.

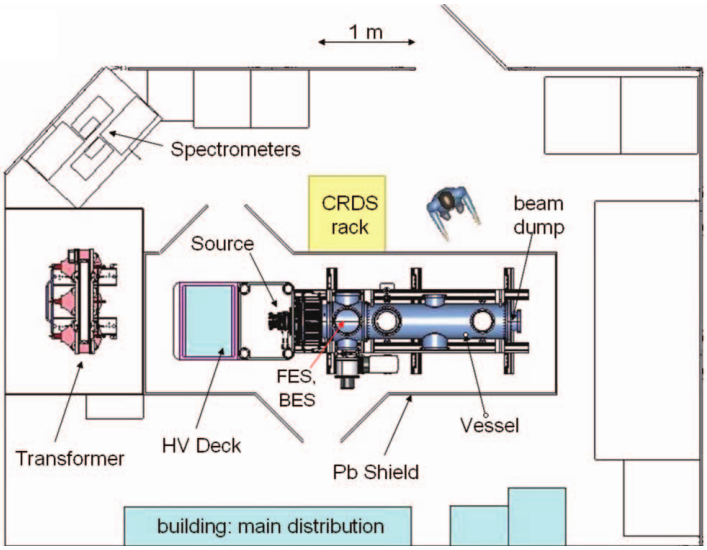

Figure 2.5: Plan of the source installation [15].

An overall plan of the ion source installation is given in Figure 2.5: an insulation transformer (70 kV, 50 kV A) powers the equipment at source voltage, in particular the high voltage deck positioned near the ion source. This contains the RF generator and its matching box, the EG grid voltage supply, the high current supply for biasing the source

electrode, the gas regulation and source pressure measurement system and supports the source cooling connections. For safety reasons (X-ray emission) the HV deck, the source and the diagnostic chamber are surrounded by lead shielding and the whole experimental area is locked during operation.

2.2 Source tests

Before operating the NIO1 source for the first time, several tests have been done in order to characterize and optimize the experimental setup.

2.2.1 Coil impedance

The impedance of the external coil (Figure 2.6) used to couple the RF power to the plasma has been measured with the Hewlett Packard 4194A Impedance/Gain-Phase Analyzer, equipped with the impedance probe mod. 41941-61002. A first scan in frequency has been done in the wide range between 10 kHz and 100 MHz, showing instabilities for frequencies higher than 10 MHz (see Figure 2.8(a)); the impedance has then been measured in a narrow range around 2 MHz (1.99 MHz$< f <$2.01 MHz), giving the results in Figure 2.8(b). An equivalent circuit like the one in Figure 2.7 can be used to model the coil, where the values of the circuit components obtained from interpolation of the experimental impedance $|Z|$ with a $|Z|_{\text{equiv. circ.}}$ are summarized in Table 2.1.

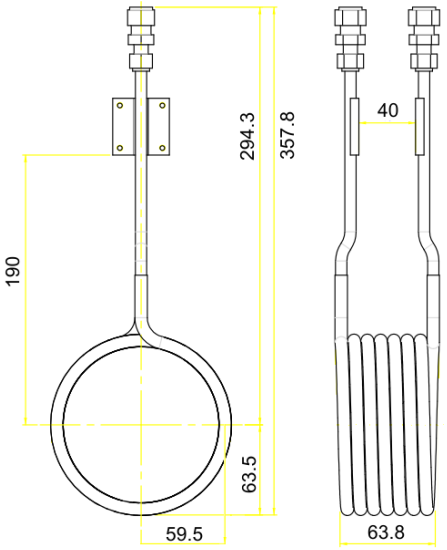

Figure 2.6: NIO1 RF coil geometry.

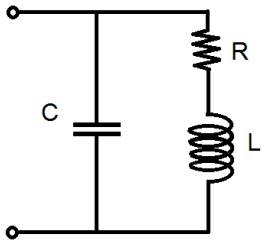

Figure 2.7: Equivalent circuit for the NIO1 RF coil.

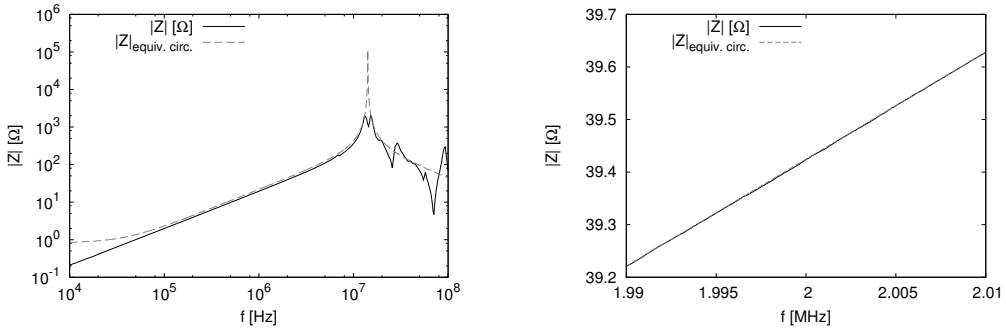

(a) Coil impedance over a wide frequency range, 10 kHz< f <100 MHz.

(b) Coil impedance in a range around the 2 MHz operation frequency.

Figure 2.8: Coil impedance $|Z|$ as measured from the Hewlett Packard 4194A Impedance/Gain-Phase Analyzer; the dashed line corresponds to the impedance of the equivalent circuit in Figure 2.7.

Table 2.1: Equivalent circuit components.

	10 kHz< f <100 MHz	1.99 MHz< f <2.01 MHz
R	826 mΩ	317 mΩ
L	3.46 µH	3.09 µH
C	36.5 pF	33.7 pF

The circuit with a series resistance $R^{\mathrm{eq}}_{\mathrm{coil}}$ and inductance $L^{\mathrm{eq}}_{\mathrm{coil}}$, equivalent to the circuit in Figure 2.7 at 1.99 MHz< f <2.01 MHz, has components:

- $R^{\mathrm{eq}}_{\mathrm{coil}} = 331\,\mathrm{m\Omega}$
- $L^{\mathrm{eq}}_{\mathrm{coil}} = 3.09\,\mu\mathrm{H}$

whose values have been used in the analytical model for the RF coupling in Chapter 3.

2.2.2 Matching box and frequency tuning

In order to have a good coupling between the RF power supply and the source plasma, the coupling circuit, and in particular the adjustable capacitors in the matching box, has to be correctly dimensioned. For this purpose the gain of the circuit including the RF coil and the matching box has been measured as in Figure 2.9, where the input signal was sent into the circuit by a function generator and the output voltage was read by a digital oscilloscope.

Since the nominal operation frequency for NIO1 is around 2.1 MHz, the capacitors $\mathrm{C_A}$ and $\mathrm{C_B}$ have been adjusted in such a way that the peak in the circuit gain is centered around this frequency, in particular they have been set to the values:

- $\mathrm{C_A} = 1.42\,\mathrm{nF}$

- $C_B = 1.30\,nF$

Using an input voltage of 1 V pk-pk and by keeping the capacitors fixed at these values, the output voltage has been measured in a frequency range around 2.1 MHz: as can be seen in Figure 2.10, the resonance peak is centered in $f_{RES} = 2056\,kHz$. The width Δf of the resonance peak at $1/\sqrt{2}$ the maximum gain (that is at G=0.99) is $\Delta f = 53.4\,kHz$, from which the circuit Q-factor, defined as the ratio of the resonant frequency to the half-power bandwidth, can be calculated:

$$Q = \frac{f_{RES}}{\Delta f} = 38.5 \tag{2.1}$$

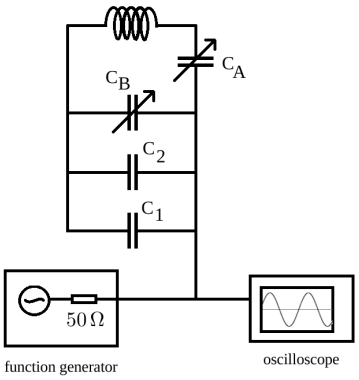

Figure 2.9: Schematic circuit for the gain measurement.

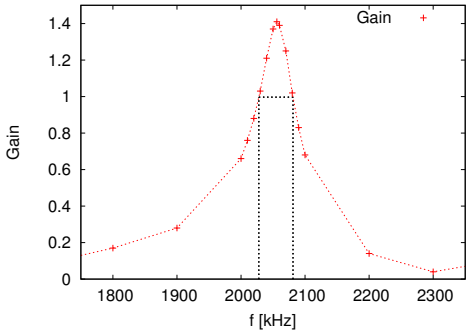

Figure 2.10: Circuite gain voltage.

2.2.3 Pressure calibration

As previously said, in NIO1 the pressure is measured in two positions:

- in the source, near the PG, by a Pirani vacuum gauge;
- in the vessel, by a combined Pirani-ionisation vacuum gauge;

Since plasma operation in the source and in particular the RF fields can interfere with the pressure measurements in the source itself with the risk of damaging the instrument, during the first operations the Pirani vacuum gauge in the source will not be used when the plasma is coupled to the RF power supply: a calibration between the pressure measured in the vessel and the pressure in the source is then necessary. For this purpose air has been used as feeding gas in the source and the valve that regulates the gas flux has been manually controlled by a voltage supply: for each value of the voltage at the valve V_{valve}, the corresponding pressures at the source p_{source} and in the vessel p_{vessel} have been measured. As can be seen in Figure 2.11, the pressure measurements made by both gauges display a different behaviour between the opening and the closing phase of the valve, maybe due to some hysteresis in the system, so during plasma operation

the source pressure cannot be inferred from V_{valve} unless the desired operation pressures are reached only by progressively opening or closing the valve. Nevertheless a univocal

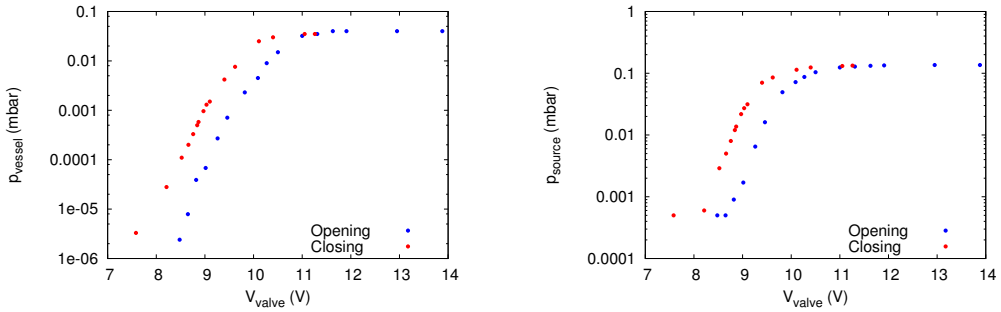

(a) Vessel pressure p_{vessel}. **(b)** Source pressure p_{source}.

Figure 2.11: Pressure measurements as a function of the valve input voltage V_{valve}: in red the values obtained in the closing phase of the valve, in blue the values corresponding to the opening phase.

relationship between the pressure in the vessel and in the source can be found as shown in Figure 2.12(b), where the data correspond to the pressure values measured during the closing and the opening phases of the gas valve. As can be seen at low pressures ($p_{vessel} < 2.3 \cdot 10^{-3}$ mbar) p_{source} increases linearly with p_{vessel} (see Figure 2.12(a)), while at higher pressures the pressure in the source has a less steep increase with p_{vessel}. These values have been interpolated with two fitting functions, in particular in the range:

- $2.8 \cdot 10^{-5}$ mbar $< p_{vessel} < 2.3 \cdot 10^{-3}$ mbar, the fitting function is $f(x) = mx + q$, where $m = 21.1$ and $q = 6.44 \cdot 10^{-4}$ mbar^{-1};
- $2.3 \cdot 10^{-3}$ mbar $< p_{vessel} < 4 \cdot 10^{-2}$ mbar, the fitting function is $g(x) = C \ln(Dx + E)$, where $C = 2.72 \cdot 10^{-2}$ mbar, $D = 3.31 \cdot 10^{3}$ mbar^{-1} and $E = -1.69$.

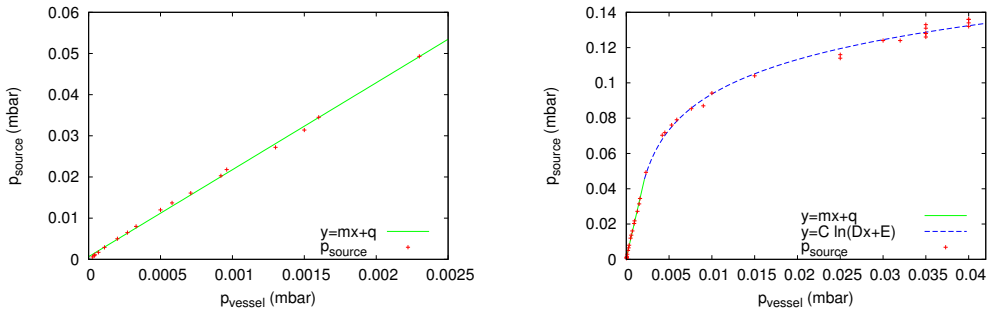

(a) Zoom in the linear region. **(b)** Whole pressure range.

Figure 2.12: Pressure calibration.

These fitting functions have been used during the first experimental session in NIO1 to calculate the source pressure from the pressure measured in the vessel when the power supply was operating; these values have also been used to determine the pressure profile in the accelerating column in NIO1, used in Chapter 6 for beam simulations.

2.3 First NIO1 experimental session

During this thesis the negative ion source NIO1 was turned on for the first time (without acceleration), using air as feeding gas; plasma ignition has been observed with a coupled power up to 300 W.

Two main quantities involving the plasma parameters have been measured:

- the plasma light, which has been measured with a photomultiplier (PMT) positioned in the back of the source through an axial line of sight;
- the plasma spectrum, which has been registered by two spectrometers (one with low resolution and the other with high resolution) whose line of sight was parallel to the PG and 26 mm away from it.

A complete description of the experimental setup together with the results obtained can be found in [16].

An estimate of the electron temperature can be obtained from an analysis of the plasma spectrum, in particular from the line ratio between N_2^+ transition at 391.4 nm and the N_2 transition at 394.3 nm in the hypothesis of a maxwellian electron distribution: however the intensity ratio between these two lines measured at a 6 Pa pressure for a RF power up to 300 W shows a decrease of the electron temperature with increasing applied RF. This probabily suggest that the value obtained for the electron temperature cannot be considered correct and the model used is inadequate to the specific situation, so more refined models have to be used in order to correctly evaluate the electron temperature. [16].

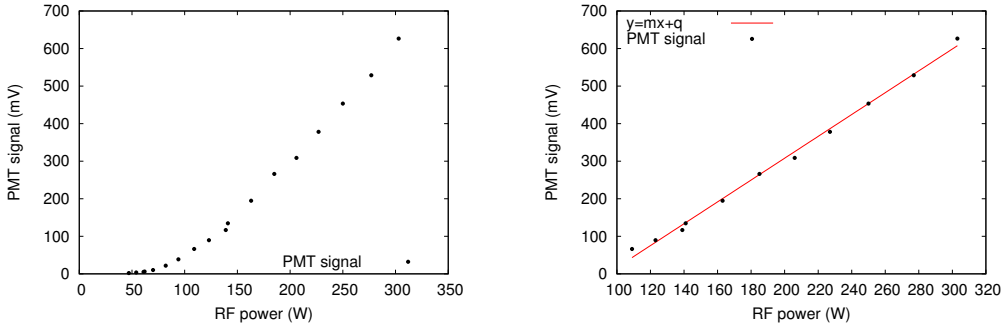

(a) PMT signal in the RF power range examined.

(b) Zoom in the linear range, that is for RF power above 100 W.

Figure 2.13: PMT signal as a function of the RF power at 1.1 Pa.

A preliminary plot of the plasma luminosity as a function of the RF power is shown in Figure 2.13(a): below 100 W the plasma light increases exponentially with power, while above 100 W the plasma luminosity depends linearly on the RF power (see Figure 2.13(b)). Since the plasma light depends linearly on the electron density, a linear dependence can be assumed between these two quantities if the electron temperature remains constant or the plasma light dependence on the electron temperature is not very strong: this is what is done in Section 4.6.3 when comparing the experimental trends for the PMT signal with the results obtained from the numerical simulation.

CHAPTER 3

Analytic model for an inductively coupled plasma

In this chapter an analytical model will be used to describe the power deposition in the NIO1 plasma source at different electron temperatures and densities. In inductively coupled plasma (ICP) sources power is transferred from the electric fields to the plasma electrons via two mechanisms: a collisional ohmic dissipation and a collisionless or stochastic heating [17]. In the first process the collisions break the phase coherent motion of the electrons with respect to the electric field [18], which otherwise would do no work on average, whereas in the second process it is the spatial nonuniformity of the electric field itself which leads to electron heating [10]; in Section 3.1 a description and modelization of these two mechanisms is presented.

In order to build an analytical model to describe the power deposition in the plasma, the electron temperature and density will be considered as constant over the volume: in Section 3.2 a model valid for high electron densities is presented, which uses the transformer formalism, whereas in Section 3.3 a model valid in the case of low electron densities is discussed.

3.1 Plasma heating

3.1.1 Electron collisions

Electrons inside a plasma can undergo several kinds of collisions with neutral particles and ions, which lead to momentum and energy transfer between the particles. The collision frequency for a process j can be written as $\nu_{\mathrm{j}} = n_{\mathrm{target}} k_{\mathrm{j}}$, where k_{j} is the reaction rate for the j-th process and n_{target} is the number density of the target particles. The reaction rate is calculated as the product $\sigma|\vec{v}|$ averaged over a maxwellian distribution function:

$$k(T) = \langle \sigma v \rangle (T) = \sqrt{\frac{8e}{\pi m_{\mathrm{e}}}} \frac{1}{T^{3/2}} \int_0^\infty \sigma(E) E e^{-E/T} \, dE \tag{3.1}$$

with E and T expressed in eV. For electron collisions with neutrals, n_{target} corresponds to the gas density and can be calculated as:

$$n_{\mathrm{target}} = n_{\mathrm{gas}} = \frac{p_{\mathrm{gas}}}{k_B\, T_{\mathrm{gas}}} \tag{3.2}$$

By taking into consideration electron collisions with ions, n_{target} corresponds to the ion density which is equal, in the hypothesis of quasi-neutrality and by considering only one ion species, to the electron density:

$$n_{\mathrm{ion}} = n_{\mathrm{e}} \tag{3.3}$$

The collision frequencies for electron-neutral scattering are the following:

- momentum-transfer electron-neutral collision frequency: $\nu_{\mathrm{en}}^{(\mathrm{p})}(T_{\mathrm{e}}) = n_{\mathrm{gas}}\, k_{\mathrm{en}}^{(\mathrm{p})}(T_{\mathrm{e}})$. $k_{\mathrm{en}}^{(\mathrm{p})}$ is calculated from $\sigma_{\mathrm{en}}^{(\mathrm{p})}$ in [19] and using (3.1).
- electron-neutral ionization collision frequency: $\nu_{\mathrm{en}}^{(\mathrm{iz})}(T_{\mathrm{e}}) = n_{\mathrm{gas}}\, k_{\mathrm{en}}^{(\mathrm{iz})}(T_{\mathrm{e}})$. $k_{\mathrm{en}}^{(\mathrm{iz})}$ is taken from [20].

The electron-ion collision frequency for momentum loss is calculated by averaging the Coulomb cross-section over a maxwellian distribution function, neglecting the ion motion [21]:

$$\langle \nu_{\mathrm{ei}}^{(\mathrm{p})} \rangle = n_{\mathrm{e}} \frac{4\sqrt{2\pi}}{3} \left(\frac{Ze^2}{4\pi\varepsilon_0} \right)^2 \frac{\ln \Lambda_{\mathrm{e}}}{\sqrt{m_{\mathrm{e}} (k_B T_{\mathrm{e}})^3}} \tag{3.4}$$

where $\ln \Lambda_{\mathrm{e}}$ is the Coulomb logarithm evaluated at $v_{\mathrm{e}} = \sqrt{k_B T_{\mathrm{e}}/m_{\mathrm{e}}}$:

$$\ln \Lambda_{\mathrm{e}} = \ln \Lambda \big|_{v_{\mathrm{e}}=\sqrt{\frac{k_B T_{\mathrm{e}}}{m_{\mathrm{e}}}}} = \ln \left[\frac{4\pi\, m_{\mathrm{ion}}}{e^3\, (m_{\mathrm{e}} + m_{\mathrm{ion}})} \frac{(\varepsilon_0\, k_B\, T_{\mathrm{e}})^{3/2}}{n_{\mathrm{e}}^{1/2}} \right] \tag{3.5}$$

The total collision frequency for momentum loss ν_{m} between electrons and the other particles inside the plasma is then the sum of these three contributions:

$$\nu_{\mathrm{m}} = \nu_{\mathrm{en}}^{(\mathrm{p})} + \nu_{\mathrm{en}}^{(\mathrm{iz})} + \langle \nu_{\mathrm{ei}}^{(\mathrm{p})} \rangle \tag{3.6}$$

A comparison between these collision frequencies is given in Figure 3.1, where a gas temperature T_{gas}=400 K and pressure p=1 Pa (n_{gas}=$1.8 \cdot 10^{20}\,\mathrm{m}^{-3}$), with a 10^{-4} ionization degree (n_{ion}=$1.8 \cdot 10^{16}\,\mathrm{m}^{-3}$) have been considered; it is to be noted that in the example shown, the Coulomb e-i collisions are neglible as compared to e-neutral collisions for $T_{\mathrm{e}} > 1\,\mathrm{eV}$.

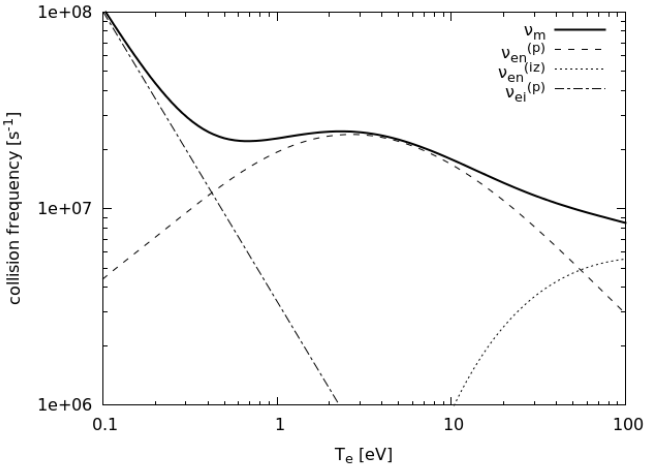

Figure 3.1: Electron collision frequencies, T_{gas}=400 K, p_{gas}=1 Pa and 10^{-4} ionization degree.

3.1.2 Plasma conductivity: a local model

A first step to study the electron heating produced by an RF field is to write the equation of motion for the electrons:

$$m_{\mathrm{e}}\frac{\partial \vec{u_{\mathrm{e}}}}{\partial t} = -e\vec{E} - m_{\mathrm{e}}\nu_{\mathrm{c}}\vec{u_{\mathrm{e}}} \tag{3.7}$$

where ν_{c} is the collision frequency for momentum loss. By assuming harmonic oscillating quantities, written as $\vec{A} = \tilde{A}e^{i\omega t}$, this becomes:

$$i\omega m_{\mathrm{e}}\tilde{u}_{\mathrm{e}} = -e\tilde{E} - m_{\mathrm{e}}\nu_{\mathrm{c}}\tilde{u}_{\mathrm{e}} \tag{3.8}$$

By solving for u_{e} and remembering the expression for the current density, an expression for the complex plasma conductivity σ_{P} is found:

$$\tilde{j}_{\mathrm{cond}} = -en_{\mathrm{e}}\tilde{u}_{\mathrm{e}} = \frac{e^2 n_{\mathrm{e}}}{m_{\mathrm{e}}}\frac{\tilde{E}}{\nu_{\mathrm{c}} + i\omega} = \sigma_{\mathrm{P}}\tilde{E} \tag{3.9}$$

where the plasma conductivity is:

$$\sigma_{\mathrm{P}} = \frac{e^2 n_{\mathrm{e}}}{m_{\mathrm{e}}}\frac{\nu_{\mathrm{c}} - i\omega}{\nu_{\mathrm{c}}^2 + \omega^2} = \varepsilon_0\,\omega_{\mathrm{pe}}^2\,\frac{\nu_{\mathrm{c}} - i\omega}{\nu_{\mathrm{c}}^2 + \omega^2} \tag{3.10}$$

and ω_{pe} is the electron plasma frequency, defined as:

$$\omega_{\mathrm{pe}} = \sqrt{\frac{e^2 n_{\mathrm{e}}}{\varepsilon_0 m_{\mathrm{e}}}} \tag{3.11}$$

In the limit $\omega \ll \nu_{\mathrm{c}}$, σ_{P} reduces to the plasma dc conductivity σ_{el}:

$$\sigma_{\mathrm{el}} = \frac{e^2 n_{\mathrm{e}}}{m_{\mathrm{e}} \nu_{\mathrm{c}}} \tag{3.12}$$

However in the following calculations the more general expression (3.10) will be retained, since the collision frequency is not always greater than the externally applied angular frequency ω (in the NIO1 case, $f = 2.1\,\mathrm{MHz}$, so $\omega{=}1.3 \cdot 10^7\,\mathrm{rad\,s^{-1}}$).

The work done per unit time and unit volume on electrons is $\vec{j} \cdot \vec{E}$ and by taking its temporal average the power density transfer is obtained:

$$p_1 = \langle \vec{j} \cdot \vec{E} \rangle_t = \frac{1}{2} \mathrm{Re}\left(\tilde{j}^* \tilde{E}\right) = \frac{1}{2} |\tilde{E}|^2 \, \varepsilon_0 \, \omega_{\mathrm{pe}}^2 \, \frac{\nu_{\mathrm{c}}}{\nu_{\mathrm{c}}^2 + \omega^2} \tag{3.13}$$

This shows that the importance of collisions in plasma heating, since $p_1 = 0$ when $\nu_{\mathrm{c}} = 0$; moreover, for small ν_{c}/ω values, the power density transfer is proportional to ν_{c}, that is $p_1 \propto \nu_{\mathrm{c}}$.

3.1.3 Skin depth

Let the RF electric field have the form of a planar wave entering along the z direction into a plasma slab having uniform temperature and density:

$$\vec{E} = \vec{E}_0 \, e^{i(\omega t - \kappa z)} = \vec{E}_0 \, e^{-\frac{z}{\delta}} e^{i(\omega t - \alpha z)} \tag{3.14}$$

where α is the real part of the vector propagation and $-1/\delta$ is its imaginary part ($\kappa = \alpha - \frac{i}{\delta}$).

Then, in order to calculate the power transferred to the plasma electrons, one needs an appropriate expression for the skin depth δ, which can be obtained by taking the curl of the Faraday law, while keeping the quasi-neutrality hypothesis ($\nabla \cdot \vec{E} = 0$):

$$\nabla \times \left(-\frac{\partial \vec{B}}{\partial t} \right) = -\frac{\partial}{\partial t} \left(\nabla \times \vec{B} \right) = \nabla \times \left(\nabla \times \vec{E} \right) = \nabla \left(\nabla \cdot \vec{E} \right) - \nabla^2 \vec{E} \simeq -\nabla^2 \vec{E} \tag{3.15}$$

Upon inserting the Ampère-Maxwell law and (3.9) in this equation, one obtains:

$$\nabla^2 \vec{E} = \frac{\partial}{\partial t} \left(\mu_0 \vec{j} + \mu_0 \varepsilon_0 \frac{\partial \vec{E}}{\partial t} \right) = \mu_0 \left(\sigma_{\mathrm{P}} \frac{\partial}{\partial t} + \varepsilon_0 \left(\frac{\partial}{\partial t} \right)^2 \right) \vec{E} \tag{3.16}$$

From this equation, by substituting the expression for the electric field written in (3.14),

one obtains the dispersion relation for a wave entering the plasma:

$$\left(\alpha - \frac{i}{\delta}\right)^2 = \kappa^2 = \left[\mu_0\,\varepsilon_0\,\omega^2\left(1 - \frac{\omega_{\mathrm{pe}}^2}{\nu_{\mathrm{c}}^2 + \omega^2}\right)\right] - i\left[\mu_0\,\varepsilon_0\,\nu_{\mathrm{c}}\,\omega\,\frac{\omega_{\mathrm{pe}}^2}{\nu_{\mathrm{c}}^2 + \omega^2}\right] = A - iB \quad (3.17)$$

After a little algebraic manipulation a general expression for the skin depth δ is obtained:

$$\delta = \frac{2}{B}\sqrt{\frac{A + \sqrt{A^2 + B^2}}{2}} \quad (3.18)$$

In the approximation $\omega_{\mathrm{pe}} \gg \nu_{\mathrm{c}}, \omega$, the skin depth reduces to the simpler form:

$$\delta = \frac{c}{\omega_{\mathrm{pe}}}\sqrt{\frac{2\,(1 + \nu_{\mathrm{c}}^2/\omega^2)}{1 + \sqrt{1 + \nu_{\mathrm{c}}^2/\omega^2}}} \quad (3.19)$$

In particular, when considering electron collisions with ions and neutrals, $\nu_{\mathrm{c}} = \nu_{\mathrm{m}}$:

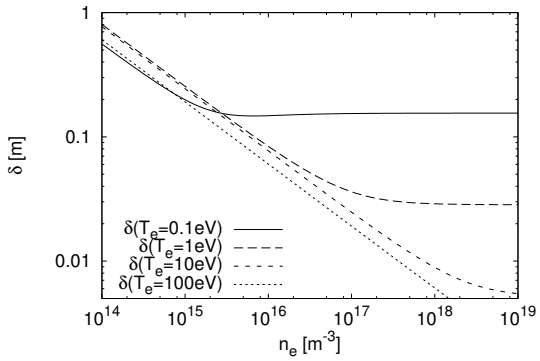

Figure 3.2: Skin depth δ.

the value of the skin depth against the electron density obtained by using the collision frequency defined in (3.6) is reported in Figure 3.2 for 4 different electron temperatures. Aa can be seen at high densities and low temperatures the effect of coulombian collisions dominates (see Figure 3.1), in particular the skin depth reaches a limiting value wich depends only on the electron temperature (see (3.4)):

$$\delta \xrightarrow[\nu_{\mathrm{m}} \simeq \nu_{\mathrm{ei}}^{(\mathrm{p})} \gg \omega]{} \sqrt{\frac{2}{\mu_0 \varepsilon_0 \omega}\,\frac{\nu_{\mathrm{ei}}^{(\mathrm{p})}}{\omega_{\mathrm{pe}}^2}} \quad (3.20)$$

The power per unit area deposited into a uniform plasma can then be calculated by

the use of (3.9), (3.10) and (3.19):

$$P_{\text{plasma}} = \frac{1}{2}\int_z \text{Re}(j^* E)\, dz = \frac{1}{2}\int_z \text{Re}(\sigma_{\text{P}})|E^2|\, dz = \frac{e^2\, E_0^2\, n_{\text{e}}\, \delta}{4\, m_{\text{e}}} \frac{\nu_{\text{m}}}{\nu_{\text{m}}^2 + \omega^2} \tag{3.21}$$

3.1.4 Stochastic heating

The fundamental mechanism that converts electric field energy into thermal energy by ohmic heating is the breaking of the phase-coherent motion of individual electrons by collisions: in the same way a spatially nonuniform electric field by itself might lead to electron heating, provided that the electrons have thermal velocities sufficient to sample the field inhomogeneity. This phenomenon is called collisionless, stochastic, nonlocal or anomalous heating [10]. In this case, the time-varying field seen by an individual thermal electron is nonperiodic due to the spatial variation in the skin depth layer, so the electron can lose phase coherence with the field (which is strictly periodic), resulting in stochastic interaction with the field and collisionless heating.

It will be shown that this heating mechanism can be associated with a stochastic collision frequency ν_{stoc}, whose well known expression will be summarized in this section, based on an equivalence between the heating power transferred to electrons in an idealized global model of stochastic heating and the heating power obtained in the local model of ohmic heating.

The non collisional heating is effective if the electron transit time through the power absorption region is shorter than the rf period [22]:

$$\tau = \frac{\delta}{v_{\text{th,e}}} < \frac{2\pi}{\omega} \tag{3.22}$$

By defining a parameter α as

$$\alpha = \frac{4\,\delta^2\,\omega^2}{\pi\, v_{\text{th,e}}^2} \propto \left(\frac{\text{transit time through } \delta}{\text{rf period}}\right)^2 \tag{3.23}$$

one can equivalently say that nonlocal heating becomes important for low α values.

When considering a planar wave entering the plasma of the form (3.14) and maxwellian electrons so that the electron thermal velocity is

$$v_{\text{th,e}} = \sqrt{\frac{8 k_B T_{\text{e}}}{\pi m_{\text{e}}}} \tag{3.24}$$

it can be shown ([10, p.707], [22, p.1449]) after integration on the whole plasma volume that the power per unit surface absorbed by the plasma is:

$$P_{\text{plasma}} = \frac{e^2\, E_0^2\, n_{\text{e}}\, \delta}{4\, m_{\text{e}}} \frac{4\,\delta}{v_{\text{th,e}}} \mathcal{I}(\alpha) \tag{3.25}$$

where $\mathcal{I}(\alpha)$ is defined as (see also Figure 3.3):

$$\mathcal{I}(\alpha) = \frac{1}{\pi}\left(e^{\alpha}\,(1+\alpha)\int_{\alpha}^{\infty}\left(\frac{e^{-x}}{x}dx\right) - 1\right) \tag{3.26}$$

In the case of dominating collisionless mechanism, one can define a stochastic collision

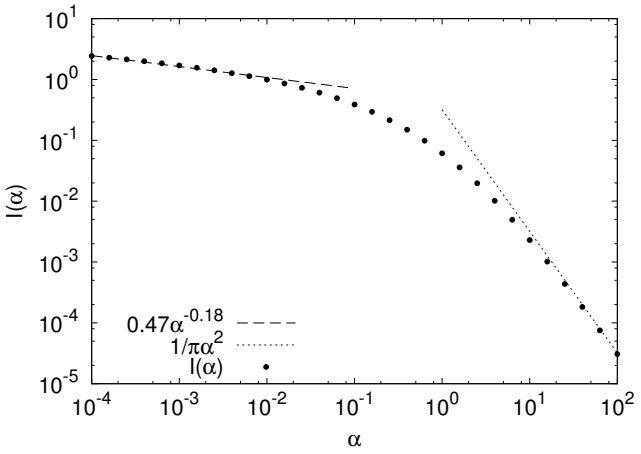

Figure 3.3: Function $\mathcal{I}(\alpha)$ with the approximations for the stochastic regime ($\alpha \ll 1$) and the collisional regime ($\alpha \gg 1$).

frequency through the expression for the power deposition in the case of ohmic heating by substituting the collision frequency ν_{m} with the stochastic one in equation (3.21):

$$P_{\mathrm{plasma}} = \frac{e^2\,E_0^2\,n_{\mathrm{e}}\,\delta}{4\,m_{\mathrm{e}}}\frac{\nu_{\mathrm{stoc}}}{\nu_{\mathrm{stoc}}^2+\omega^2} \tag{3.27}$$

The skin depth δ then has the same expression as in (3.19), where ν_{stoc} has to be used instead of ν_{m}:

$$\delta = \frac{c}{\omega_{\mathrm{pe}}}\sqrt{\frac{2\left(1+\nu_{\mathrm{stoc}}^2/\omega^2\right)}{1+\sqrt{1+\nu_{\mathrm{stoc}}^2/\omega^2}}} \tag{3.28}$$

By equating (3.25) and (3.27) then one has:

$$\frac{4\,\delta}{v_{\mathrm{th,e}}}\mathcal{I}(\alpha) = \frac{\nu_{\mathrm{stoc}}}{\nu_{\mathrm{stoc}}^2+\omega^2} \tag{3.29}$$

Equations (3.23), (3.28) and (3.29) can then be solved simultaneously for α, δ and ν_{stoc}. The δ dependence can be eliminated by putting together the first two equations, thus reducing the system to two equations which depend on the product $n_{\mathrm{e}}T_{\mathrm{e}} = x$ (here

expressed in eV m^{-3}):

$$\sqrt{4\,\pi\,\alpha}\,\mathcal{I}(\alpha) = \frac{\omega\,\nu_{\mathrm{stoc}}}{\nu_{\mathrm{stoc}}^2 + \omega^2} \tag{3.30a}$$

$$\frac{2\left(1+\nu_{\mathrm{stoc}}^2/\omega^2\right)}{1+\sqrt{1+\nu_{\mathrm{stoc}}^2/\omega^2}} = 2\,\frac{\mu_0 e^3}{m_{\mathrm{e}}^2}\,\frac{x}{\omega^2}\,\alpha \tag{3.30b}$$

which is more simply written by using the normalized collision frequency $\nu_{\mathrm{a}} = \nu_{\mathrm{stoc}}/\omega$:

$$2\sqrt{\pi}\,\sqrt{\alpha}\,\mathcal{I}(\alpha) = \frac{\nu_{\mathrm{a}}}{1+\nu_{\mathrm{a}}^2} \tag{3.31a}$$

$$\frac{1+\nu_{\mathrm{a}}^2}{1+\sqrt{1+\nu_{\mathrm{a}}^2}} = \frac{1}{K_0}\,\frac{x}{\omega^2}\,\alpha = X\,\alpha \tag{3.31b}$$

where $K_0 = m_{\mathrm{e}}^2/(\mu_0 e^3)$ and $X = x/(K_0\,\omega^2)$. The existence of a universal solution to the system (3.31) can be discussed by considering the intersection of the curves corresponding to the first and the second equation in the $(\alpha, \nu_{\mathrm{a}})$ plane: equation (3.31a) gives two solutions ν_{a}^+ and ν_{a}^- for any α (respectively the upper and lower curves plotted in blue in Figure 3.4), while at different fixed X values equation (3.31b) gives the parametric curves plotted in red in Figure 3.4, in particular the curves from right to left correspond to $X_i = 10^{i/5}$, where $i = 0,1,2,...10$. The intersection of these curves shows that two solutions for $(\alpha, \nu_{\mathrm{a}})$ may exist for a given X, so it is convenient to choose the proper root on physical grounds.

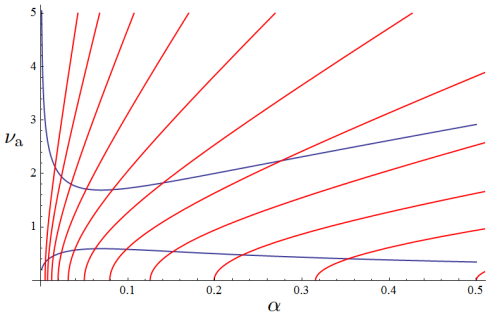

Figure 3.4: Plot of the equations in (3.31) in the $(\alpha, \nu_{\mathrm{a}})$ plane.

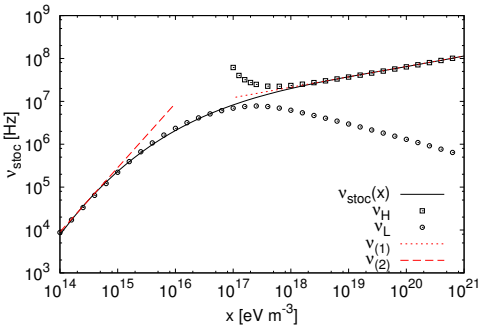

Figure 3.5: Numerical roots and analytical approximations for ν_{stoc}; $\nu_{\mathrm{stoc}}(x)$ is the value used througout the thesis.

For this purpose the system in (3.30) has been numerically solved at a fixed ω value, which corresponds to the NIO1 operation frequency $f = 2.1\,\mathrm{MHz}$ (ω=$1.3 \cdot 10^7\,\mathrm{rad\,s^{-1}}$), and $x = n_{\mathrm{e}} T_{\mathrm{e}}$ ranging from 10^{14} to 10^{21}: as expected above a certain x value it admits two solutions for ν_{stoc} (see Figure 3.5), one that stays below ω (ν_L) and one above ω (ν_H). In order to choose the proper root on physical grounds I considered the analytical

solutions in two limit cases (dashed lines in Figure 3.3 and 3.5):

- stochastic regime ($\alpha \ll 1$): in this range $\nu_{\text{stoc}} \gg \omega$ and $\mathcal{I}(\alpha)$ can be approximated by the function $\mathcal{I}^{(1)}(\alpha) = A\alpha^B$, where A=0.47 and B=-0.18. In this way (3.30) yields

$$\nu_{(1)} = \left(\frac{\omega}{\sqrt{4\pi}A} \left(\frac{\mu_0 e^3 x}{\omega m_{\text{e}}^2} \right)^{B+1/2} \right)^{\frac{1}{B+3/2}} \tag{3.32}$$

- collisional regime ($\alpha \gg 1$): in this range $\nu_{\text{stoc}} \ll \omega$ and $\mathcal{I}(\alpha)$ can be approximated by the function $\mathcal{I}^{(2)}(\alpha) = 1/\pi\alpha^2$. In this way (3.30) yields

$$\nu_{(2)} = \frac{\pi}{4\omega^2} \left(\frac{8\mu_0 e^3 \omega}{\pi m^2} \right)^{3/2} x^{3/2} \tag{3.33}$$

Figure 3.5 shows that low x values correspond to the collisional regime, so the smaller root ν_L has to be used, whereas high x values correspond to the stochastic regime, so the larger root ν_H has to be chosen.

To join the two solutions one can make a fit of the two branches with a logarithmic polinomial function $\nu_{\text{stoc}}(x)$:

$$\nu_{\text{stoc}}(x) = 10^{-244.1+48.10\log_{10}(x)-3.467\log_{10}^2(x)+0.1113\log_{10}^3(x)-0.001336\log_{10}^4(x)} \tag{3.34}$$

as reported in Figure 3.5 (continuous line). From hereinafter this fitting function (obtained in the case of ω=$1.3 \cdot 10^7\,\text{rad}\,\text{s}^{-1}$) will be used to calculate the stochastic collision frequency; note it does depend on electron density and temperature, but not on the gas used.

3.1.5 Effective collision frequency

In the next sections both the ohmic heating due to local electron collisions and the nonlocal heating just described will be taken into account by the use of an effective collision frequency ν_{eff} [10]:

$$\nu_{\text{eff}} = \nu_{\text{m}} + \nu_{\text{stoc}} \tag{3.35}$$

where ν_{m} is the collision frequency for momentum loss between electrons and the other particles defined in (3.6) and ν_{stoc} is the stochastic collision frequency in (3.34), defined upon an integration on the whole plasma volume; in order to keep a compact notation in the following calculations, ν_{c} will be used in place of ν_{eff}, keeping in mind that hereinafter $\nu_{\text{c}} \equiv \nu_{\text{eff}}$.

The skin depth δ calculated using (3.18) is shown in Figure 3.7. Considering the NIO1 case, for $n_{\text{e}} < 5 \cdot 10^{16}\,\text{m}^{-3}$ or $T_{\text{e}} < 0.5\,\text{eV}$, δ becomes greater than the chamber radius

($\delta > a = 0.05\,\mathrm{m}$), so a distinction can be made between two limit cases of coupling regimes:

- high-density regime: $\delta < a$
- low-density regime: $\delta > a$

The following sections will be dedicated to the description of the different approaches used to analyze these two regimes.

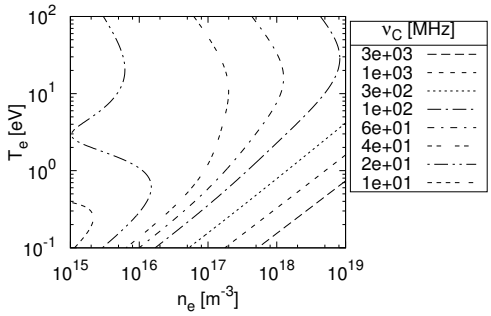

Figure 3.6: ν_c as a function of the electron temperature and density.

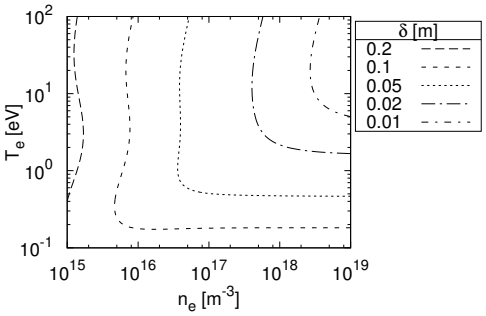

Figure 3.7: Skin depth as a function of the electron temperature and density.

3.2 High density regime

In the high density regime the skin depth is smaller than the chamber radius ($\delta \ll a$), in such a way that the following approximations are valid:

- the current flows in a skin thickness δ in the outer region of the plasma below the cylindrical coil, with a uniform current density;
- in this skin thickness the electron density n_e and the electron temperature T_e are considered as uniform.

These conditions allow introducing a well known simplified description [23], known as transfrormer model (see later chapter), where plasma total rf current and voltage are obtained from a circuit analysis. For its practical convenience, especially for simple rf ampfier matching, I will extrapolate these approximations also to regions where δ is comparable or exceeds the driver radius, setting $\delta = a$ as the maximum value for the skin depth. The source and coil geometry and its impedance measurement were described in Section 2.2, the quantities relevant to this discussion are reported in Table 3.1. The inductive coupling mechanism can be described by calling j the uniform current density flowing in the skin thickness δ: in this way the plasma current I_P and the voltage V_P

Table 3.1: Quantities related to the source and coil used in the inductive coupling model.

a	50 mm	chamber radius
b	59.5 mm	coil radius
l	63.8 mm	coil length
N	7	coil turns
$R_{\text{coil}}^{\text{eq}}$	0.331 Ω	equivalent coil resistance
		(measured by Hewlett Packard 4194A Impedance/Gain-Phase Analyzer)
$L_{\text{coil}}^{\text{eq}}$	3.09 µH	equivalent coil inductance
		(measured by Hewlett Packard 4194A Impedance/Gain-Phase Analyzer)

across this plasma loop are

$$I_{\text{P}} = j\,\delta\,l = \sigma_{\text{P}}\,E_\theta\,\delta\,l \tag{3.36a}$$

$$V_{\text{P}} = 2\pi a\,E_\theta \tag{3.36b}$$

where E_θ is the electric field produced by the coil and σ_{P} is the plasma conductivity. Combining these two with (3.10) and using (3.12), the plasma resistance R_{P} and inductance L_{P} take the form:

$$V_{\text{P}} = \frac{2\pi a}{\delta\,l}\frac{\nu_{\text{c}} + i\omega}{\varepsilon_0\,\omega_{\text{pe}}^2} I_{\text{P}} = (R_{\text{P}} + i\omega L_{\text{P}})\,I_{\text{P}} \tag{3.37}$$

Now, by noting that $\sigma_{\text{el}} = \varepsilon_0\,\omega_{\text{pe}}^2/\nu_{\text{c}}$, one can write:

$$R_{\text{P}} = \frac{2\pi a}{\delta\,l\,\sigma_{\text{el}}} \tag{3.38a}$$

$$L_{\text{P}} = \frac{R_{\text{P}}}{\nu_{\text{c}}} \tag{3.38b}$$

3.2.1 Transformer model and coupling circuit

As done in [23], the inductively coupled discharge is regarded as the secondary coil of a transformer, whereas the primary of the transformer is the induction coil itself (with inductance and resistance listed in Table 3.1); as the discharge is a conductive fluid sheath surrounded by the coil, it is considered as a one turn secondary winding. An estimate of the coil and discharge inductances can be given by

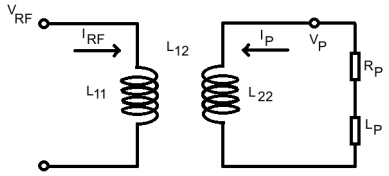

Fig. 3.8: Transformer model.

correcting the inductance for an ideal solenoid (in which $r \gg l$) with the Nagaoka factor $\mathcal{K}$, which depends on the the ratio between the diameter and the length of the solenoid [24]; in particular in NIO1:

- $\mathcal{K}_\mathrm{b}(2b/l) = \mathcal{K}_\mathrm{b}(1.87) = 0.54$ (coil)
- $\mathcal{K}_\mathrm{a}(2a/l) = \mathcal{K}_\mathrm{a}(1.57) = 0.58$ (discharge)

Then the self-inductance of the coil (L_{11}) and of the current sheet in the plasma (L_{22}) are:

$$L_{11} = \mu_0 \pi b^2 \frac{N^2}{l} \mathcal{K}_\mathrm{b} = 5.8\,\mu\mathrm{H} \tag{3.39a}$$

$$L_{22} = \mu_0 \pi \frac{a^2}{l} \mathcal{K}_\mathrm{a} = 9.0 \cdot 10^{-2}\,\mu\mathrm{H} \tag{3.39b}$$

The mutual inductance L_{12} is calculated considering the magnetic flux through the coil due to the plasma current, yielding:

$$L_{12} = \mu_0 \pi \frac{a^2 N}{l} \mathcal{K}_\mathrm{a} = 0.63\,\mu\mathrm{H} \tag{3.40}$$

note that the coupling coefficient $k = L_{12}/\sqrt{L_{11}\,L_{22}}$, which depends on the space between a and b, is 0.87 in this case. Using these quantities and considering sinusoidal signals of the form $\vec{A} = \mathrm{Re}\tilde{A}e^{i\omega t}$, the inductance matrix for this transformer becomes:

$$\begin{cases} \tilde{V}_\mathrm{RF} = (R_\mathrm{coil} + i\omega L_{11})\tilde{I}_\mathrm{RF} + i\omega L_{12}\tilde{I}_\mathrm{P} \\ \tilde{V}_P = i\omega L_{21}\tilde{I}_\mathrm{RF} + i\omega L_{22}\tilde{I}_\mathrm{P} \end{cases} \tag{3.41}$$

By inserting (3.36a) with the opposite sign (see Figure 3.8) in the second one, one obtains the plasma current as a function of the coil current I_RF:

$$\tilde{I}_\mathrm{P} = -\frac{i\omega L_{12}}{i\omega(L_{22} + L_\mathrm{P}) + R_\mathrm{P}} \tilde{I}_\mathrm{RF} \tag{3.42}$$

Then, by inserting this in the first one in (3.41), an expression for the load impedance Z_L seen by the generator is readily obtained:

$$\begin{aligned} Z_\mathrm{L} &= R_\mathrm{L} + i\omega L_\mathrm{L} = \\ &= \frac{\tilde{V}_\mathrm{RF}}{\tilde{I}_\mathrm{RF}} = \\ &= \left[R_\mathrm{coil} + \frac{\omega^2 R_\mathrm{P} L_{12}^2}{R_\mathrm{P}^2 + \omega^2 (L_{22} + L_\mathrm{P})^2} \right] + i\omega \left[L_{11} - \frac{\omega^2 (L_{22} + L_\mathrm{P}) L_{12}^2}{R_\mathrm{P}^2 + \omega^2 (L_{22} + L_\mathrm{P})^2} \right] \end{aligned} \tag{3.43}$$

This shows that the load impedance depends on the coil impedance and on the plasma parameters through L_{22} and L_{12}, in particular the load inductance decreases in the

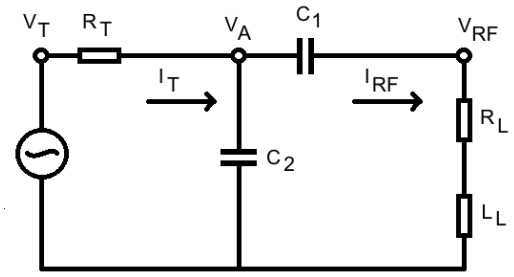

Figure 3.9: Equivalent circuit for an inductive discharge including the matching capacitors.

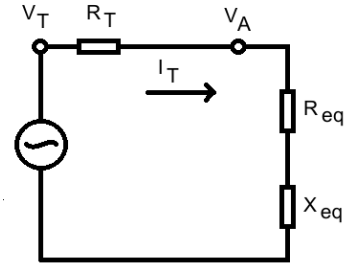

Figure 3.10: Equivalent circuit for the total load impedance seen by the power supply.

presence of the plasma.

In order to have control over the impedance seen by the RF generator and in particular to have the maximum power transfer to the plasma, the generator's output impedance has to be matched through a capacitive matching network as shown in Figure 3.9. If $R_\mathrm{T} = 50\,\Omega$ is the source resistance, then the circuit is matched when

$$\frac{1}{Z_\mathrm{eq}} = Y_\mathrm{eq} \equiv G_\mathrm{eq} + iB_\mathrm{eq} = \frac{1}{R_\mathrm{T}} \tag{3.44}$$

where Z_eq, Y_eq, G_eq and B_eq are respectively the impedance, the admittance, the conductance and the susceptance seen at the RF generator's terminals (wich takes into account the matching network, the coil and the plasma load, see Figure 3.10). The expression for the reactances of the two capacitors obtained in this way are the following ones (see Appendix A.1 for the detailed calculation):

$$\begin{aligned} X_1 &\equiv -\frac{1}{\omega C_1} = \sqrt{R_\mathrm{L}(R_\mathrm{T} - R_\mathrm{L})} - X_\mathrm{L} \\ X_2 &\equiv -\frac{1}{\omega C_2} = -R_\mathrm{T}\sqrt{\frac{R_\mathrm{L}}{R_\mathrm{T} - R_\mathrm{L}}} \end{aligned} \tag{3.45}$$

where $X_\mathrm{L} \equiv \omega L_\mathrm{L}$. The values obtained for the capacitors in series (C_1) and in parallel (C_2) with the coil are those presented in Figure 3.11 and are calculated for a gas temperature $T_\mathrm{gas} = 400\,\mathrm{K}$ and pressure $p_\mathrm{gas} = 1.0\,\mathrm{Pa}$ ($n_\mathrm{gas} = 1.8 \cdot 10^{20}\,\mathrm{m}^{-3}$): it can be seen that they strongly depend on the electron density, in particular with decreasing density C_1 has to decrease and C_2 to increase . For an electron density $n_\mathrm{e} = 1 \cdot 10^{17}\,\mathrm{m}^{-3}$ and temperature $T_\mathrm{e} = 10\,\mathrm{eV}$, C_1 and C_2 can be evaluated at two different pressures and the same gas temperature $T_\mathrm{gas} = 400\,\mathrm{K}$:

- $p_\mathrm{gas} = 1.0\,\mathrm{Pa}$: $C_1 = 2.52\,\mathrm{nF}$, $C_2 = 2.33\,\mathrm{nF}$
- $p_\mathrm{gas} = 0.3\,\mathrm{Pa}$: $C_1 = 2.28\,\mathrm{nF}$, $C_2 = 3.90\,\mathrm{nF}$

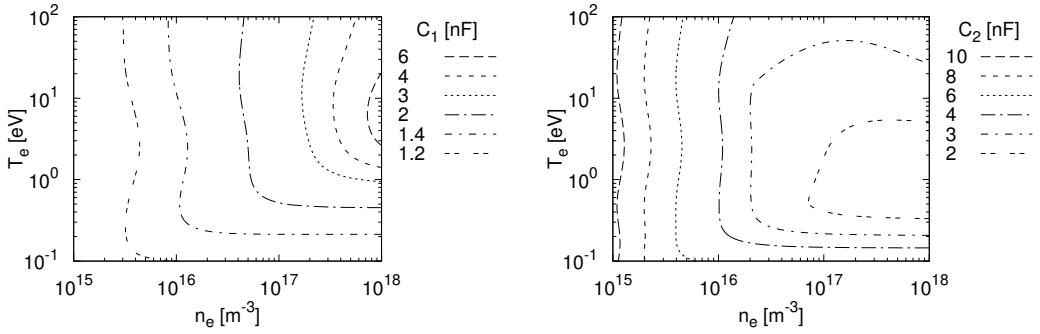

(a) C_1, series capacitor. **(b)** C_2, parallel capacitor.

Figure 3.11: Capacitors values to obtain impedance matching.

Once the capacitors have been set to a fixed C_1 and C_2, the load resistance and reactance are:

$$\begin{aligned} R_{\mathrm{eq}} &= \frac{R_{\mathrm{L}} X_2^2}{R_{\mathrm{L}}^2 + (X_1 + X_2 + X_{\mathrm{L}})^2} \\ X_{\mathrm{eq}} &= X_2 - \frac{X_2^2 (X_1 + X_2 + X_{\mathrm{L}})}{R_{\mathrm{L}}^2 + (X_1 + X_2 + X_{\mathrm{L}})^2} \end{aligned} \tag{3.46}$$

At this point, using (3.42) and the relation $V_{\mathrm{A}} = (R_{\mathrm{eq}} + iX_{\mathrm{eq}})I_{\mathrm{T}} = (R_{\mathrm{L}} + i(X_1 + X_{\mathrm{L}}))I_{\mathrm{RF}}$, the currents across the circuit in Figure 3.9 and in the plasma take the following expressions:

$$|I_{\mathrm{T}}| = \frac{|V_{\mathrm{A}}|}{\sqrt{R_{\mathrm{eq}}^2 + X_{\mathrm{eq}}^2}} \tag{3.47a}$$

$$|I_{\mathrm{RF}}| = \frac{\sqrt{\left[R_{\mathrm{L}} R_{\mathrm{eq}} + (X_1 + X_{\mathrm{L}}) X_{\mathrm{eq}}\right]^2 + \left[R_{\mathrm{L}} X_{\mathrm{eq}} - (X_1 + X_{\mathrm{L}}) R_{\mathrm{eq}}\right]^2}}{R_{\mathrm{L}}^2 + (X_1 + X_{\mathrm{L}})^2} |I_{\mathrm{T}}| \tag{3.47b}$$

$$|I_{\mathrm{P}}| = \frac{\omega L_{12}}{\sqrt{\omega^2 (L_{22} + L_{\mathrm{P}})^2 + R_{\mathrm{P}}^2}} |I_{\mathrm{RF}}| \tag{3.47c}$$

whereas using (3.41) and (3.42), the voltage across the coil reads:

$$\tilde{V}_{\mathrm{RF}} = \left(R_{\mathrm{coil}} + i\omega L_{11} + \frac{\omega^2 L_{12}^2}{i\omega (L_{22} + L_{\mathrm{P}}) + R_{\mathrm{P}}} \right) \tilde{I}_{\mathrm{RF}} \tag{3.48}$$

3.2.2 RF coupling dependence on plasma parameters

Using the equations obtained in the previous section,the power absorbed by the plasma can be calculated through (3.47) and (3.38a) as a function of the output voltage at the RF generator :

$$P_{\text{abs}} = \frac{1}{2} R_{\text{P}} I_{\text{P}}^2 \tag{3.49}$$

The total input power instead is:

$$P_{\text{in}} = \frac{1}{2} R_{\text{L}} I_{\text{RF}}^2 \tag{3.50}$$

The absorbed power for an output voltage $V_{\text{A}} = 100\,\text{V}$, gas temperature $T_{\text{gas}} = 400\,\text{K}$ and two different operating pressures, $p_{\text{gas}} = 1.0\,\text{Pa}$ and $p_{\text{gas}} = 0.3\,\text{Pa}$, is shown in Figure 3.12; the two capacitors are set to two fixed values for each pressure, corresponding to those necessary to have impedance matching assuming a uniform $n_{\text{e}} = 1 \cdot 10^{17}\,\text{m}^{-3}$ and $T_{\text{e}} = 10\,\text{eV}$ (see Section 3.2.1).

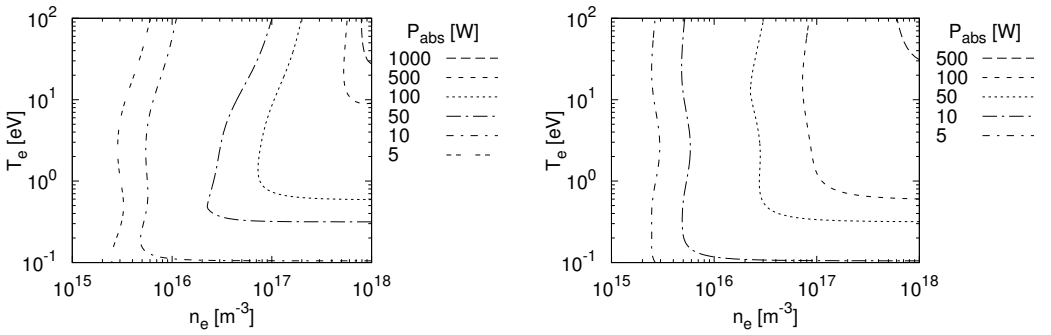

(a) $p_{\text{gas}} = 0.3\,\text{Pa}$ ($n_{\text{gas}} = 5.4 \cdot 10^{19}\,\text{m}^{-3}$). **(b)** $p_{\text{gas}} = 1.0\,\text{Pa}$ ($n_{\text{gas}} = 1.8 \cdot 10^{20}\,\text{m}^{-3}$).

Figure 3.12: Power transmitted to a hydrogen plasma at two gas pressures, $T_{\text{gas}} = 400\,\text{K}$ and $V_{\text{A}} = 100\,\text{V}$.

Instead of setting the two capacitors to fixed values one can calculate the absorbed power in the case of impedance matching: by setting $V_{\text{A}} = 100\,\text{V}$, then the input power would have been 100 W and the absorbed power P_{abs} turns out as the percentage of the transmitted over the input power. In particular this last quantity (the power transmitted to the plasma over the total input power) depends only on the plasma parameters and the gas density (through the collision frequency), not on the input power or voltage, nor on the value of the matching capacities:

$$\frac{P_{\text{abs}}}{P_{\text{in}}} = P_{\text{ratio}} = \frac{R_{\text{P}}}{R_{\text{L}}} \frac{\omega^2 L_{12}^2}{\omega^2 (L_{22} + L_{\text{P}})^2 + R_{\text{P}}^2} \tag{3.51}$$

The fraction of power transmitted to the plasma expressed as a percentage, for a gas temperature $T_{\mathrm{gas}} = 400\,\mathrm{K}$ and two different operating pressures, $p_{\mathrm{gas}} = 1.0\,\mathrm{Pa}$ and $p_{\mathrm{gas}} = 0.3\,\mathrm{Pa}$, is shown in Figure 3.13. It can be seen that the coupling between the coil field and the plasma decreases at low electron densities in both cases, but this is the range where the high density regime is no more valid (I extended this approach also to this zone by setting a maximum value for the skin depth equal to the chamber radius).

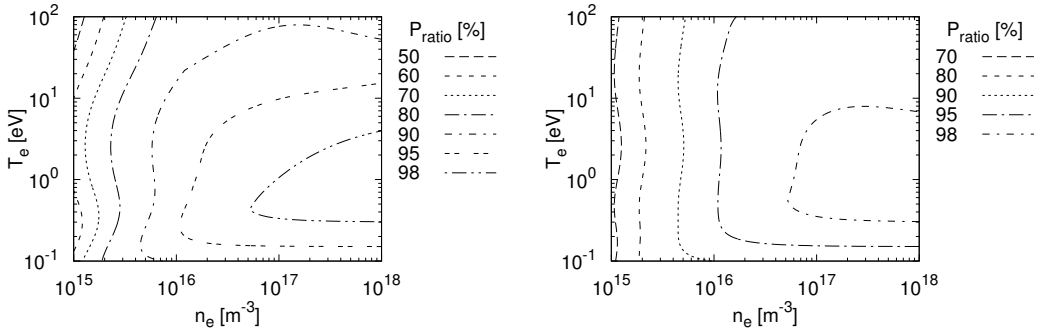

(a) $p_{\mathrm{gas}} = 0.3\,\mathrm{Pa}$ ($n_{\mathrm{gas}} = 5.4 \cdot 10^{19}\,\mathrm{m}^{-3}$). **(b)** $p_{\mathrm{gas}} = 1.0\,\mathrm{Pa}$ ($n_{\mathrm{gas}} = 1.8 \cdot 10^{20}\,\mathrm{m}^{-3}$).

Figure 3.13: Power percentage transmitted to a hydrogen plasma at two gas pressures and $T_{\mathrm{gas}} = 400\,\mathrm{K}$.

The values given in Figure 3.13 can be read as the power transmitted to the plasma in the case of:

- impedance matching for a power supply output tension $V_{\mathrm{A}} = 100\,\mathrm{V}$
- fixed input power $P_{\mathrm{in}} = 100\,\mathrm{W}$; actually this is the more common operation mode, as one is usually interested in the plasma behaviour at fixed input power.

3.3 Low density regime

In the low density regime the skin depth is greater than the chamber radius ($\delta > a$), so the constant electron density and temperature are now regarded as averages of those quantities over the volume. In this regime the fields fully penetrate the plasma, so the electric field inside the chamber can be expressed using the Faraday law:

$$E_\theta(r) = i\omega\mu_0 \frac{N\,\mathcal{K}_{\mathrm{b}}}{2l} I_{\mathrm{RF}}\, r \tag{3.52}$$

The power transmitted to the plasma is then calculated as a volume integration of the power density averaged over one period:

$$P_{\mathrm{plasma}} = \frac{1}{2}\int_V \mathrm{Re}(\sigma_{\mathrm{P}})\,|E_\theta|^2 = \frac{\pi e^2 n_{\mathrm{e}}}{16\,m_{\mathrm{e}}\,l}\left(\omega\,\mu_0\,N\,\mathcal{K}_{\mathrm{b}}\,I_{\mathrm{RF}}\,a^2\right)^2 \frac{\nu_{\mathrm{c}}}{\omega^2+\nu_{\mathrm{c}}^2} \tag{3.53}$$

As previously said in Section 3.1.5, the low density regime is effective when $n_e < 5 \cdot 10^{16}\,\mathrm{m}^{-3}$ or $T_e < 0.5\,\mathrm{eV}$: the power tranferred from the electric field to the plasma electrons in this regime is shown in Figure 3.14, where a coil current $I_{RF} = 10\,\mathrm{A}$ has been used. Taking a look at this figure and also considering (3.53), it can be seen that at high temperatures the power depends linearly on the electron density (collisions with neutral particles dominate), whereas at low temperatures the power increase with the density is slower and reaches a limit due to the dominance of coulomb collisions.

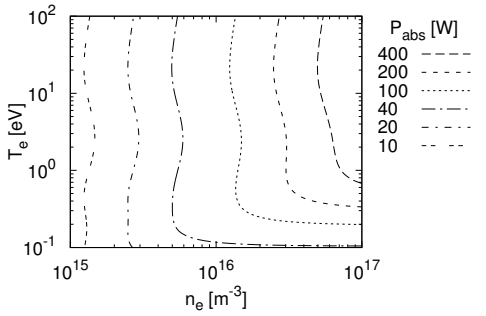

Figure 3.14: Power absorbed by the plasma in the low density regime at $I_{RF} = 10\,\mathrm{A}$.

In this simplified analytical model the power transmitted to the plasma has been expressed as a function of the electron density and temperature and of external parameters that can be set during the experimental session. If one sets the gas density inside the source, the voltage drop at the coil ends or the current flowing through the coil and the input power, then the measured absorbed power can give an estimate on the plasma parameters, namely the electron density and the electron temperature.

CHAPTER 4

Steady-state model for discharges in monospecies gas

The main aim of this chapter is to model the plasma in the source, in particular to obtain the electron temperature and density profiles in different experimental conditions using a relatively simple equation system. The software and the geometry used are described in Section 4.1, while the approximations and the equations used in the model are presented in Section 4.2.

In order to validate the model implementation in the multiphysics software used, a simple analytical solution for the plasma parameter profiles is given in Section 4.3; the numerical solutions obtained by implementing the model equations at different degrees of approximation are described in Section 4.4; it must be noted that finding the equilibrium solution for the electron density of plasma (even in very simplified models) requires a careful specification of the fixed parameters, especially in the numerical studies, in consideration of the typical positive feedback between electron heating and electron/ion production, as explained in this chapter.

Finally in Section 4.5 the model is applied to the case of a hydrogen discharge, comparing the simulation trends with those obtained in other numerical simulations, whereas in Section 4.6 the model is applied to the case of an air discharge, comparing the simulation trends with those obtained in NIO1 first experimental campaign.

4.1 Numerical simulations with COMSOL Multiphysics® software

The tool used to calculate the electron temperature and density in this chapter is the COMSOL Multiphysics® software (v. 3.5a) [25]. It is a general-purpose software platform for modeling and simulating physics-based problems, based on the finite element analysis (FEA). It includes various models, ranging from mechanical to chemical applications to user defined models (where the software just supply numerical and graphical models as a high level programming language) allowing the study of coupled systems or multiphysics problems in geometries up to 3 dimensions. To solve the equation system (usually partial differential equations) using the FEA, the geometry has to be divided in a subset of smaller elements, the mesh: the geometric shape of these mesh elements (e.g. triangular

in a 2D geometry) is separated from the finite element shape function, to allow for more flexibility. Once the equations in the geometry domain and the boundary conditions have been defined and the variables starting values are set, the problem can be solved and the simulation results can be visualised and further analyzed through the postprocessing tools.

In this section the whole plasma inside the NIO1 source will be studied, not only the region under the coil (as done in the previous chapter). The geometry used is the 2D axialsymmetric one in Figure 4.1: at the top there is the back region of the source, in the middle section the region under the coil and at the bottom the region near the plasma grid (which is placed at position z=0); the thick borders indicate the presence of the confining multipole magnets. The mesh used in this model is the triangular one (default mesh).

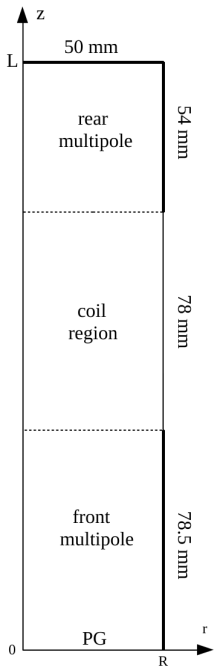

Figure 4.1: Geometry used in numerical simulations.

4.2 Diffusion and energy equations for electrons

The more important approximation used to model the plasma in the driver region is to consider a plasma with only one ion type (H_2^+ in the case of a H_2 plasma): this is generally not true, especially in molecular gases, but this approximation is adopted in order to simplify the problem [22]. The gas pressure and temperature are considered as external parameters (in particular $p_{\mathrm{gas}} = 1\,\mathrm{Pa}$ and $T_{\mathrm{gas}} = 400\,\mathrm{K}$ if not otherwise stated), thus defining the gas density; the ion temperature is taken equal to the neutral gas temperature, $T_{\mathrm{ion}} = T_{\mathrm{gas}}$ [26].

A first step is to write the stationary motion equation for electrons and ions by neglecting the inertial and convective terms (low velocities):

$$\begin{cases} 0 = -n_\mathrm{e} e(\vec{E} + \vec{u_\mathrm{e}} \times \vec{B}) - \nabla p_\mathrm{e} - m_\mathrm{e} n_\mathrm{e} \nu_\mathrm{ei}(\vec{u_\mathrm{e}} - \vec{u_\mathrm{i}}) - m_\mathrm{e} n_\mathrm{e} \nu_\mathrm{en} \vec{u_\mathrm{e}} \\ 0 = +n_\mathrm{i} e(\vec{E} + \vec{u_\mathrm{i}} \times \vec{B}) - \nabla p_\mathrm{i} - m_\mathrm{i} n_\mathrm{i} \nu_\mathrm{ie}(\vec{u_\mathrm{i}} - \vec{u_\mathrm{e}}) - m_\mathrm{i} n_\mathrm{i} \nu_\mathrm{in} \vec{u_\mathrm{i}} \end{cases} \tag{4.1}$$

where $\nu_\mathrm{ei}, \nu_\mathrm{ie}, \nu_\mathrm{en}, \nu_\mathrm{in}$ are respectively the electron-ion, ion-electron, electron-neutral, ion-neutral momentum transfer collision frequencies. In this first analysis the magnetic field $\vec{B}$ is neglected with respect to the other terms and since in this model the plasma contains one ion species only, the electron density is equal to the ion density ($n_\mathrm{e} = n_\mathrm{i} = n$). With these approximations and considering that $n_\mathrm{e} m_\mathrm{e} \nu_\mathrm{ei} = n_\mathrm{i} m_\mathrm{i} \nu_\mathrm{ie}$, (4.1) simplifies to:

$$\begin{cases} 0 = -ne\vec{E} - \nabla p_\mathrm{e} - m_\mathrm{e} n \nu_\mathrm{ei}(\vec{u_\mathrm{e}} - \vec{u_\mathrm{i}}) - m_\mathrm{e} n \nu_\mathrm{en} \vec{u_\mathrm{e}} \\ 0 = +ne\vec{E} - \nabla p_\mathrm{i} - m_\mathrm{i} n \nu_\mathrm{ei}(\vec{u_\mathrm{i}} - \vec{u_\mathrm{e}}) - m_\mathrm{i} n \nu_\mathrm{in} \vec{u_\mathrm{i}} \end{cases} \tag{4.2}$$

It will be shown that the temperature gradient is negligible with respect to the density gradient, so $\nabla p = k_B T \nabla n$; then by adding the two equations in (4.2) one obtains:

$$0 = -k_B(T_\mathrm{e} + T_\mathrm{i})\nabla n - (m_\mathrm{e}\nu_\mathrm{en} + m_\mathrm{i}\nu_\mathrm{in})\vec{\Gamma} \tag{4.3}$$

where an ambipolar flux has been assumed, so that $\vec{\Gamma} = n\vec{u_\mathrm{e}} = n\vec{u_\mathrm{i}}$. By rewriting (4.3) in a more convenient way, the diffusion equation is readily obtained:

$$\vec{\Gamma} = -D_\mathrm{a}\nabla n = -\frac{k_B(T_\mathrm{e} + T_\mathrm{i})}{m_\mathrm{e}\nu_\mathrm{en} + m_\mathrm{i}\nu_\mathrm{in}}\nabla n \tag{4.4}$$

Noting that $T_\mathrm{e} \gg T_\mathrm{i}$ and that $m_\mathrm{i}\nu_\mathrm{in} > m_\mathrm{e}\nu_\mathrm{en}$, the ambipolar diffusion coefficient can be rewritten in this form:

$$D_\mathrm{a} \simeq \frac{T_\mathrm{e}}{m_\mathrm{i}\nu_\mathrm{i}} \tag{4.5}$$

where now $\nu_\mathrm{in} = \nu_\mathrm{i}$ for the sake of brevity. The ion collision frequency is calculated as $\nu_\mathrm{i} = n_\mathrm{gas}\langle\sigma_\mathrm{i} u_\mathrm{i}\rangle$, where σ_i is the ion-neutral cross-section. Since σ_i is almost constant in this gas and ionic temperature range ($T_\mathrm{ion} = T_\mathrm{gas} \simeq 0.25\,\mathrm{meV}$), then:

$$\nu_\mathrm{i} = \frac{\langle u_\mathrm{i}\rangle}{\lambda_\mathrm{i}} \tag{4.6}$$

where λ_i is the ion mean free path. A list of the ion-neutral cross-sections used is given in Table 4.1.

The diffusion coefficient is then:

$$D_\mathrm{a} \simeq \frac{T_\mathrm{e}\lambda_\mathrm{i}}{m_\mathrm{i} u_\mathrm{i,th}} \frac{u_\mathrm{i,th}}{\langle u_\mathrm{i}\rangle} = D_\mathrm{a0}\frac{u_\mathrm{i,th}}{\langle u_\mathrm{i}\rangle} \tag{4.7}$$

Table 4.1: Ion-neutral cross sections.

	σ_i	Ref.
$\mathbf{H}_2^+$-$\mathbf{H}_2$	$2.13 \cdot 10^{-19}\,\mathrm{m}^{-2}$	[20]
$\mathbf{N}_2^+$-$\mathbf{N}_2$	$1.77 \cdot 10^{-18}\,\mathrm{m}^{-2}$	[27]
$\mathbf{O}_2^+$-$\mathbf{O}_2$	$6.67 \cdot 10^{-19}\,\mathrm{m}^{-2}$	[28]

where $u_\mathrm{i,th}$ is the ion thermal velocity:

$$u_\mathrm{i,th} = \sqrt{\frac{8k_B T_\mathrm{i}}{\pi m_\mathrm{i}}} \tag{4.8}$$

One can write two different expressions for the mean ion velocity $\langle u_\mathrm{i} \rangle$, depending on the pressure regime considered:

- high pressure: the ion drift velocity remains smaller than the thermal velocity due to collisions, so the average speed is equal to the thermal speed, $\langle u_\mathrm{i} \rangle = u_\mathrm{i,th}$. The diffusion coefficient is then $D_\mathrm{a} = D_\mathrm{a0}$.
- low pressure: the ion drift velocity is not negligible compared to the thermal velocity, so the mean velocity takes the form

  $$\langle u_\mathrm{i} \rangle = \sqrt{u_\mathrm{i,th}^2 + u_\mathrm{drift}^2} \tag{4.9}$$

  In this case the diffusion coefficient depends on the density gradient and its expression will be given in Section 4.4.2.

The continuity equation for electrons reads:

$$\nabla \cdot \vec{\Gamma} = \nu_\mathrm{iz} n \tag{4.10}$$

where ν_iz is the frequency of ionizing electron-neutral collisions, previously called $\nu_\mathrm{en}^{(iz)}$. Using this and (4.4) the first equation of the model is then:

$$\nabla \cdot (-D_\mathrm{a} \nabla n) = \nu_\mathrm{iz}\, n \tag{4.11}$$

The second equation to use is the electron energy equation which, in stationary conditions and upon neglecting convection terms [29], is:

$$\nabla \cdot (-K_\mathrm{e} \nabla T_\mathrm{e}) = p_\mathrm{abs} - \varepsilon_\mathrm{L}\, n\, \nu_\mathrm{iz} \tag{4.12}$$

where:

- p_abs: the power density transferred to the electrons in the plasma via the RF

inductive coupling, and can be either given as an external parameter or can be calculated by considering the electric field generated by the coils;

- ε_{L}: the electron energy loss per ionizing collision. It is defined as [10]:

$$k_{\mathrm{iz}}\,\varepsilon_{\mathrm{L}} \equiv k_{\mathrm{iz}}\,\varepsilon_{\mathrm{iz}} + \sum_{\mathrm{i}} k_{\mathrm{exc,i}}\,\varepsilon_{\mathrm{exc,i}} + k_{\mathrm{el}}\,\frac{3\,m_{\mathrm{e}}}{m_{\mathrm{i}}}\,T_{\mathrm{e}} \tag{4.13}$$

  where k_{iz}, $k_{\mathrm{exc,i}}$, k_{el} are respectively the ionization, excitation, elastic collision reaction rates and $\varepsilon_{\mathrm{iz}}$ and $\varepsilon_{\mathrm{exc,i}}$ are respectively the energy lost during an ionization and excitation scattering against neutral atoms. The function $\varepsilon_{\mathrm{L}}(T_{\mathrm{e}})$ has been calculated in detail for hydrogen, nitrogen and oxigen plasmas in Appendix A.2;

- K_{e}: the plasma thermal conductivity [30]:

$$K_{\mathrm{e}} = \frac{5\,n\,k_B^2\,T_{\mathrm{e}}}{2\,m_{\mathrm{e}}\,\nu_{\mathrm{en}}} \tag{4.14}$$

If there are no multipole magnets confining the plasma, the particle and heat fluxes are set equal to those at the Debye sheath edge, by assuming the Debye length small compared to the driver dimensions. In this way the boundary condition for the continuity equation is:

$$\hat{n}\cdot(-D_{\mathrm{a}}\nabla n) = n\,c_{\mathrm{s}} \tag{4.15}$$

where c_{s} is the ion sonic speed:

$$c_{\mathrm{s}} = \sqrt{\frac{k_B\,T_{\mathrm{e}}}{m_{\mathrm{i}}}} \tag{4.16}$$

The boundary condition for the energy equation is instead [10]:

$$\hat{n}\cdot(-K_{\mathrm{e}}\nabla T_{\mathrm{e}}) = \left(\frac{1}{2} + \frac{1}{2}\ln\frac{m_{\mathrm{i}}}{2\,\pi\,m_{\mathrm{e}}} + 2\right) n\,c_{\mathrm{s}}\,k_B\,T_{\mathrm{e}} = \eta\,n\,c_{\mathrm{s}}\,k_B\,T_{\mathrm{e}} \tag{4.17}$$

where the electron energy flux is the sum of the kinetic energy lost per electron lost and the energy gained by the ion as it traverses the sheath; $\hat{n}$ is the vector of length one perpendicular to the surface.

4.3 Fixed input power and high pressure: analytical solution

As said in the previous section, the approximation $D_{\mathrm{a}} = D_{\mathrm{a0}}$ holds in the high pressure regime. An analytical solution to the problem can be found by making the following assumptions:

- T_{e} is uniform; this is a good approximation to the real temperature profile [31], even

if in a more realistic situation the temperature is expected to be position-dependent (in particular to be higher in the coil region);

- p_{abs} is uniform ($p_{\mathrm{abs}} = P_{\mathrm{abs}}/V$);

In this way the continuity equation becomes linear:

$$\nabla n = -\frac{\nu_{\mathrm{iz}}(T_{\mathrm{e}})}{D_{\mathrm{a0}}(T_{\mathrm{e}})} n \tag{4.18}$$

A simple analytical solution in cylindrical coordinates is:

$$n(r,z) = n_0\, J_0(\gamma\, r) \cos(k(z - L/2)) \tag{4.19}$$

This eigenvalue problem can be solved by substituting (4.19) in (4.18) and (4.15) (boundary conditions at r=R=0.05 m and z=L=0.2105 m), thus obtaining a system that can be solved numerically:

$$\begin{cases} \frac{\nu_{\mathrm{iz}}(T_{\mathrm{e}})}{D_{\mathrm{a0}}(T_{\mathrm{e}})} = \gamma^2 + k^2 \\ k\, \tan(k\, \frac{L}{2}) = \frac{c_{\mathrm{s}}}{D_{\mathrm{a0}}} \\ \gamma\, \frac{J_1(\gamma R)}{J_0(\gamma R)} = \frac{c_{\mathrm{s}}}{D_{\mathrm{a0}}} \end{cases} \tag{4.20}$$

The solution found using Mathematica 9.0 for a molecular hydrogen gas at a pressure $p_{\mathrm{gas}} = 1\,\mathrm{Pa}$ and temperature $T_{\mathrm{gas}} = 400\,\mathrm{K}$, considering only H_2^+ ions at a temperature $T_{\mathrm{ion}} = 400\,\mathrm{K}$, is:

$$\begin{cases} k = 5.71\,\mathrm{m}^{-1} \\ \gamma = 12.0\,\mathrm{m}^{-1} \\ T_{\mathrm{e}} = 9.50\,\mathrm{eV} \end{cases} \tag{4.21}$$

In this way a solution for the constant electron temperature and for the density profile is found . To find a solution also for n_0 one has to consider the energy balance, which, according to (4.12) and (4.17) and using (4.11), is:

$$\int_V p_{\mathrm{abs}}\, dV = \varepsilon_{\mathrm{L}} \int_V n\, \nu_{\mathrm{iz}}\, dV + \oint_\Sigma \eta\, k_B\, T_{\mathrm{e}}\, n\, c_{\mathrm{s}}\, d\Sigma = \varepsilon_{\mathrm{L}} \oint_\Sigma n\, c_{\mathrm{s}}\, d\Sigma + \eta\, k_B\, T_{\mathrm{e}} \oint_\Sigma n\, c_{\mathrm{s}}\, d\Sigma \tag{4.22}$$

so the total input power P_{abs} is:

$$P_{\mathrm{abs}} = (\varepsilon_{\mathrm{L}} + \eta\, k_B\, T_{\mathrm{e}}) \oint_\Sigma n\, c_{\mathrm{s}}\, d\Sigma = \varepsilon_T \oint_\Sigma n\, c_{\mathrm{s}}\, d\Sigma \tag{4.23}$$

After integration one obtains the following expression for the maximum density:

$$n_0 = \frac{P_{\text{abs}}}{c_s\,\varepsilon_T}\frac{\gamma\,k}{4\,\pi\,R\,(k\,J_1(\gamma R)\cos(kL/2)+\gamma\,J_0(\gamma R)\sin(kL/2))} \tag{4.24}$$

As can be seen, in this model:

- the electron temperature and the density profile do not depend on the input power but only on the gas density and the ion temperature;
- there is a linear dependence between the maximum density and the total input power.

The results obtained using this analytical model and an input power $P_{\text{abs}} = 2\,\text{kW}$ are given in Figure 4.2(a) and Figure 4.2(b) (dashed lines). The profiles are plotted as a function of normalized radial and axial coordinates , r' and z', defined as follows:

$$\begin{cases} r' = \frac{r}{R} \\ z' = \frac{z-L/2}{L/2} \end{cases} \tag{4.25}$$

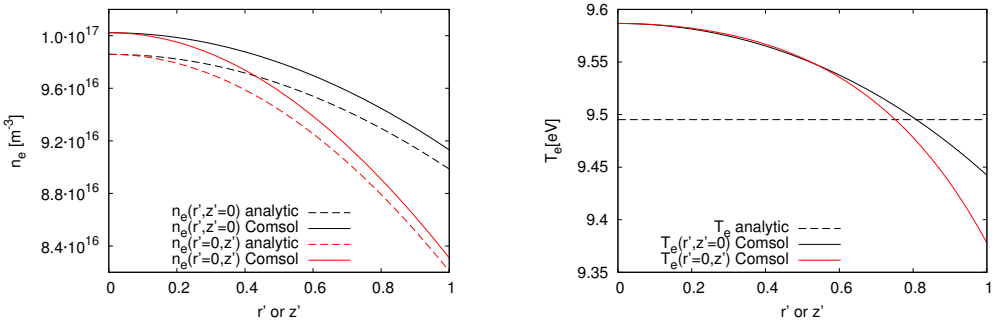

(a) Electron radial and axial density profiles (normalized lengths, (4.25)).

(b) Electron radial and axial temperature profiles (normalized lengths, (4.25)).

Figure 4.2: T_{e} and n_{e} profiles in a H_2 plasma, $P_{\text{abs}} = V\,p_{\text{abs}} = 2\,\text{kW}$, high density approximation, $T_{\text{gas}} = T_{\text{ion}} = 400\,\text{K}$, $p_{\text{gas}} = 1\,\text{Pa}$

4.4 Model numerical implementation

In this section I will implement the model proposed in Section 4.2 and summarized in Table 4.2 in COMSOL Multiphysics® at different degrees of approximation for a hydrogen discharge containing the H_2^+ ionic species only. The external parameters used, unless otherwise stated, are the previous ones, namely: $T_{\text{gas}} = T_{\text{ion}} = 400\,\text{K}$ and $p_{\text{gas}} = 1\,\text{Pa}$.

Table 4.2: Model equations.

	subdomain equations	**boundary conditions**
continuity	$\nabla \cdot (-D_\mathrm{a} \nabla n) = \nu_\mathrm{iz}\, n$	$\hat{n} \cdot (-D_\mathrm{a} \nabla n) = n\, c_\mathrm{s}$
energy	$\nabla \cdot (-K_\mathrm{e} \nabla T_\mathrm{e}) = p_\mathrm{abs} - \varepsilon_\mathrm{L}\, n\, \nu_\mathrm{iz}$	$\hat{n} \cdot (-K_\mathrm{e} \nabla T_\mathrm{e}) = \eta\, n\, c_\mathrm{s}\, k_B\, T_\mathrm{e}$

4.4.1 Uniform power density deposition and high pressure regime

To verify the correct implementation in COMSOL of the equations in Table 4.2, I first considered the high pressure regime, with conditions as close as possible to the analytical solution in order to make a significant comparison possible. Again, p_abs and $D_\mathrm{a} = D_\mathrm{a0}$ are considered uniform over the volume, but in order to find the electron density from (4.18), the electron temperature cannot be considered constant as done in the analytical model (in which the energy equation is considered in its integral form). It should be noted that taken separately equation (4.18) is an eigenvalue problem for n_e, with an infinite number of solutions for some T_e values, and no solution for other T_e, while (4.12) is an inhomogenous equation for T_e thanks to the fixed p_abs term; the coupling for n_e and T_e allows to determine a unique solution, provided coupling is correctly specified.

Using the same external parameters, the simulation gives the results plotted in Figure 4.2(a) and Figure 4.2(b) (continuous lines): as can be seen there is good agreement between this result and the analytical solution, so the model implementation in COMSOL is correct.

4.4.2 Uniform power density deposition and low pressure regime

In a low pressure regime, the ion drift velocity is not negligible compared to the thermal velocity, so (4.9) has to be used, where the drift velocity is related to the particle flux:

$$\Gamma = n\, u_\mathrm{drift} \tag{4.26}$$

The general expression for the diffusion coefficient is that given in (4.7), where an explicit expression for the drift velocity has to be found. To do so one can equate the modulus of the fluxes given in (4.4) and (4.26):

$$\left(n\, u_\mathrm{i,th}\, \frac{u_\mathrm{drift}}{u_\mathrm{i,th}}\right)^2 = D_\mathrm{a0}^2\, \frac{1}{1 + \left(\frac{u_\mathrm{drift}}{u_\mathrm{i,th}}\right)^2} \left[\left(\frac{\partial n}{\partial r}\right)^2 + \left(\frac{\partial n}{\partial z}\right)^2\right] \tag{4.27}$$

By solving for $u_\mathrm{drift}/u_\mathrm{i,th}$ and then substituting in (4.7), one obtains:

$$D_\mathrm{a} = \frac{\sqrt{2}\, D_\mathrm{a0}}{\sqrt{1 + \sqrt{1 + 4\, \left(\frac{D_\mathrm{a0}}{n\, u_\mathrm{i,th}}\right)^2 \left[\left(\frac{\partial n}{\partial r}\right)^2 + \left(\frac{\partial n}{\partial z}\right)^2\right]}}} \tag{4.28}$$

The use of this expression for the diffusion coefficient in numerical simulations is relatively straightforward, since the square root arguments are positively defined; it yields the profiles in Figure 4.3, where the densities have been normalized to the density at the center of the chamber n_0. With respect to the high density model the plasma parameters show:

- a higher electron density at the center of the chamber ($n_0 = 9.7 \cdot 10^{16}\,\mathrm{m}^{-3}$ in the high density regime and $n_0 = 2.0 \cdot 10^{17}\,\mathrm{m}^{-3}$ in the low density regime);
- a density profile steeper at the edge of the chamber;
- a lower electron temperature.

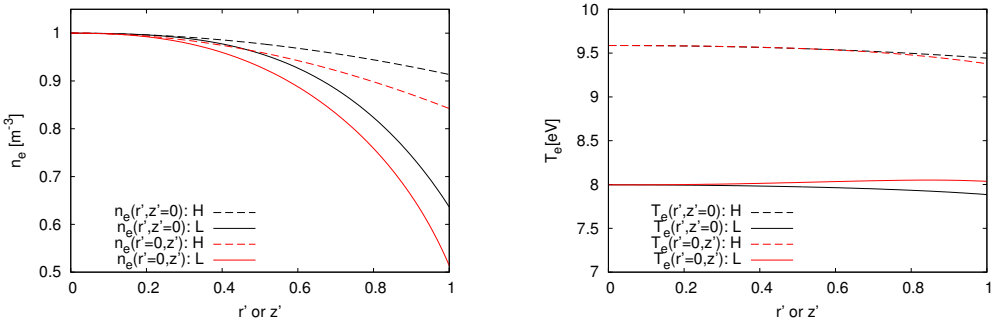

(a) Radial and axial electron density profiles (normalized density).

(b) Radial and axial electron temperature profiles.

Figure 4.3: T_e and n_e profiles in a H_2 plasma, $P_\mathrm{abs} = 2\,\mathrm{kW}$, in the high density (H) and low density (L) regimes.

All the profiles obtained, in addition to the cylindrical symmetry, are symmetrical with respect to the center of the chamber, since the presence of the coils (which introduce a non-uniform power deposition) or the magnets has not been considered yet.

4.4.3 RF power deposition

In this paragraph a more physical power absorption profile will be introduced by considering the power transferred to the plasma electrons from the electric field generated by the coil. By following the reasoning in Section 3.3, the electric field under the coils can be expressed as:

$$E_\theta(r) = i\omega\mu_0 \frac{N\,\mathcal{K}_b}{2l} I_\mathrm{RF}\, r \tag{4.29}$$

To simulate the axial dependence of the electric field, this formula has been multiplied by a custom function $f(z)$, which is approximately 1 under the coils and smoothly goes to zero elsewhere (see Figure 4.4, the dashed vertical lines indicate the coil position).

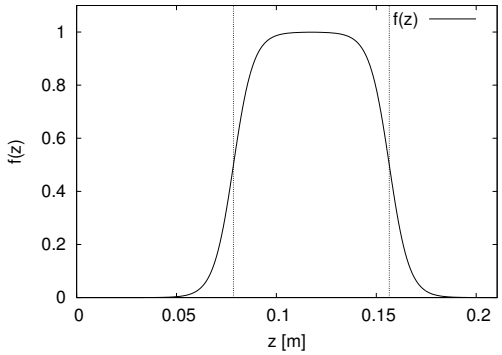

Figure 4.4: Function f(z) used to simulate the axial dependence of the electric field.

The power density in this region is then:

$$p_{\text{abs}} = \frac{1}{2}\text{Re}(\sigma_P)\,|E_\theta(r,z)|^2 = \frac{1}{2}\frac{n_\text{e}\,e^2}{m_\text{e}}\frac{\nu_c}{\nu_c^2+\omega^2}\,f(z)^2\;|E_\theta(r)|^2 \tag{4.30}$$

with $\nu_c = \nu_m + \nu_{stoc}$ as calculated in Section 3.1. Using again the equations in Table 4.2 where now p_{abs} is as in (4.30), the simulation produces the profiles in Figure 4.5 for a total power deposition $P_{\text{abs}} = 2\,\text{kW}$ (obtained with $I_{\text{RF}} = 14.7\,\text{A}$). The profiles

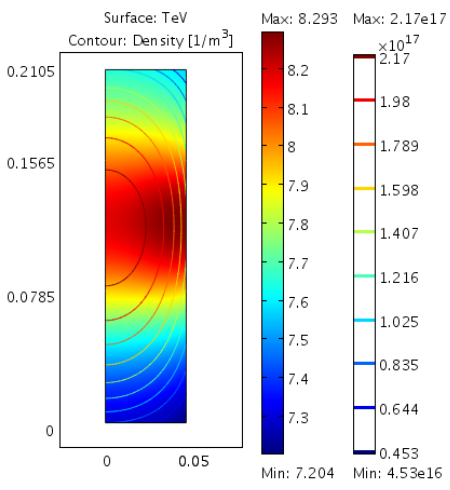

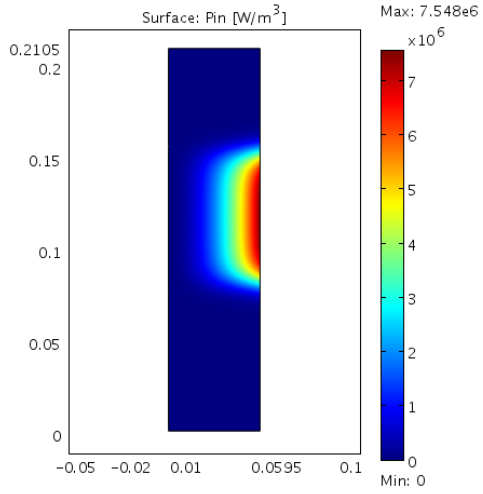

(a) Electron density and temperature profiles. **(b)** Power density profile.

Figure 4.5: Profiles obtained in a H_2 plasma, $P_{\text{abs}} = 2\,\text{kW}$, considering a ohmic power deposition.

are no longer symmetrical with respect to the center of the chamber, in particular the maximum density and temperature are located under the coil (positioned between $z =$

0.0785 m and $z = 0.1565$ m, $z = 0$ corresponds to the plasma grid) due to the power density profile given in Figure 4.5(b). This effect can be clearly seen when making a comparison with the previous profiles: in Figure 4.6 and Figure 4.7 there are respectively the axial and radial profiles in the case of a uniform power density (P_{unif}, dashed line) and a localized power density (P_{ohm}, continuous line).

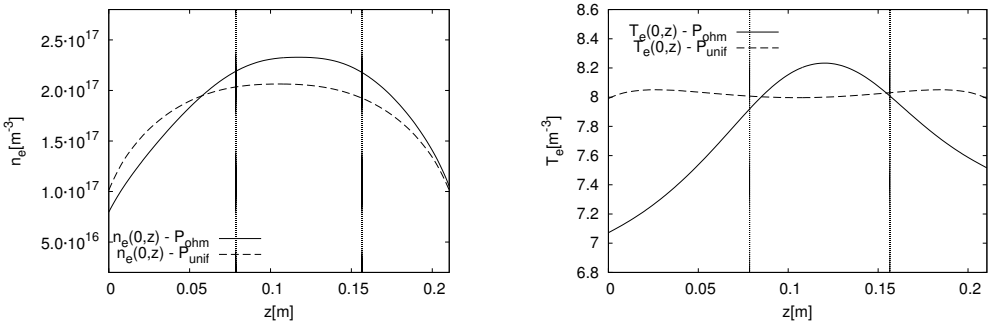

(a) Axial electron density. **(b)** Axial electron temperature.

Figure 4.6: Comparison between the profiles on the chamber's axis; the dashed vertical lines indicate the coil position.

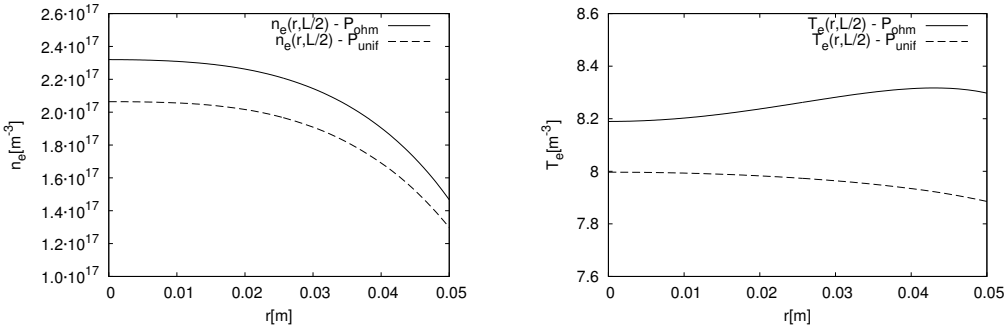

(a) Radial electron density. **(b)** Radial electron temperature.

Figure 4.7: Comparison between the radial profiles at the middle of the axis chamber.

4.4.4 Magnetic multipole confinement

Until now the confining effect of the magnetic multipoles has not been considered: the outward fluxes were those at the plasma sheath for a plasma confined only by a metal surface. To introduce magnetic confinement the approach described in [10, pp. 155–159] can be used, in which a set of alternating rows of north and south poles of permanent magnets is placed around the surface of a cylindrical chamber: the alternating rows of magnets generate a line cusp magnetic configuration in which the magnetic field strength B is maximum near the magnets and decays with distance when entering into the chamber. To model the outward particle flux in this magnetic configuration one can introduce the concept of the effective leak width w of a line cusp. If there are N cusps

of width w, then the effective circumferential loss width is $N\,w$ and the fraction f_{loss} of diffusing electron–ion pairs that will be lost to the wall is [10]

$$f_{\mathrm{loss}} = \frac{N\,w}{2\,\pi\,R} \tag{4.31}$$

where, considering NIO1, $N = 14$ and $R = 0.05\,\mathrm{m}$. The boundary condition at the wall for the ambipolar diffusion of plasma within the field-free discharge volume is now

$$\hat{n} \cdot \Gamma = f_{\mathrm{loss}}\, n\, c_{\mathrm{s}} \tag{4.32}$$

An estimate of the leak width for intermediate pressures has been given in [32]:

$$w \simeq \frac{2}{\pi}(\langle r_{\mathrm{Le}}\rangle\,\langle r_{\mathrm{Li}}\rangle)^{1/2}\frac{d}{(\lambda_{\mathrm{e}}\,\lambda_{\mathrm{i}})^{1/2}} \tag{4.33}$$

where $\langle r_L\rangle$ is the mean Larmor radius, λ is the mean free path and d is the distance between the permanent magnets. So, neglecting the electron-ion collisions and considering that $d = 2\,\pi\,R/N$, the fraction of diffusing electron–ion pairs is:

$$\begin{aligned} f_{\mathrm{loss}} &= \frac{2}{\pi}\left(\frac{m_{\mathrm{e}}\,\langle v_{\perp\mathrm{e}}\rangle}{e\,B}\,\frac{m_{\mathrm{i}}\,\langle v_{\perp\mathrm{i}}\rangle}{e\,B}\right)^{1/2}(n_{\mathrm{gas}}\sigma_{\mathrm{e}}\,n_{\mathrm{gas}}\sigma_{\mathrm{i}})^{1/2} \\ &= \frac{2\,n_{\mathrm{gas}}\,\sqrt{m_{\mathrm{e}}\,m_{\mathrm{i}}\,\sigma_{\mathrm{i}}}}{\pi\,e\,B}\sqrt{\langle v_{\perp\mathrm{i}}\rangle\,\langle v_{\perp\mathrm{e}}\rangle\,\sigma_{\mathrm{e}}} \end{aligned} \tag{4.34}$$

which, for a given gas density and ion type, depends only on the electron temperature. The eletron and ion velocities can be written using (4.9), where the drift velocity is now calculated at the boundary ($u_{\mathrm{drift}} = c_{\mathrm{s}}$):

$$\langle v_{\perp}\rangle = \sqrt{\left(\frac{2}{3}\,v_{\mathrm{th}}\right)^2 + \frac{k_B\,T_{\mathrm{e}}}{m_{\mathrm{i}}}} \tag{4.35}$$

In NIO1 the magnetic field at the boundary (near the coil) given by numerical simulations is about 4 mT [14]: by considering this value for the magnetic field and the total electron-neutral collision cross-sections in Figure 4.8 ([19],[33] and [34]), one obtains for f_{loss} the results in Figure 4.9; it is to be noted that in some magnetic configurations possible in NIO1, the magnetic field rises on lateral walls away from the coil over 0.1 T, so that lower f_{loss} values could be obtained.

As can be seen in this graph, a hydrogen plasma is better confined and the confinement is worse at higher temperatures; these results are obtained for $T_{\mathrm{gas}} = 400\,\mathrm{K}$ and $p_{\mathrm{gas}} = 1\,\mathrm{Pa}$, so to calculate f_{loss} at different pressures the values in Figure 4.9 have to be multiplied by the operation pressure: in particular the lower the pressure, the more effective the confinement. Of course, since f_{loss} represents the fraction of diffusing electron–ion pairs that are lost to the wall, it is always smaller than 1 ($f_{\mathrm{loss}} \leq 1$): if by

application of (4.34) a value $f_{\text{loss}} > 1$ is obtained, then it is assumed that all diffusing electron–ion pairs are lost to the wall, that is $f_{\text{loss}} = 1$.

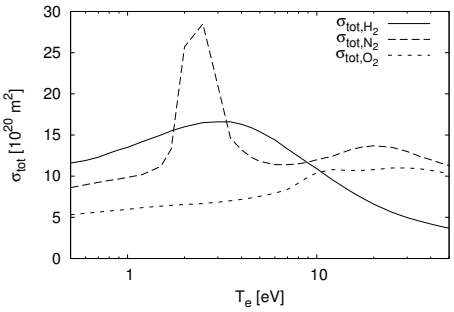

Figure 4.8: σ_{tot} for electron collisions H_2, N_2 and O_2 gases.

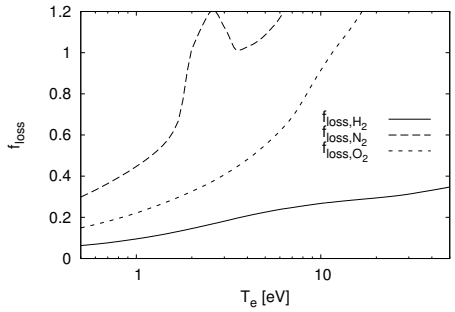

Figure 4.9: f_{loss} for H_2, N_2 and O_2 discharges, $n_{\text{gas}} = 1.8 \cdot 10^{20}\,\text{m}^{-3}$.

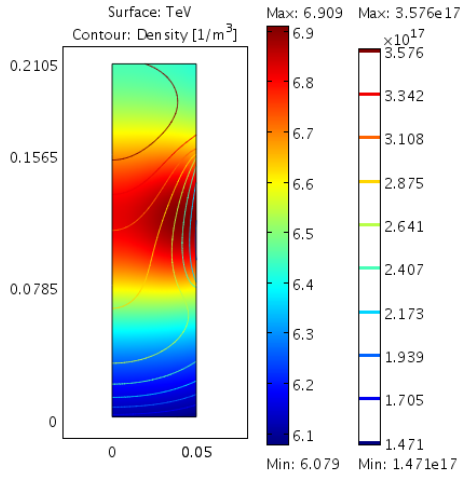

(a) Profiles for the ohmic p_{abs} in (4.30).

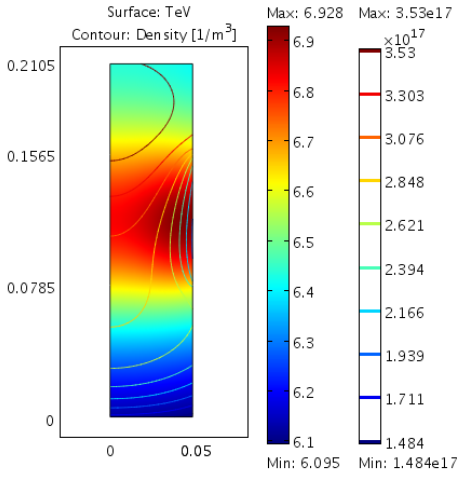

(b) Profiles for the custom p_{abs} in (4.38).

Figure 4.10: T_{e} and n_{e} profiles in a H_2 plasma, $P_{\text{abs}} = 2\,\text{kW}$, obtained considering the magnetic multipole confinement.

Finally the confining effect of the multipole magnets can be included in the numerical model by changing the boundary conditions at the walls where magnets are present (thick borders in Figure 4.1) to:

$$\begin{aligned} \hat{n} \cdot (-D_{\text{a}} \nabla n) &= f_{\text{loss}}\, n\, c_{\text{s}} \\ \hat{n} \cdot (-K_{\text{e}} \nabla T_{\text{e}}) &= f_{\text{loss}}\, \eta\, n\, c_{\text{s}}\, k_B\, T_{\text{e}} \end{aligned} \tag{4.36}$$

Using these boundary conditions and the usual subdomain equations, the simulation produces the profiles in Figure 4.10(a) for a hydrogen plasma and a 2 kW total absorbed

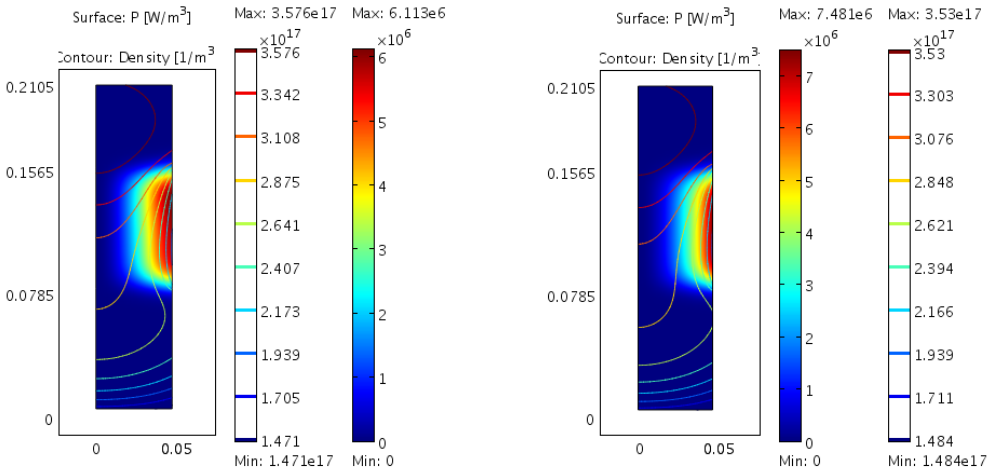

(a) Ohmic p_{abs} profile.

(b) Custom p_{abs} profile.

Figure 4.11: Power density profiles in a H_2 plasma, $P_{\text{abs}} = 2\,\text{kW}$, obtained considering the magnetic multipole confinement.

power (now obtained with a lower coil current $I_{\text{RF}} = 12.5\,\text{A}$). As can be seen when comparing this result with Figure 4.5(a):

- the electron density increases and is more uniform across the volume, which gives a better control on the plasma parameters;
- the electron temperature decreases and it is more uniform across the volume; the first effect is due the fact that now, because of the magnetic confinement, the electrons travel a longer distance before being lost to the walls, thus requiring a lower temperature to sustain the discharge.

4.4.5 Simplified power density profile

The expression for the absorbed power density given in Section 4.4.3 can be simplified in order to make the simulation convergence easier. As can be seen from (4.30), if the plasma conductivity is constant over the volume, p_{abs} radial and axial dependence are the following ones:

$$p_{\text{abs}} \propto f(z)^2\, r^2 \tag{4.37}$$

As can be seen in Figure 4.11(a), the region where there is the main power absorption is limited to a relatively thin zone under the coil, where one can approximate the plasma conductivity to a constant. In this way, instead of (4.30), a custom expression for the

power density can be used:

$$p_{\text{abs}} = P_{\text{abs}} \frac{f(z)\, r^2}{2\pi\, R^4/4 \cdot \int_z f(z)} \tag{4.38}$$

where P_{abs} is the total power transmitted to the plasma. Setting P_{abs} to the usual 2 kW, the results obtained are those in Figure 4.10(b). As can be seen, the electron

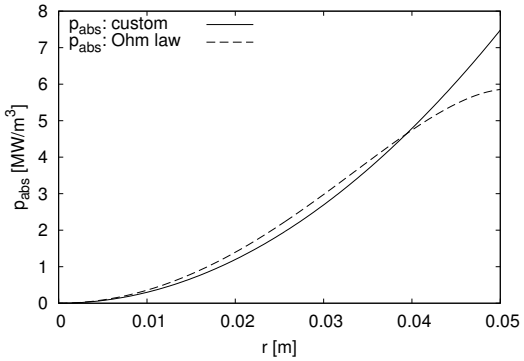

Figure 4.12: Comparison between p_{abs} for an ohmic dissipation and the one in (4.38).

density and temperature profiles are almost identical to those obtained in Figure 4.10(a): the small differences are due to the differences in the power density profiles between the ohmic power deposition model and the custom profile (see Figure 4.11 and 4.12), especially at the border where there is a stronger density gradient. This approximation is then valid and it will be used in those cases where the convergence is hard to reach.

4.5 Plasma parameters in a hydrogen discharge

In this section I will apply the model described in Section 4.2 to a H_2 discharge containing the H_2^+ ionic species only, considering an ohmic power deposition and the multipole confinement described in the previous section.

4.5.1 Power dependence

Keeping the gas density fixed ($T_{\text{gas}} = 400\,\text{K}$, $p_{\text{gas}} = 1\,\text{Pa}$), the total power transferred to the plasma is changed by varying the current I_{RF} flowing through the coils. When performing the simulation, the following results are obtained (see Figure 4.13):

- the electron temperature does not change with the input power. This is due to the fact that T_{e} is determined by particle conservation through the continuity equation, so it is independent from the plasma density and therefore the input power;
- the electron density depends linearly on the total input power. In fact, the energy

equation in Table 4.2 can be integrated as follows:

$$\int_V p_{\mathrm{abs}}\, dV = P_{\mathrm{abs}} = \int_V \varepsilon_{\mathrm{L}}(T_{\mathrm{e}})\, \nu_{\mathrm{iz}}(T_{\mathrm{e}})\, n_{\mathrm{e}}\, dV + \oint_\Sigma \eta\, c_{\mathrm{s}}\, k_B\, T_{\mathrm{e}}\, n_{\mathrm{e}}\, d\Sigma \tag{4.39}$$

As the temperature profile remains unchanged, if P_{abs} increases by a factor κ ($P'_{\mathrm{abs}} = \kappa P_{\mathrm{abs}}$), then $T'_{\mathrm{e}} = T_{\mathrm{e}}$ and n'_{e} obeys the following relation:

$$\int_V \varepsilon_{\mathrm{L}}\, \nu_{\mathrm{iz}}\, (\kappa n_{\mathrm{e}} - n'_{\mathrm{e}})\, dV + \oint_\Sigma \eta\, c_{\mathrm{s}}\, k_B\, T_{\mathrm{e}}\, (\kappa n_{\mathrm{e}} - n'_{\mathrm{e}})\, d\Sigma \tag{4.40}$$

which is satisfied if $n'_{\mathrm{e}} = \kappa n_{\mathrm{e}}$;

- there is a threshold current (approximately 13A, which corresponds to a 50 W input power) over which the plasma is turned on (over which there is a significant total power deposition).

It is worth noting that in this model the dependencies of plasma parameters at fixed pressure (the electron density increases linearly with applied power whereas the temperature profile does not change) do not depend on the type of gas used, so they will still be valid in the discharges in O_2 and N_2 simulated in the next section.

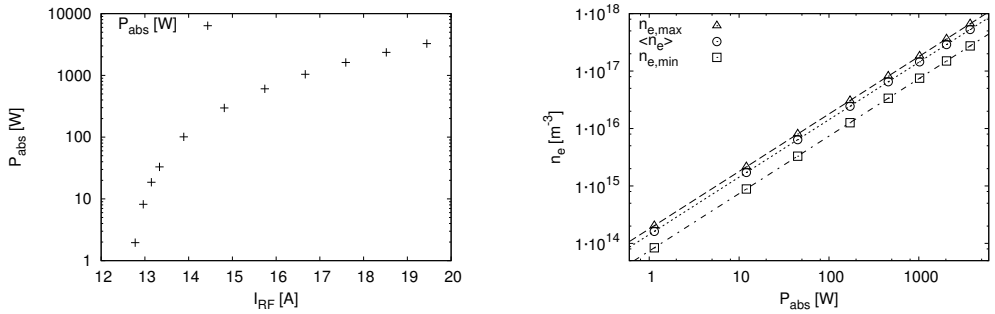

(a) Total absorbed power as a function of the coil current.

(b) Electron density as a function of the total absorbed power.

Figure 4.13: P_{abs} and n_{e} dependencies at fixed pressure $p = 1\,\mathrm{Pa}$.

4.5.2 Pressure dependence

In this case the gas temperature and the total power deposition will be kept fixed ($T_{\mathrm{gas}} = 400\,\mathrm{K}$, $P_{\mathrm{abs}} = 2000\,\mathrm{W}$), while the gas pressure ranges from 0.2 Pa to 10 Pa; note that the gas density was considered fixed in this model, neglecting selfpumping effect at this stage. The simulation results are plotted in Figure 4.14, 4.15, 4.16 and 4.17.

The profiles obtained in three particular cases ($p_{\mathrm{gas}} = 0.3, 3, 10\,\mathrm{Pa}$), are shown in Figure 4.14 and 4.15, where the following behaviours can be noticed:

- the temperature decreases with increasing pressure, whereas the electron density increases;

- at higher pressures both the temperature and density profiles become steeper, in particular their peak is under the coil (where there is the main power deposition);
- at lower pressures the peak in the density profile moves towards the back of the chamber because in this region the magnetic confinement is more effective. The electron temperature profile still has its peak in the higher electric field zone, but is more uniform over the volume.
- at higher pressures the radial profile of the absorbed power density decreases towards the wall because of the steepening in the electron density profile.

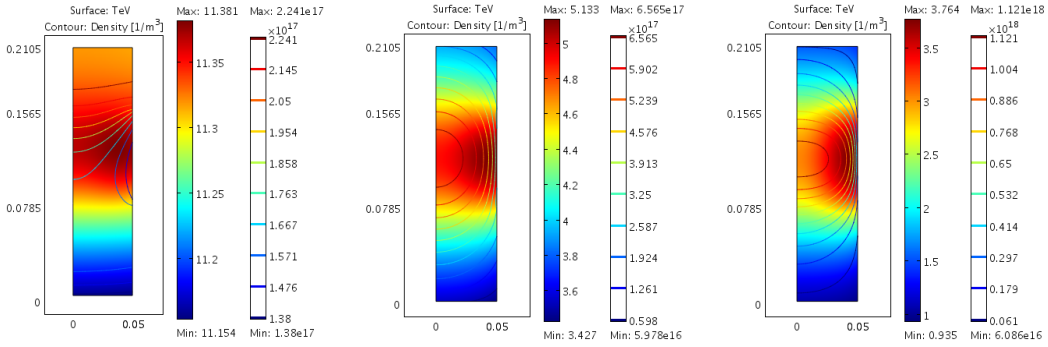

(a) $p_{\text{gas}} = 0.3\,\text{Pa}$. **(b)** $p_{\text{gas}} = 3\,\text{Pa}$. **(c)** $p_{\text{gas}} = 10\,\text{Pa}$.

Figure 4.14: T_e and n_e profiles for a $H_2^+ - e$ plasma in a H_2 gas at different pressures.

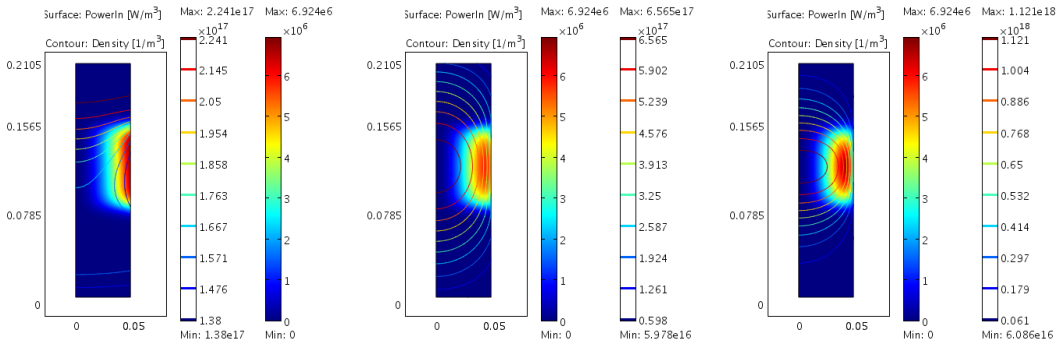

(a) $p_{\text{gas}} = 0.3\,\text{Pa}$. **(b)** $p_{\text{gas}} = 3\,\text{Pa}$. **(c)** $p_{\text{gas}} = 10\,\text{Pa}$.

Figure 4.15: p_{abs} and n_e profiles for a $H_2^+ - e$ plasma in a H_2 gas at different pressures.

In Figure 4.16 and 4.17 the maximum, minimum and mean electron density and temperature dependencies on the gas pressure are shown together with the mean values obtained without considering the magnetic confinement. In addition to the steepening in the profiles with pressure, one can note the following trends for the mean quantities:

- T_e decreases with increasing pressure to guarantee the particle conservation in the

continuity equation, in which $\nu_{\mathrm{iz}} \propto p_{\mathrm{gas}}\, T_{\mathrm{e}}^{A} \exp(-B/T_{\mathrm{e}})$ (the ionization frequency depends linearly on the gas pressure and with the Arrhenius' equation on the electron temperature). This trend well agrees with other numerical simulations for a hydrogen discharge [31], which take into account the Debye sheath and all the ionic (H^+, H_2^+, H_3^+, H^-) and neutral H and H_2 species. As previously said at lower pressures the magnetic confinement is more effective, which results in electron temperatures lower than those obtained for a plasma not confined by magnetic multipoles;

- n_{e} increases with increasing pressure but reaches a limiting value at high pressures (about $4 \cdot 10^{17}\,\mathrm{m}^{-3}$) because of the high localization of the electron density under the coil; without magnetic confinement the electron density would be lower.

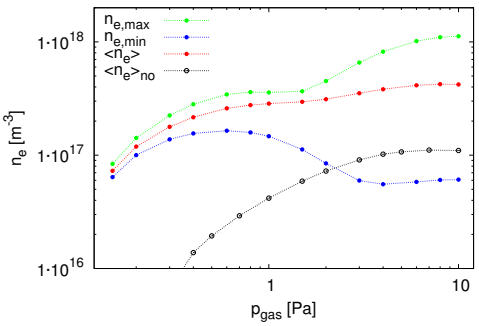

Figure 4.16: Electron density dependence on gas pressure in H_2; $\langle n_{\mathrm{e}} \rangle_{no}$ is the mean electron density obtained when the magnetic confinement is not considered.

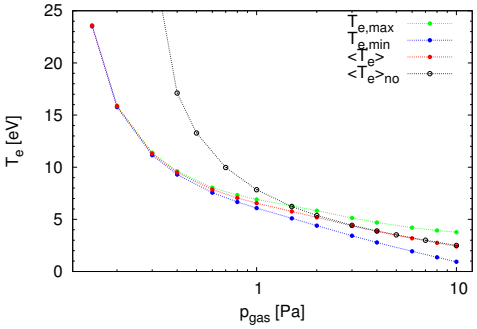

Figure 4.17: T_{e} dependence on gas pressure in H_2; $\langle T_{\mathrm{e}} \rangle_{no}$ is the mean electron density obtained when the magnetic confinement is not considered.

The electron temperature and the positive ion density in a hydrogen discharge have been measured in the inductively coupled plasma of the IPP prototype source (a negative ion source larger than NIO1) with Langmuir probes at 0.6 Pa and an injected RF power of 40 kW [35]: at the exit of the driver these measurements display a positive ion density (which can be assumed approximately equal to the electron density) of about $5 \cdot 10^{17}\,\mathrm{m}^{-3}$ and electron temperatures around 5 eV in the presence of magnetic confinement; when no magnetic field is present, the density decreases to about $3 \cdot 10^{17}\,\mathrm{m}^{-3}$ and the temperature increases to a value around 7 eV. The results obtained from the model proposed in this section for a hydrogen discharge well agree with the value of the plasma parameters in the IPP prototype source, showing that this model, even though simplified, can reproduce not only the trends of the electron temperature and density, but also their approximate values.

4.6 Plasma parameters in air discharge

Since the first experimental campaign of NIO1 has been done in air, in this section the model described in Section 4.2 will be used to simulate discharges in two molecular gases separately, nitrogen (78% dry air volume) and oxygen (21% dry air volume). For both gases the model in Section 4.2 is applied in the cases of low pressure regime and multipole confinement; in order to make the convergence process easier, the power density profile is not the one obtained from the Ohm's law, but is assumed a priori and takes the form in (4.38). The ion-neutral cross sections used are those in Table 4.1, the reaction rates and energy loss per electron-ion pair created are listed in Appendix A.2.

Since in Section 4.5.1 it was shown that in the model used the electron density increases linearly with applied power whereas the temperature profile does not change, the simulations for these two gases have been done at fixed $P_{\text{abs}} = 100\,\text{W}$ and $T_{\text{gas}} = T_{\text{ion}} = 400\,\text{K}$, while the gas pressure p_{gas} was ranging from 0.1 Pa to 10 Pa.

4.6.1 Nitrogen gas model

In the nitrogen gas case the ionic species considered is N_2^+, which has a mass $m_{\text{ion}} \simeq 28{\cdot}1.67 \cdot 10^{-27}\,\text{kg}$. The electron temperature and density profiles obtained at three different pressures are those in Figure 4.18; in Figure 4.19 and 4.20 the maximum, minimum and mean electron density and temperature dependencies on the gas pressure are shown together with the mean values obtained without considering the magnetic confinement. As can be seen, with respect to the hydrogen case:

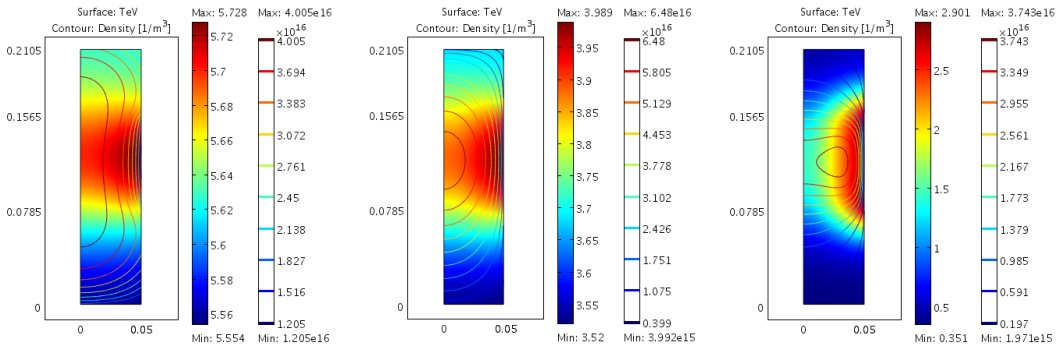

(a) $p_{\text{gas}} = 0.3\,\text{Pa}$. **(b)** $p_{\text{gas}} = 1\,\text{Pa}$. **(c)** $p_{\text{gas}} = 8\,\text{Pa}$.

Figure 4.18: T_e and n_e profiles for a $N_2^+ - e$ plasma in a N_2 gas at different pressures.

- the magnetic confinement is weaker, so the difference between the profiles obtained in the presence or in the absence of magnetic multipoles becomes important only at really low pressures;
- T_e has a slower decrease with pressure. For example, at $p_{\text{gas}} = 1\,\text{Pa}$ the maximum T_e (corresponding to regions where plasma is produced) is about 4.0 eV and at $p_{\text{gas}} = 5\,\text{Pa}$ is about 3.0 eV;

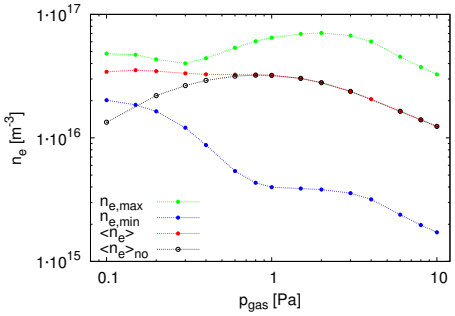

Figure 4.19: Electron density dependence on gas pressure in N_2; $\langle n_e \rangle_{no}$ is the mean electron density obtained when the magnetic confinement is not considered.

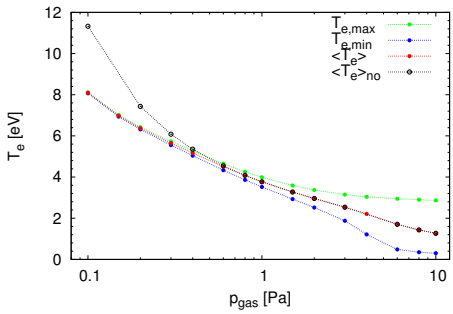

Figure 4.20: T_e dependence on gas pressure in N_2; $\langle T_e \rangle_{no}$ is the mean electron density obtained when the magnetic confinement is not considered.

- the mean electron density is approximately constant (about $3 \cdot 10^{16}\,\mathrm{m}^{-3}$) for pressures lower than 1 Pa whereas for higher pressures it decreases with increasing p_{gas}.

4.6.2 Oxygen gas model

In the oxygen gas case the ionic species considered is O_2^+, which has a mass $m_{\mathrm{ion}} \simeq 32{\cdot}1.67 \cdot 10^{-27}\,\mathrm{kg}$. The electron temperature and density profiles obtained at three different pressures are those in Figure 4.21; the maximum, minimum and mean electron density and temperature dependencies on the gas pressure are shown respectively in Figure 4.22 and 4.23. As can be seen, with respect to the nitrogen case:

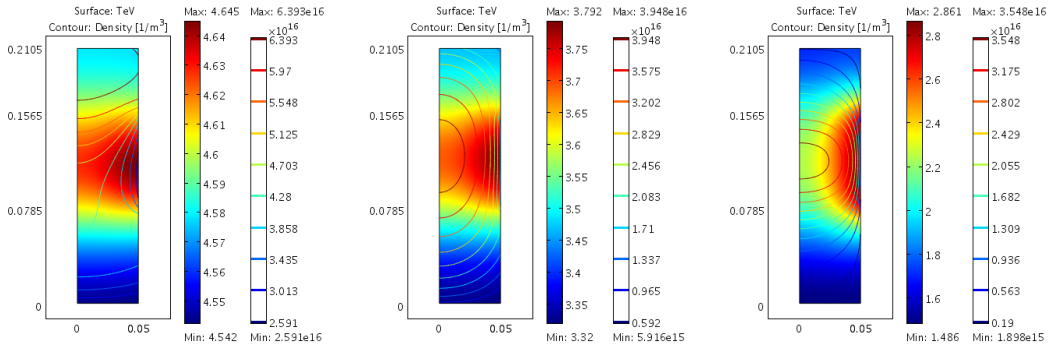

(a) $p_{\mathrm{gas}} = 0.3\,\mathrm{Pa}$. **(b)** $p_{\mathrm{gas}} = 1\,\mathrm{Pa}$. **(c)** $p_{\mathrm{gas}} = 8\,\mathrm{Pa}$.

Figure 4.21: T_e and n_e profiles for a $O_2^+ - e$ plasma in a O_2 gas at different pressures.

- the magnetic confinement is more effective;
- at $p_{\mathrm{gas}} = 1\,\mathrm{Pa}$ and 5 Pa the maximum electron temperatures are approximately equal (respectively about 3.8 eV and 2.9 eV), but T_e has a slower decrease with

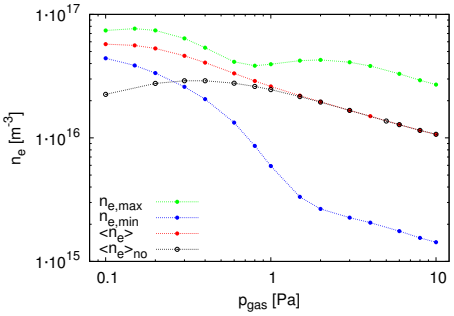

Figure 4.22: Electron density dependence on gas pressure in O_2; $\langle n_e \rangle_{no}$ is the mean electron density obtained when the magnetic confinement is not considered.

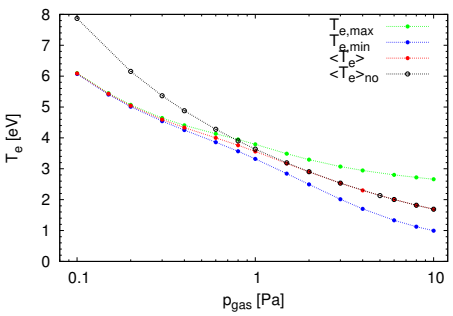

Figure 4.23: T_e dependence on gas pressure in O_2; $\langle T_e \rangle_{no}$ is the mean electron density obtained when the magnetic confinement is not considered.

pressure for low pressure values;

- the mean electron density is approximately constant (about $6 \cdot 10^{16}\,\mathrm{m}^{-3}$) for pressures lower than 0.2 Pa; for higher pressures the decrease with p_{gas} is faster than in the nitrogen case.

4.6.3 Comparison with experimental results

In plasma physics and ion source development, very elaborate theoretical calculation and expensive experimental equipment are necessary in order to obtain a good agreement between calculation and observation. As explained in Section 2.2, gas pressure was stabilized and measured before discharge operation, to minimize self pumping effects and avoid interference between the RF coil and source operation; during the first ever NIO1 experimental session two main quantities involving the plasma parameters have been measured: the plasma light (measured with a photomultiplier) and the plasma spectrum, measured by two spectrometers.

Measurement of plasma temperature by simple optical means [36] is sensitive only to high energy tails of the distribution, whose overall shape (Maxwellian, double Maxwellian or Druyvesteyn) is actually a postulate of the optical analysis. Similarly the expression of the rate coefficients in the fluid model here presented was finalized to a Maxwellian distribution.

The electron temperature estimated from the spectroscopic analysis shows that the model used, which assumes a Maxwellian distribution function, is not adequate for the specific experimental conditions: congruence of future optical observations and the present fluid model calculation of electron temperature is therefore a promising field of investigation. However, calculation of the electron energy distribution will require a kinetic model for the electron phase space distribution with a realistic coil and magnet, well beyond this thesis scope, and well beyond the available simulation resources.

A preliminary plot of the plasma luminosity as a function of the RF power was given

in Figure 2.13(a), in particular above 100 W the plasma luminosity depends linearly on the RF power as shown in Figure 2.13(b). As previously said in Section 4.5.1, in the model proposed in this section the electron temperature does not change with the injected power at fixed pressure, so if this assumption holds also in the experimental measurements, the PMT signal depends only on the electron density, in particular a linear dependence between the plasma light and the electron density can be assumed. The linear trend for a RF power above 100 W then well agrees with Figure 4.13, where the electron density depends linearly on the RF power.

CHAPTER 5

Numerical study on a magnetic filter field effect

In negative ion sources one of the main problems is to increase the negative ion production in the source in order to have a high extracted H^- current. In a hydrogen plasma there are two mechanisms which contribute to the negative ion H^- production (see Section 1.3 for a more detailed description): the first is the volume production mechanism, in which negative hydrogen ions are produced by dissociative attachment of low-energy electrons to vibrationally excited hydrogen molecules; the second is a surface production mechanism, in which fast atoms (H^0) or ions (H^+) are converted to H^- ions when colliding on the source walls. The latter mechanism can be enhanced with the injection of Caesium vapor near the plasma grid, where it forms a thin layer, thus lowering the work function of the PG itself.

In NIO1 a Cs input flange is located in the plasma grid assembly, but the Cs oven is not yet installed, so during the first beam operations only the first mechanism will lead to H^- production: in this process the cross section for H_2 vibrational excitation is larger for highly excited states ($\nu \geq 7$) and high electron energies, on the other hand the negative ions produced by dissociative attachment are easily destroyed by collisions with electrons with energies greater than 2 eV. A transverse magnetic field parallel to the plasma grid, called magnetic filter, is thus necessary: while the fast and less collisional (see Figure 3.1) electrons produced in the driver region are trapped by the magnetic filter field and driven towards the source walls, cold electrons diffuse through the filter because of their higher collisionality. In this way the electron temperature near the plasma grid is low enough to produce negative ions through collisions with the vibrationally excited molecules diffusing across the magnetic field and to prevent their destruction.

The main aim of this chapter is to model the magnetic filter field in NIO1, in particular to study the decrease in the electron temperature when approaching the plasma grid. A description of the magnetic filter field in NIO1 is given in Section 5.1, then in Section 5.2 a detailed explanation of the algorithm used to simulate the electron trajectories is given. Finally the results obtained are presented in Section 5.3.

5.1 Magnetic filter field profile in NIO1

The magnetic field acting as a filter in NIO1 is produced by:

- the front multipole assemblies;
- the current I_y which flows along the y direction in the plasma grid and closes its path in the bias plate;

by taking z as the direction along the axis of the chamber and y the direction of I_y, the magnetic filter is oriented along the x direction. A numerical simulation which uses $I_y = 500\,\mathrm{A}$ yields the results in Figure 5.1 (continuous line) for the x component of the magnetic field on axis [cit. simulaz Cavenago]; the magnetic field $B_x(z)$ used in this numerical study has the gaussian profile in Figure 5.1 (dashed line).

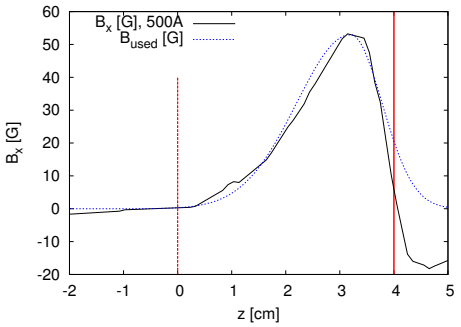

Figure 5.1: Magnetic filter field on axis in NIO1 obtained from numerical simulations (continuous line) and value used in the present algorithm (dashed line); the vertical line at $z = 4\,\mathrm{cm}$ corresponds to the PG.

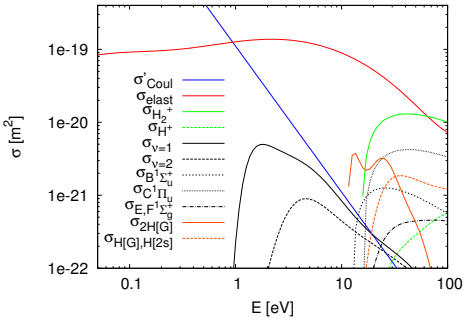

Figure 5.2: Cross sections for electron collisions with hydrogen molecules and H_2^+ [19]; σ_{elast}, $\sigma_{H_2^+}$ and $\sigma_{Coul} = 10^3\sigma'_{Coul}$ are the ones considered in this code.

The coordinate system chosen is centered on the chamber axis 4 cm before the plasma grid, a position in which the magnetic field on axis is negligible, with the positive z direction pointing towards the PG.

5.2 Algorithm description

The electron trajectories are calculated by a code written in C++ which uses a Monte Carlo method [37] in a way similar to what has been done in [38].

In the region where the magnetic field is negligible, a Maxwell-Boltzmann energy distribution is assumed for the electrons:

$$F(E,T) = \frac{2}{\sqrt{\pi}} \frac{\sqrt{E}}{k_B T^{3/2}} \exp\left(-\frac{E}{k_B T}\right) \tag{5.1}$$

$F(E,T)$ reaches its maximum for $E_{max} = k_B T/2$:

$$F(T)_{max} = F(E_{max},T) = \sqrt{\frac{2}{\pi}}\, e^{-\frac{1}{2}}\, \frac{1}{k_B\, T} \tag{5.2}$$

The electron temperature T is given as an external parameter and the particles are created at position (x,y,z)=(0,0,0) with an energy that follows the Maxwell-Boltzmann energy distribution with a with a cutoff for $E > 5T$. The energy is assigned to the electrons using the "acceptance-rejection" method [39], that is, chosen two random numbers $\varepsilon \in [0,5T]$ and $u \in [0,1]$, if $uF(T)_{max} < F(\varepsilon,T)$ then ε is accepted as the starting energy, otherwise it is rejected. Then, if the initial energy is $E_0 = \varepsilon$, the initial velocity has modulus $v_0 = \sqrt{2\, e\, E_0/m_e}$ and is given an isotropic distribution in the positive z direction by generating two random numbers $u \in [0,1]$ and $t \in [0,1]$ and calculating the azimuthal angle ϕ and the polar angle θ as:

$$\phi = 2\pi u \tag{5.3a}$$

$$\theta = \arccos(t) \tag{5.3b}$$

The electron starting velocity components are then:

$$\begin{cases} v_{0,x} = v_0\, \cos(\phi)\, \sin(\theta) \\ v_{0,y} = v_0\, \sin(\phi)\, \sin(\theta) \\ v_{0,z} = v_0\, \cos(\theta) \end{cases} \tag{5.4}$$

The particle velocity is then integrated using the Boris algorithm (its implementation is described in Section 5.2.1) and the time step is adapted in order to have at least 20 steps for each period of rotation around the magnetic axis:

$$dt = \frac{T_{min}}{20} = \frac{2\pi}{20}\frac{m_e}{e\, B_{max}} = 3.37 \cdot 10^{-10}\,\mathrm{s} \tag{5.5}$$

where $B_{max} = 5.3\,\mathrm{mT}$ (see Figure 5.1). At each time step the electron can undergo a collision with the ions H_2^+ or the neutral H_2 particles, which are considered uniformly distributed in space; the gas density used in this simulation is $n_{gas} = 1.8 \cdot 10^{20}\,\mathrm{m}^{-3}$ (which corresponds to $p_{gas} = 1\,\mathrm{Pa}$ and $T_{gas} = 400\,\mathrm{K}$) and the positive ion density is $n_{ion} = 1 \cdot 10^{17}\,\mathrm{m}^{-3}$. The scattering processes considered are the following ones (for the corresponding cross sections see Figure 5.2):

- $e - H_2$ *elastic collisions*: the mean free path associated with it is $\lambda_{el} = (n_{gas}\sigma_{el})^{-1}$;
- $e - H_2^+$ *coulomb collisions*: the mean free path associated with it is $\lambda_{coul} = (n_{ion}\sigma_{coul})^{-1}$;
- $e - H_2$ *ionization collisions*: the mean free path associated with it is $\lambda_{ion} = (n_{gas}\sigma_{ion})^{-1}$.

The total collision probability P_{coll} is then

$$P_{coll} = 1 - e^{-\frac{d}{\lambda}} \tag{5.6}$$

where d is the distance travelled by the particle since the last collision and λ is the total mean free path, which in this case is

$$\lambda = \left(n_{gas}(\sigma_{el} + \sigma_{ion}) + n_{ion}\sigma_{coul}\right)^{-1} \tag{5.7}$$

To decide whether the electron undergoes a collision or not, at each time step a random number $u \in [0,1]$ is generated:

- if $u > P_{coll}$ than the electron does not collide, so the Boris algorithm is applied to the position and velocity calculated in the preceding step;
- if $u < P_{coll}$ than the electron has collided, so the Boris algorithm is applied to the particle position calculated in the preceding step and to the particle velocity after the scattering. The scattering angle probability and the electron energy after the collision depend on the collision type, which is determined in the following way:
  - if $u < P_{coll}\,\lambda\, n_{gas}\sigma_{el}$ the electron undergoes an elastic scattering;
  - if $P_{coll}\,\lambda\, n_{gas}\sigma_{el} < u < P_{coll}\,\lambda\,(n_{gas}\sigma_{el} + n_{ion}\sigma_{coul})$ the electron undergoes a coulomb scattering;
  - otherwise the electron undergoes an ionization scattering.

  The algorithm used to determine the scattering angles, the velocity after the collision and the energy loss for each one of these processes is given in Section 5.2.2.

The iterative process used to integrate the particle trajectory stops and a new electron is created when one of the following conditions is satisfied:

- $z > 4\,\text{cm}$: the electron has reached the plasma grid;
- $r > 5\,\text{cm}$: the electron has reached the chamber wall;
- $z < -8\,\text{cm}$: the electron has trepassed a limit back position, beyond which its trajectory is no longer followed;
- $N > N_{limit}$: the number of iterations exceeds a fixed (high) limit.

The energy domain, which ranges from $0\,\text{eV}$ to $5T$, is divided in N_E bins: the electron energy is sampled into steps $\Delta E = 5T/N_E$. As for the spatial dependence, we can assume the uniformity of the magnetic field with respect to the radial position of the particles, so that a 1D model is sufficient to describe the electron cooling induced by the magnetic field. Therefore, only the z domain between the electron starting point ($z = 0\,\text{cm}$) and the plasma grid position ($z = 4\,\text{cm}$) is sampled, in particular it is divided in N_Z bins: the steps in the z direction are then $\Delta z = 4\,\text{cm}/N_Z$. In this way a $N_E \times N_Z$ matrix M can

be defined, where the element M_{ij} corresponds to energies $(i\,\Delta E) \leq E < ((i+1)\,\Delta E)$ (with $i \in [0,N_E-1]$) and z-positions $(j\,\Delta z) \leq z < ((j+1)\,\Delta z)$ (with $j \in [0,N_Z-1]$). At each time step the particle z-position and energy are evaluated and the counter of the corresponding M_{ij} is increased by one unity: the output of the program is the $N_E \times N_Z$ matrix obtained after the integration of the trajectories of all the electrons that can be used to evaluate the electron energy distribution function at each z position.

5.2.1 Boris algorithm implementation

The particle trajectories in electric and magnetic fields are calculated by integration of the particle velocity using the Boris integration scheme [40]; the algorithm is described in details in Appendix B.1.

In order to verify the correct implementation of the Boris scheme in this program, the trajectory described by an electron in a magnetic field can be studied using the Hamiltonian formalism. The Hamiltonian of a charged particle in magnetic and electric fields is [41]:

$$\mathcal{H} = \frac{1}{2m}\left(\mathbf{p} - q\mathbf{A}(\mathbf{x},t)\right)^2 + q\phi(\mathbf{x},t) \tag{5.8}$$

where $\mathbf{p} = m\mathbf{v} + q\mathbf{A}$ is the conjugate variable with respect to position and $\mathbf{A}$ is the vector potential. The equations of motion are:

$$\begin{aligned} \dot{x}_i &= \frac{\partial \mathcal{H}}{\partial p_i} \\ \dot{p}_i &= -\frac{\partial \mathcal{H}}{\partial x_i} \end{aligned} \tag{5.9}$$

When considering a constant magnetic field along the $\hat{x}$ direction $B_x(z)$ which depends only on the z coordinate, the vector potential can be written as:

$$A_y(z) = -\int_0^z B_x(z)\,dz \tag{5.10}$$

so the Hamiltonian becomes

$$\mathcal{H} = \frac{1}{2m}\left(p_x^2 + p_z^2 + \left(p_y + q\int_0^z B_x(z)\,dz\right)^2\right) \tag{5.11}$$

In the particular case of a uniform magnetic field B_0 then $A_y = -B_0 z$ and the Hamiltonian is reduced to the Hamiltonian of a harmonic oscillator

$$\mathcal{H} = \frac{1}{2m}\left(p_x^2 + p_z^2 + (p_y + qB_0 z)^2\right) \tag{5.12}$$

By taking as initial conditions

$$\begin{cases} x_0 = y_0 = z_0 = v_{x,0} = v_{y,0} = 0 \\ v_{z,0} = v_0 \end{cases} \tag{5.13}$$

the equations of motion in (5.9) yield as solution

$$\begin{cases} x = 0 \\ y = \frac{v_0 m}{qB}\left(1 - \cos\left(\frac{qB}{m}t\right)\right) = r_L\left(\cos(\omega t) - 1\right) \\ z = \frac{v_0 m}{qB}\sin\left(\frac{qB}{m}t\right) = r_L \sin(\omega t) \end{cases} \tag{5.14}$$

where ω and r_L are respectively the cyclotron frequency and the Larmor radius. For a 1 eV electron and $B_0 = 5.3\,\mathrm{mT}$, then $\omega = 9.32 \cdot 10^8\,\mathrm{rad}$ and $r_L = 0.64\,\mathrm{mm}$, which gives the dashed trajectory in Figure 5.3(a). In the same figure the solution calculated by the program is plotted in red (500 time steps): as can be seen the two are in good agreement even at the time step chosen ($T/20$) and the energy is conserved during the electron motion.

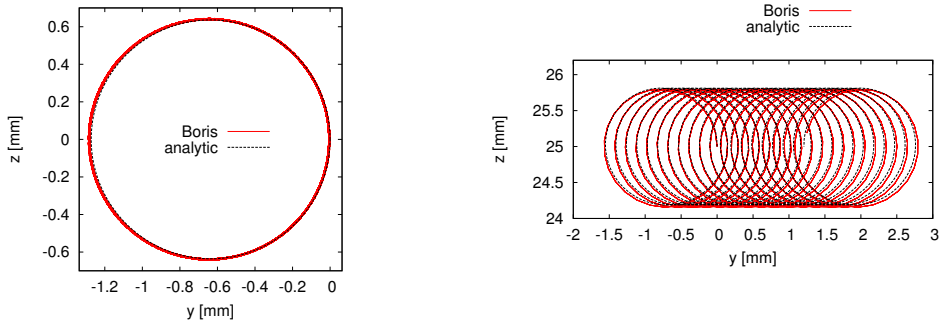

(a) Uniform $B_x(z) = B_0 = 5.3\,\mathrm{mT}$, $(y_0, z_0) = (0, 0)$: in black the exact solution obtained from the Hamiltonian formalism.

(b) Magnetic filter field $B_x(z)$ in Figure 5.1, $(y_0, z_0) = (0, 25)$: in black the solution obtained using the guiding center theory.

Figure 5.3: Electron trajectories in the (y,z) plane, starting point on the axis of the chamber: the solution obtained from the program is plotted in red.

In the case of an arbitrary dependence of the magnetic field, the Hamilton's equations no longer yield an analytical solution in closed form, so some approximations have to be made in order to study the particle motion. If the scale of the magnetic field inhomogeneities is larger than the Larmor radius, then the electron motion can be broken up into a circular motion around a central point called the guiding center and the motion of the guiding center itself [30]: in the guiding center theory only the second motion is studied, while the gyration motion is that due to the magnetic field evaluated in the guiding center. It can be shown that in the presence of a magnetic field gradient,

the guiding center drifts with a velocity given by:

$$v_{\nabla B} = \pm\frac{1}{2} v_0 r_L \frac{\mathbf{B}\times\nabla B}{B^2} \tag{5.15}$$

where the $\pm$ signs depend on whether the particle has a positive or negative charge. A comparison between the results obtained from the implementation of the Boris algorithm and from the guiding center theory is given in Figure 5.3(b), where the magnetic field used is the one in Figure 5.1 evaluated at the starting point $z = 2.5\,\text{cm}$: the guiding center motion is correctly reproduced but there are discrepancies between the two trajectories; this is due to the fact that during one gyration the magnetic field is not uniform so the Larmor radius is not constant during the circular motion.

Since the results obtained from the program are in agreement with the theory, the implementation of the Boris algorithm can be considered correct.

5.2.2 Electron collisions with ions and neutrals

When considering a collision, the scattering angles (ϕ, θ) are referred to the velocity direction before the scattering in the center of mass (CM) frame reference; since $m_{H_2}, m_{H_2^+} \gg m_e$, the CM system is approximately equal to the laboratory system, so to make the simulation faster the two are taken as coincident. By calling $\hat{v}_{inc}$ the unit vector parallel to the incident velocity, a new cartesian frame of reference can be defined, with $\hat{z}' = \hat{v}_{inc}$ and $\hat{y}'$ perpendicular to the plane containing $\hat{z}$ and $\hat{z}'$ (see Figure 5.4):

$$\hat{z}' = \begin{pmatrix} \sin\theta_0\cos\phi_0 \\ \sin\theta_0\sin\phi_0 \\ \cos\theta_0 \end{pmatrix}, \quad \hat{y}' = \frac{\hat{z}\times\hat{z}'}{|\hat{z}\times\hat{z}'|} = \begin{pmatrix} -\sin\phi_0 \\ \cos\phi_0 \\ 0 \end{pmatrix}, \quad \hat{x}' = \frac{\hat{y}'\times\hat{z}'}{|\hat{y}'\times\hat{z}'|} = \begin{pmatrix} \cos\theta_0\cos\phi_0 \\ \cos\theta_0\sin\phi_0 \\ -\sin\theta_0 \end{pmatrix}$$

The components of the unit vector parallel to the scattered velocity $\hat{v}_{scat}$ are calculated

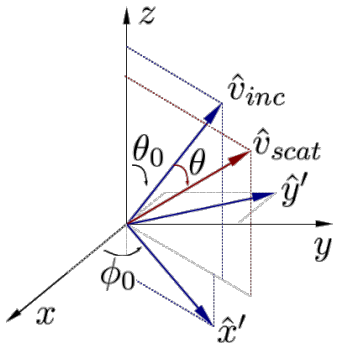

Figure 5.4: Coordinate system.

in this new frame of reference using Equation (5.4) (with $v_0 = 1$) and are then projected

on the original frame of reference (x, y, z) by:

$$\hat{v}_{scat} = \begin{pmatrix} \cos\theta_0 \cos\phi_0 & -\sin\phi_0 & \sin\theta_0 \cos\phi_0 \\ \cos\theta_0 \sin\phi_0 & \cos\phi_0 & \sin\theta_0 \sin\phi_0 \\ -\sin\theta_0 & 0 & \cos\theta_0 \end{pmatrix} \begin{pmatrix} \cos\phi \sin\theta \\ \sin\phi \sin\theta \\ \cos\theta \end{pmatrix} \tag{5.16}$$

Upon knowing the initial velocity direction and the scattering angles (θ, ϕ) with respect to this direction, the final velocity direction is computed according to (5.16).

The probability distribution along the azimuthal angle ϕ is uniform over the interval $[0,2\pi]$, so, given a random number $u \in [0,1]$, it is determined by:

$$\phi = 2\pi u \tag{5.17}$$

The distribution of the polar scattering angle θ instead depends on the collision type.

Elastic collisions

For an electron-neutral elastic collision, given a random number $u \in [0,1]$, the polar scattering angle θ can be calculated as follows [37]:

$$\theta = \arccos\left(\frac{2 + E - 2(1+E)^u}{E}\right) \tag{5.18}$$

where E is the electron energy in electronvolts. At high electron energies this gives mostly small scattering angles whereas at low energies the scattering is more isotropic.

The electron energy loss in an elastic scattering event with a particle having mass M is [10]

$$\Delta E = E\frac{2m_e M}{(m_e + M)^2}(1 - \cos\theta) \tag{5.19}$$

so the velocity after the collision is calculated as

$$v_{scat} = v_{inc}\sqrt{1 - \frac{2m_e M}{(m_e + M)^2}(1 - \cos\theta)} \tag{5.20}$$

where in this case M is the neutral hydrogen mass.

Coulomb collisions

The distribution of the polar angle for a Coulomb collision is calculated using the cumulative small-angle method [42]:

$$\theta = \arccos\left(1 + s\ln u\right) \tag{5.21}$$

with u a random number $u \in [0,1]$ and s

$$s = n_{ion} \sqrt{\frac{2}{m_e}}\, \pi \left(\frac{e^2}{4\pi\varepsilon_0}\right)^2 \frac{1}{E^{3/2}}\, \ln \Lambda \, dt \tag{5.22}$$

where $\ln \Lambda$ is the Coulomb logarithm:

$$\ln \Lambda = \ln \left[\left(\frac{\varepsilon_0 \, k_B \, T}{n \, e^2}\right)^{1/2} \left(\frac{e^2}{4\pi\varepsilon_0} \frac{m_e + m_{H_2^+}}{2\, m_{H_2^+}} \frac{1}{E}\right)^{-1} \right] \tag{5.23}$$

and dt is the time step in (5.5) used in the simulation.

Since the Coulomb scattering is an elastic process, the energy loss and the final velocity are calculated as in (5.19) and (5.20), where in this case M is the positive hydrogen ion mass.

Ionizing collisions

If an ionization occours, a new electron is created at the collision position: the scattering angles for the two electrons are calculated using (5.17) and (5.18). As of the energy, the molecular hydrogen ionization energy is $E_{ion} = 15.4\,\text{eV}$, so by calling E_{inc} the energy of the primary electron before the collision, the scattered and the ejected electrons have energies that satisfy:

$$E_{scat} + E_{eject} = E_{inc} - E_{ion} \tag{5.24}$$

In [43] it is shown that, given a random number $u \in [0,1]$, the energy of the ejected electron can be written as

$$E_{eject} = B(E_{inc}) \tan \left(u \arctan \left(\frac{E_{inc} - E_{ion}}{2B(E_{inc})} \right) \right) \tag{5.25}$$

where $B(E_{inc})$ is a known function (for hydrogen, $B(E_{inc}) \simeq 8.3$). When E_{inc} is just above the threshold energy E_{ion}, this reduces to

$$E_{eject} = u \, \frac{E_{inc} - E_{ion}}{2} \tag{5.26}$$

so on average the remaining energy is divided equally between the two electrons:

$$\langle E_{eject} \rangle = \langle E_{scat} \rangle = \frac{E_{inc} - E_{ion}}{2} \tag{5.27}$$

In order to make the simulation faster, instead of using (5.25), the approximated expression in equation (5.27) is used.

5.2.3 Electron temperature and density evaluation

The electron temperature and density as a function of the position along the z axis can be evaluated once the electron energy probability function EEPF or the electron energy distribution function EEDF are known. For a pure Maxwellian distribution the EEPF $f(E,z)$ is [44]:

$$f(E,z) = \frac{2}{\sqrt{\pi}} \frac{n_e(z)}{(k_B T_e(z))^{3/2}} e^{-\frac{E}{k_B T_e(z)}} \tag{5.28}$$

By taking the logarithm one obtains:

$$\ln\left(f(E,z)\right) = \ln\left(\frac{2}{\sqrt{\pi}} \frac{n_e(z)}{(k_B T_e(z))^{3/2}}\right) - \frac{E}{k_B T_e(z)} \tag{5.29}$$

hence the electron temperature can be easily obtained from the slope of this curve.

The EEPF is related to the EEDF $F(E,z)$ as follows:

$$F(E,z) = \sqrt{E}\, f(E,z) \tag{5.30}$$

The electron density and temperature can then be calculated at different z positions by integrating the EEDF:

$$n_e(z) = \int_0^\infty F(E,z)\, dE = \int_0^\infty \sqrt{E}\, f(E,z)\, dE \tag{5.31a}$$

$$T_e(z) = \frac{2}{3} \frac{1}{n_e(z)} \int_0^\infty E\, F(E,z)\, dE = \frac{2}{3} \frac{1}{n_e(z)} \int_0^\infty E^{3/2}\, f(E,z)\, dE \tag{5.31b}$$

As previously said the output of the program is a $N_E \times N_Z$ matrix M: the j^{th} column of this matrix is proportional to the EEPF integrated over the x, y plane in the position $z_j = (j + 1/2)\Delta z$; this quantity will be called EEPF' and is measured in $\mathrm{eV}^{-3/2}/\mathrm{m}$. The electron temperatures and densities are then calculated using (5.31) in its discrete form:

$$n_e(z_j) \propto \sum_{i=0}^{N_E-1} \sqrt{E_i}\, M_{i,j} \tag{5.32a}$$

$$T_e(z_j) = \frac{2}{3} \frac{1}{n_e(z_j)} \sum_{i=0}^{N_E-1} E_i^{3/2}\, M_{i,j} \tag{5.32b}$$

where $E_i = (i + 1/2)\Delta E$.

5.3 Simulation results

In this section the results obtained by running the simulation are presented: in order to underline the importance of the different scattering processes in cooling the electrons, first only elastic collisions are considered, then the coulomb collisions are added and finally also ionization is taken into consideration. The electron temperature and density are calculated as in Section 5.2.3. The discretization is done as follows:

- $dt = T_{min}/20$, so, if $B_{max} = 5.3\,\mathrm{mT}$, $dt = 3.37 \cdot 10^{-10}\,\mathrm{s}$;
- $N_Z = 50$, so $\Delta z = 0.8\,\mathrm{mm}$;
- $N_E = 250$, so, for a starting electron distribution with $T_e = 10\,\mathrm{eV}$, $\Delta E = 0.2\,\mathrm{eV}$.

It will then be shown how an increase in the magnetic field affects the electron temperature and density across the magnetic filter.

5.3.1 Comparison between scattering contributions

The results obtained when considering elastic collisions only (black), when including Coulomb collisions (red) and when considering also ionizing collisions (blue) are plotted in Figure 5.5 and 5.6.

The EEPF' at two z positions, $z_1 = 2\,\mathrm{cm}$ and $z_2 = 3.52\,\mathrm{cm}$, are shown in Figure 5.5(a), where the main differences between the three approximations are at:

- low energies (below 5 eV): by adding the Coulomb contribution, the EEPF' at very low energies decreases with respect to the elastic case, whereas when the ionization contribution is added the EEPF' increases again due to the low energy electrons created in the ionizations;
- high energies (above the ionization threshold): the EEPF' changes considerably only when the ionizations are added, in particular, with increasing distance along z, this energy range is progressively depleted.

The mean temperatures obtained by EEPF' integration are shown in Figure 5.5(b): the temperature obtained considering only elastic collisions is lower than the one obtained by adding Coulomb collisions because of the high electron population at very low temperatures; after an initial electron cooling due to the loss of the more energetic electrons to the walls, both display an almost constant temperature which starts to slightly decrease at $z = 2.5\,\mathrm{cm}$, reaches a minimum where $B_x(z)$ is maximum and then increases again. When including also the ionization scattering the temperature is much lower because of the combined effects described when talking about the EEPF' (low energy electrons created in the ionizations and depletion of the high energy range): in this case the decrease in temperature is more pronounced and there is electron cooling in the whole region between the starting point and the maximum of the magnetic field.

The electron temperatures have been calculated also by ln(EEPF') interpolation in two energy ranges, which correspond to two Maxwellian distributions having different temperatures:

- 5 eV< E <15 eV. As can be seen in Figure 5.6(a), by including the ionizing collisions the temperature across z is reduced by 1 eV: since this is the dominant electron population, it is the cooling in this range that affects the mean electron temperature behaviour in Figure 5.5(b).
- E >20 eV. As can be seen in Figure 5.6(b), the starting temperature obtained from the interpolation is approximately the temperature of the initial Maxwellian distribution (10 eV): across the magnetic field it decreases substantially, in particular near the plasma grid it reaches 4 eV when including also the ionization scattering. In all the three approximations, the electron cooling is more effective between $z = 2.5$ cm and the maximum of the magnetic field.

It is worth noting that in both energy ranges, after the electron temperature reaches a minimum value where $B_x(z)$ is maximum, it remains constant in the region where the slope of the magnetic field is negative: this behaviour has been observed also in experimental measurements [45].

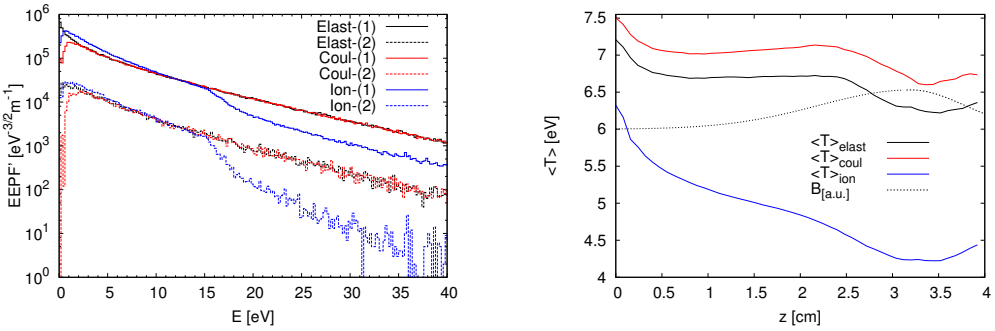

(a) EEPF' at the two z positions (1)=2 cm, (2)=3.52 cm.

(b) T_e obtained by EEPF' integration at all the z positions.

Figure 5.5: Comparison between the EEPF' and mean T_e obtained when considering elastic collisions only (black), when including Coulomb collisions (red) and when considering also ionizing collisions (blue).

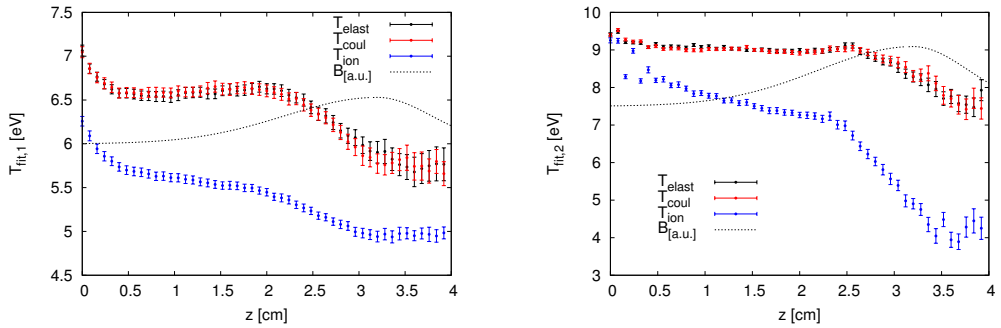

(a) 5 eV< E <15 eV. **(b)** Energy range: E >20 eV.

Figure 5.6: Comparison between T_e obtained interpolating the EEPF' at all the z positions in two energy ranges when considering elastic collisions only (black), when including Coulomb collisions (red) and when considering also ionizing collisions (blue).

5.3.2 Temperature and density dependence on magnetic field strength

In this paragraph the results obtained using magnetic fields with different intensities are shown; in the simulations all the collision processes described in the preceding sections are considered (elastic, Coulomb and ionization scattering). The electrons are created at $(x, y, z) = (0, 0, 0)$ with a starting Maxwellian distribution with $T = 10\,\text{eV}$ and pass through:

- no magnetic field $B = 0$ (in black): the electrons created at the starting point are $N_{start} = 2 \times 10^5$, the time step used is $dt = 3.37 \cdot 10^{-10}\,\text{s}$;
- the magnetic field $B_x(z)$ in Figure 5.1 (in red): the electrons created at the starting point are $N_{start} = 1.1 \times 10^6$, the time step used is $dt = 3.37 \cdot 10^{-10}\,\text{s}$;
- a magnetic field $2B_x(z)$ (in blue): the electrons created at the starting point are $N_{start} = 3.5 \times 10^5$, the time step used is $dt = 1.69 \cdot 10^{-10}\,\text{s}$.

As it can be seen in Figure 5.7(a), the EEPF' before the maximum of the magnetic field ($z_1 = 2\,\text{cm}$) is higher in the low energy region (below the ionization threshold) at higher B values because of the repelling effect of the magnetic field; above the ionization energy on the other hand EEPF' is lower for higher B values because the ionization processes are localized mainly near the starting position of the electrons. After the maximum of the magnetic field ($z_2 = 3.5\,\text{cm}$), the EEPF' in the presence of a magnetic filter field is lower than the one obtained by setting $B = 0$ (see Figure 5.7(b)) because of the electron confinement due to the magnetic filter, in particular the range above the ionization threshold is depleted because the ionization processes are localized mainly near the starting position of the electrons.

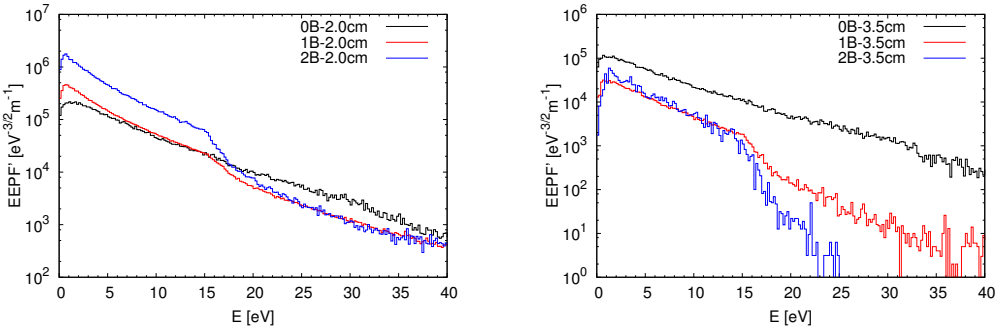

(a) EEPF' at $z = 2\,\text{cm}$. **(b)** EEPF' at $z = 3.52\,\text{cm}$.

Figure 5.7: Comparison between the EEPF's obtained without magnetic field (black), with $B_x(z)$ in Figure 5.1 (red) and $2B_x(z)$ (blue).

As already mentioned, there are two electron Maxwellian populations, the bigger one at low temperatures (which determines the mean electron temperature) and a smaller one at high temperature. Their temperature across z has been found by ln(EEPF') interpolation in the following energy ranges:

- $5\,\text{eV} < E < 15\,\text{eV}$. As can be seen in Figure 5.8(a), in this energy range without a magnetic field the temperature remains practically unchanged; by introducing a magnetic field the temperature is lowered and the cooling effect is stronger for higher B values (at $B = 2B_x(z)$, $T_{fit,1} \simeq 3\,\text{eV}$ in proximity of the PG).
- $E > 20\,\text{eV}$; as can be seen in Figure 5.8(b), the starting temperature obtained from the interpolation is approximately the temperature of the initial Maxwellian distribution (10 eV). Without the magnetic field the temperature slowly decreases across z because of inelastic collisions and energetic electron escape to the wall: when introducing the magnetic field, the electron temperature decreases substantially, in particular it drops at $z = 2.5\,\text{cm}$ for $B = B_x(z)$; for $B = 2B_x(z)$ the temperature starts to decrease at $z = 1.5\,\text{cm}$ and it reaches a minimum approximately where B is maximum ($T_{fit,2} \simeq 3\,\text{eV}$): beyond this point almost no electrons are present so the fit on ln(EEPF') is no longer meaningful.

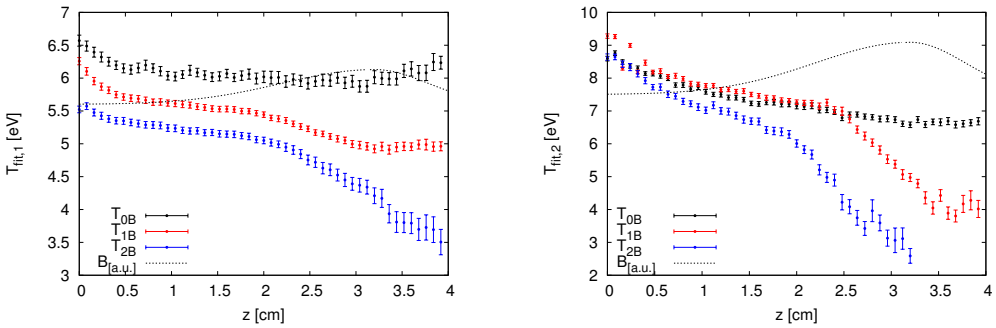

(a) 5 eV< E <15 eV. **(b)** Energy range: E >20 eV.

Figure 5.8: Comparison between T_e obtained interpolating the EEPF' at all the z positions in two energy ranges: T_{0B} (in black) corresponds to the values obtained without magnetic field, T_{1B} (in red) to T_e obtained with $B_x(z)$ in Figure 5.1 and T_{2B} (in blue) corresponds to T_e obtained with $2\,B_x(z)$.

In Figure 5.9 the mean temperatures obtained by EEPF' integration are shown, where the magnetic filter field effect in electron cooling is clear.

The electron densities in Figure 5.10 are calculated as in (5.32a) and are normalized in order to have an electron density $n_e = 1 \cdot 10^{17}\,\mathrm{m}^{-3}$ at the starting point: as can be seen there is an increased electron confinement with a stronger magnetic field. This results in a density decrease by more than one order of magnitude, in particular at the plasma grid the density is reduced by a factor 0.02 for $B_{max} = 5.3\,\mathrm{mT}$ and by a factor 0.005 for $B_{max} = 10.6\,\mathrm{mT}$. These values however have been obtained by neglecting the presence of the electric field that forms at the plasma edges, which indeed plays a crucial role at the PG. This field acts in a region whose depth can be evaluated as $10\lambda_D$ thick, where λ_D is the Debye length:

$$\lambda_D = \sqrt{\frac{\varepsilon_0\, k_B\, T_e}{n_e\, e^2}} \tag{5.33}$$

By taking $n_e = 1 \cdot 10^{17}\,\mathrm{m}^{-3}$ as the starting density, which is approximately the electron density in proximity of the plasma grid obtained from the numerical simulation in Chapter 4 (see Figure 4.11(a)), one has the values in Table 5.1: for both magnetic fields at the sheath edge the density is about 1/20 its initial value; beyond the edge one should include the sheath potential and the density would have a different profile.

Table 5.1: Sheath thickness for different magnetic fields.

B_{max}	n_{PG}	T_{PG}	d_{sheath}	n_{sheath}
0.0 mT	$1.75 \cdot 10^{16}\,\mathrm{m}^{-3}$	6.5 eV	1.4 mm	$1.85 \cdot 10^{16}\,\mathrm{m}^{-3}$
5.3 mT	$1.77 \cdot 10^{15}\,\mathrm{m}^{-3}$	4.5 eV	3.7 mm	$4.1 \cdot 10^{15}\,\mathrm{m}^{-3}$
10.6 mT	$5.0 \cdot 10^{14}\,\mathrm{m}^{-3}$	3.5 eV	6.2 mm	$4.1 \cdot 10^{15}\,\mathrm{m}^{-3}$

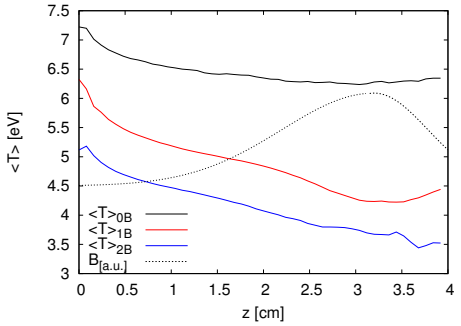

Figure 5.9: Electron temperature calculated as in (5.32b).

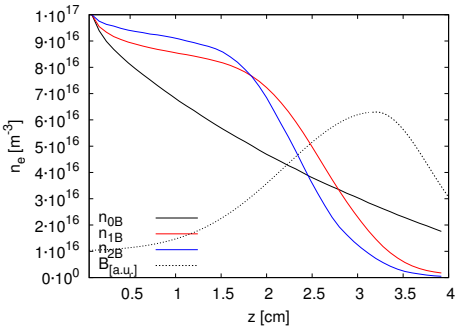

Figure 5.10: Electron density calculated as in (5.32a).

CHAPTER 6

Beam acceleration

The main aim of this chapter is to model the extraction and acceleration of negative ions: in Section 6.1 a description of the ion extraction mechanism regulated by space-charge effects and of the main parameters used to describe the quality of a negative ion beam is given, together with the main problems connected with the use of negative ion sources.

The NIO1 grid and permanent magnet system in the acceleration column is described in Section 6.2, where the nominal operation values have been set for an extracted H^- current density $j_{H^-} \simeq 300\,\mathrm{A\,m^{-2}}$.

Since in the first NIO1 operations the beam will be extracted from an air plasma or from a hydrogen plasma in which the H^- ions are produced only via volume mechanisms, the simulations described in Section 6.3 have been performed postulating an extracted current density lower than the nominal value, namely $j_{H^-} = j_{O^-} = 30\,\mathrm{A\,m^{-2}}$. The tools used in the beam simulation are the SLACCAD code, used to obtain the potential map between the grids, and the EAMCC code, which gives the particle trajectories by taking into account the electric potential and the magnetic fields in the simulation region. It will be shown that appropriate adjustments on the grid voltages and on the strength of the magnetic fields have to be done, in particular when using an hydrogen beam at the low current density considered.

6.1 Negative ion extraction and acceleration

In negative ion sources the negative ions produced in the source volume or on the PG rear wall are extracted through the plasma grid apertures (held at the source voltage) by an extraction electrode held at a higher potential, the extraction grid EG. In this way the extracted beam current is space-charge limited and the extractable emission current density can be calculated by the Child-Langmuir law ([46], [47]), which is valid in the case of a planar and infinite emission area and of ions having zero initial energy in the longitudinal direction:

$$j_{CL} = \frac{4}{9}\varepsilon_0 \sqrt{\frac{2\,e\,Z}{m_{ion}}} \frac{V_{extr}^{3/2}}{d^2} \tag{6.1}$$

where V_{extr} is the potential drop and d is the gap between the emission surface and the EG. For a circular aperture with radius r, one can define the aspect ratio $S = r/d$, so that the total extracted current reads:

$$I_{\mathrm{CL}} = \frac{4}{9}\pi\varepsilon_0\sqrt{\frac{2\,e\,Z}{m_{\mathrm{ion}}}}\,S^2\,V_{\mathrm{extr}}^{3/2} = P_{\mathrm{CL}}\,V_{\mathrm{extr}}^{3/2} \tag{6.2}$$

where the proportionality constant P_{CL} between the extractable ion current and the potential drop is called the perveance of the system. In the same way, the *perveance* P^* of an ion beam can be defined as:

$$P^* = \frac{I}{V_{\mathrm{extr}}^{3/2}} \tag{6.3}$$

In a real ion beam the current density in (6.1) depends on the ion density at the plasma meniscus, which is the ideal surface separating the plasma region in the source from the ion beam: the shape of the plasma meniscus adjusts in such a way that the electric field at this surface is zero and the space-charge limited current density in (6.1) equals the ion current density. Then the distance d^* between the meniscus and the extraction electrode has to be used in place of d in (6.2), for example for a concave boundary as in Figure 6.1, $d^* > d$ and the beam perveance P^* is reduced with respect to P_{CL}. In

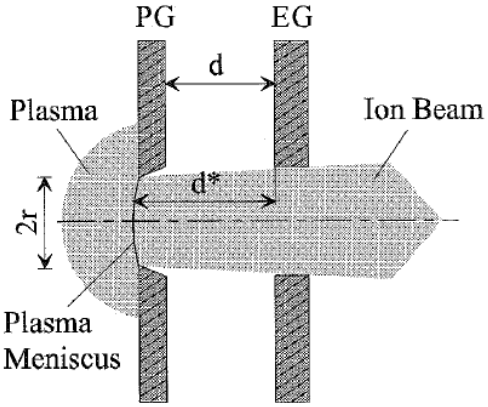

Figure 6.1: Diode extraction system and beam formation [5].

order to quantify the quality of the ion beam at the end of the accelerating column, one parameter that can be used is the beam *divergence*, which is the half width of the particle velocity distribution at $1/e$ of its maximum: if more than 80% of the ion beam current is found within a divergence angle of less than $\pm 20\,\mathrm{mrad}$, then the ion beam is said to be extracted in the perveance match condition [5]; the beam divergence can be minimized by regulating the shape and the voltage of the electrodes, but it cannot be zero because of the ion temperature and the thickness and shape of the plasma electrode.

In high energy ion sources instead of a diode system like the one used in the Child-Langmuir model, a multi-stage extraction and acceleration electrode system has to be used to prevent voltage breakdown between the grids and to limit the beam divergence during the acceleration. Once the extraction voltage is fixed, in order to increase the extracted current a multi-aperture system can be used instead of a single aperture, so that the total extractable ion current is the total aperture area multiplied by the space-charge limited current density, while the aspect ratio S is kept less than unity so as to keep the ion-emitting surface stable [5].

One of the issues in negative ion sources, is the presence of a co-extracted electron current, which in some cases is 100 times higher than the extracted ion current [11]. This represents a problem because:

- if the accelerated electrons cross the whole accelerating column, they would acquire the maximum energy and the dump on which they have to be deviated would be subjected to a high power deposition;
- acceleration of electrons decreases the accelerator efficiency;
- the electron space-charge inhibits the ion extraction.

For these reasons a set of small permanent magnets is usually embedded in the extraction grid, with their polarity parallel to the beam axis: in this way the resulting magnetic field, transverse to the beam axis, not only suppresses the electron extraction from the plasma source (the ions, being more massive, can cross the magnetic field more easily), but also deflects the extracted electrons onto the front surface of the extraction grid (which for this reason has to be adequately cooled).

Another problem in the acceleration of negative ion beams is represented by stripping reactions happening in the accelerating column due to the flowing neutral H_2 gas from the source towards the accelerator gaps:

$$H^- + H_2 \longrightarrow H^0 + H_2 + e \tag{6.4}$$

The neutral hydrogen atoms produced in this region have less than the full energy and usually posses higher divergence compared to the ions that cross the whole acceleration column; furthermore the electrons produced in the stripping reaction can represent a nonnegligible fraction of the power load on the accelerator grids because they are accelerated through the remaining part of the accelerator. For these reasons the background gas between the electrodes has to be as low as possible: since the gas pumped through the accelerator comes directly from the ion source, the target extracted ion current has to be achieved at a pressure as low possible (tipically $\simeq 0.3\,\mathrm{Pa}$).

6.2 NIO1 accelerating column

The negative ion source NIO1 (for a complete description of the experiment see Section 2.1) has been designed to accelerate to 60 keV a total H^- current of 130 mA: in order

to reach this current value the ions have to be generated in the source both via volume production (see Section 1.3) and surface production by the injection of Caesium gas in the extraction region. The accelerating column consists of four grids (see Figure 6.2), each one with a 3×3 matrix of apertures equally spaced by 14 mm (radius of the PG apertures 3.8 mm): speaking in terms of potential drops, NIO1 has been designed to operate at an extraction potential V_{extr} around 8 kV (potential drop between the PG and the EG) and an accelerating potential $V_{\mathrm{acc}} = 60$ kV (potential drop between the PG and the PA).

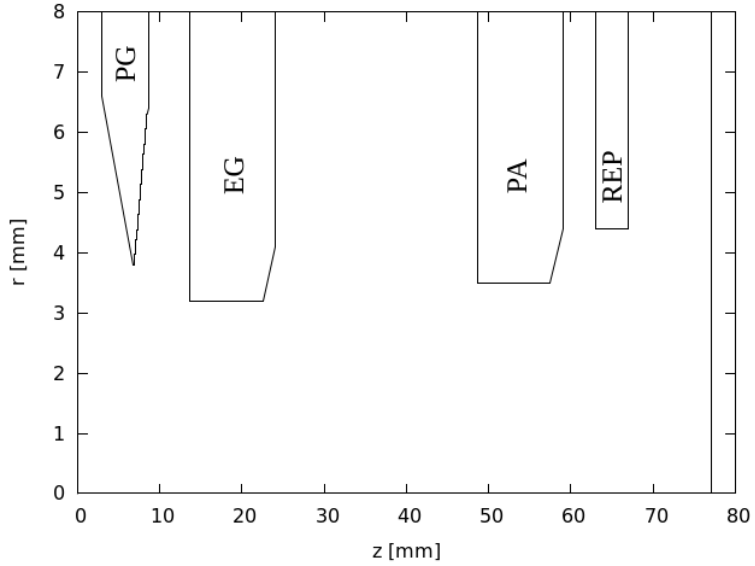

Figure 6.2: View of NIO1 grid system design in the (r,z) plane for a single aperture; this is the geometry used throughout the beam simulations.

In order to deflect the co-extracted electrons on the second grid, permanent magnets are embedded in the EG and in the PA with magnetization along the $\hat{z}$ direction (along the beam axis) and external iron shimming bars equalize the magnetic field: the resulting magnetic field corresponding to the central apertures (y=0) is shown in Figure 6.3; the magnetic field in the upper (y=14 mm) and lower (y=−14 mm) apertures is simply reversed. In order to reduce the stripping losses during the acceleration, the source operation pressure is 0.3 Pa-1 Pa; a turbomolecular and a rotary pump connected to the diagnostic chamber pump the gas through the electrode grids and through the large lateral windows between the arms that support the grids.

During the first experimental campaigns, NIO1 will be operated without the Caesium oven, so the the negative ions extracted from the source will be the ones generated via volume production only. Given the low pressure in the source, the extracted current density is expected to be substantially reduced with respect to the nominal value of about $300\,\mathrm{A\,m^{-2}}$: since it has been shown that the use of Caesium gas increases the negative

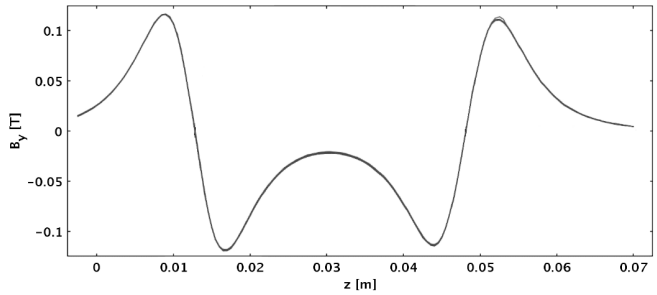

Figure 6.3: B_y profile in $y = 0$: in $y = \pm$ 14 mm the magnetic field is reversed [14].

ion production by $3-10$ times [5, p.361], in the following simulation an extracted current density $j_{H^-} = 30\,\mathrm{A\,m^{-2}}$ will be assumed.

It is interesting also to study the case of an oxygen beam, since before the operations in the hydrogen gas, air has been used as the filling gas. Air is composed of a mixture of about 78% nitrogen and 21% oxygen, but the negative ions in an air plasma are mostly O^- ions because oxygen has a higher electronegativity. In [48] some low power experiments, carried out with low RF power ($P < 50\,W$) in varying mixtures of N_2/O_2 plasmas, show that the negative ion density depends on the relative abundance of nitrogen in the mixture: this ion density decreases with the increase of $R = N_2/(N_2 + O_2)$. In particular for $R = 0.78$ (having a N_2/O_2 composition very similar to air), the negative ion density decreases by about 2 orders of magnitude. Since the value of the RF power in NIO1 is in the 1 kW range and the O^- density increases with the RF power [49] it can be concluded that an O^- density around 10^{17} m^{-3} is a realistic assumption; this value would justify an extracted current density in the range of some tens of $A\,m^{-2}$. In the following discussion then a value of $j_{O^-} = 30\,\mathrm{A\,m^{-2}}$ has been used to make a comparison with the hydrogen case.

6.3 Numerical simulations of the negative ion extraction

In order to make a self-consistent numerical simulation on the extraction region and the accelerated beam, a three dimensional model which solves the Poisson equation and the equation of motion taking into account the magnetic fields should be used. These codes, such as OPERA [50] or other 3-D codes [51], are essential in the final optimization of negative ion accelerators but are computationally heavy: for this reason in the initial optimization phase and in this thesis 2D codes as SLACCAD or simplified 3D codes as EAMCC (where the electric and magnetic fields are not calculated self-consistently) are used to simulate one of the 9 beamlets in the acceleration column in NIO1.

6.3.1 SLACCAD code and simulation results

SLACCAD is a 2D axial-symmetric code written in FORTRAN language used to calculate the self-consistent potential map of a beamlet of negative ions extracted from

a plasma and accelerated across a grid system [52, 53]. The space between the grids is divided in a square mesh and a certain potential has to be assigned the electrodes; the magnetic field as well as the presence of the other beamlets cannot be taken into account, since their presence would destroy the axial symmetry of the single beamlet problem.

In the first iteration it solves the Laplace equation:

$$\Delta\phi = 0 \tag{6.5}$$

The solution $\phi(r,z)$ is used to calculate the trajectories of the extracted ions, which are modelled as rays carrying a certain amount of charged particles: the rays start at a fixed z position before the plasma grid with a parallel velocity corresponding to few eV. The total extracted current density (e.g. $j_{H^-} = 30\,\mathrm{A\,m^{-2}}$) in divided among a certain number of macro-particles N, traced as rays according the potential map. The presence of the plasma is taken into account by imposing a region where $\phi = 0$ before the plasma grid, and adapting the interface of this region with the beam region (the so called *meniscus*) self-consistently, following an iterative approach. The space charge is then deposited in each mesh node in order to obtain the charge density $\rho(r,z)$, which is used in the Poisson equation:

$$\Delta\phi = \frac{\rho}{\varepsilon_0} \tag{6.6}$$

This equation is then integrated to find the new $\phi(r,z)$ which is used to calculate the new rays trajectories: this iterative process is repeated for a fixed number of iteration steps or until a convergence criterion is satisfied.

This code has been used to calculate the potential map both for H^- and O^- beamlets in the NIO1 grid geometry (see Figure 6.6), in the absence of stripping losses (without taking into account the pressure profile of the background gas) and of magnetic fields by using the following parameters:

- mesh size = 0.04 mm
- number of rays = 201
- emitter radial extent = 3.8 mm
- ion starting energy = 3 eV
- ions starting z position = 0.5 mm
- number of iterations = 97

The other input parameters are the grids potentials ϕ, which are set to different values during the simulations:

- $\phi_{PG} = 0$

- $\phi_{\mathrm{EG}} = V_{\mathrm{extr}}$
- $\phi_{\mathrm{PA}} = V_{\mathrm{acc}}$
- $\phi_{\mathrm{REP}} = V_{\mathrm{acc}}$

The optimal configuration for a certain extracted current and accelerating potential will be the one that produces a beam with minimum divergence which is sufficiently distant from the grids: this last requirement is necessary in order to avoid unwanted power load on the grids and is quantitatively described by a parameter called *clearance*. In SLACCAD the divergence is calculated as the RMS of the angle that each ray forms with the axial direction, multiplied by a weighting factor:

$$\text{divergence} = \sqrt{\sum_j \left(\frac{r_j \cdot \alpha_j^2}{\sum_j (r_j)} \right)} \tag{6.7}$$

where

$$\alpha_j = \arctan\left(\frac{v_{r,j}}{v_{z,j}} \right) \tag{6.8}$$

and the weighting factor $r_j / \sum_j (r_j)$ is to account for the fact that the external rays in this 2D simulation carry more current, so they weight more in the RMS calculation. In the post-analysis the clearance is calculated by simply evaluating the distance among the beam envelope (the radial coordinate of the more external ray for any given z position) and the aperture edges.

Previous simulations done using an extracted current $j_{\mathrm{H}^-} = 300\,\mathrm{A\,m^{-2}}$ with the nominal accelerating potential $V_{\mathrm{acc}} = 60\,\mathrm{kV}$ yield the results in Figure 6.4: at $V_{\mathrm{extr}} = 5.75\,\mathrm{kV}$ the divergence of the beam is minimum and the beam clearance at the EG is acceptable.

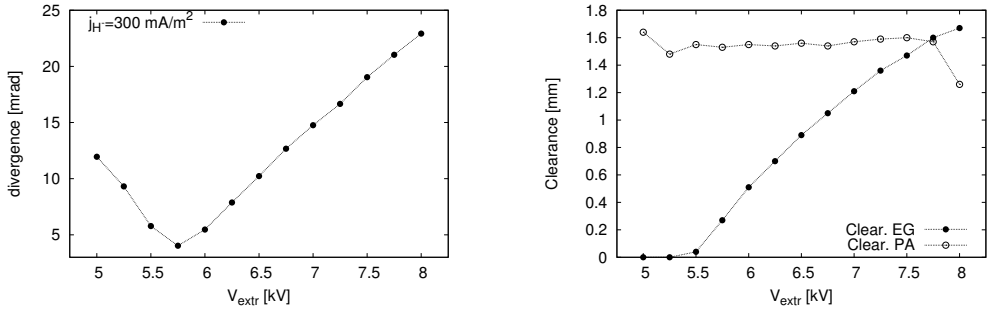

(a) Beam divergence. **(b)** Beam clearance at the EG and PA.

Figure 6.4: Results obtained in previous simulations using an extracted current $j_{\mathrm{H}^-} = 300\,\mathrm{A\,m^{-2}}$ and $V_{\mathrm{acc}} = 60\,\mathrm{kV}$ [54].

In order to preserve the perveance in the case of a lower extracted H^- current, the extraction and acceleration potentials have to be adjusted using the perveance definition in (6.3):

$$\frac{I}{V_{\text{extr}}^{3/2}} = \frac{I'}{V'_{\text{extr}}{}^{3/2}} \tag{6.9}$$

So the extraction potential for a beam with $30\,\text{A}\,\text{m}^{-2}$ current density in the same perveance condition as a $300\,\text{A}\,\text{m}^{-2}$ current density beam is:

$$V'_{\text{extr}} = 10^{-2/3} V_{\text{extr}} \simeq 0.22 \cdot V_{\text{extr}} \tag{6.10}$$

and the acceleration potential is scaled in the same way.

Various simulations have been done in a V_{acc} range around $12.9\,\text{kV} = 10^{-2/3}\,60\,\text{kV}$: for each of these values a scan in V_{extr} has been done to find the condition of minimum divergence. As can be seen in Figure 6.5(a) the minimum value of the beam divergence increases with the acceleration potential, however the hydrogen beam collides on the extraction grid EG for V_{acc} lower or equal to 12 kV (see Figure 6.5(b), where the clearances obtained at the minimum of each curve are plotted) thus resulting in beam losses and grid power load. In order to have a focused beam which in the absence of

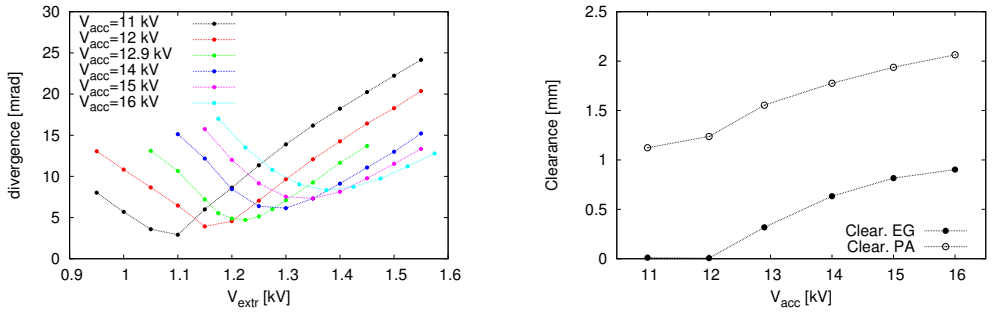

(a) Curves for the beam divergence at different V_{acc} values.

(b) Beam clearance at the EG and PA at the divergence minimum.

Figure 6.5: Results obtained using an extracted current $j_{H^-} = 30\,\text{A}\,\text{m}^{-2}$ and $V_{\text{acc}} = 11 - 12 - 12.9 - 14 - 15 - 16$ kV.

magnetic fields lies well away from the grids, a 16 kV acceleration potential has been used as a reference value: the minimum divergence is found at $V_{\text{extr}} \simeq 1375\,\text{V}$ and is 8.4 mrad; the beam trajectories obtained using these parameters as well as the equipotential lines are shown in Figure 6.6(a).

In the oxygen case, in order to obtain the guessed assumed current density $j_{O^-} = 30\,\text{A}\,\text{m}^{-2}$ the extraction potential has to be higher than in the hydrogen case, in

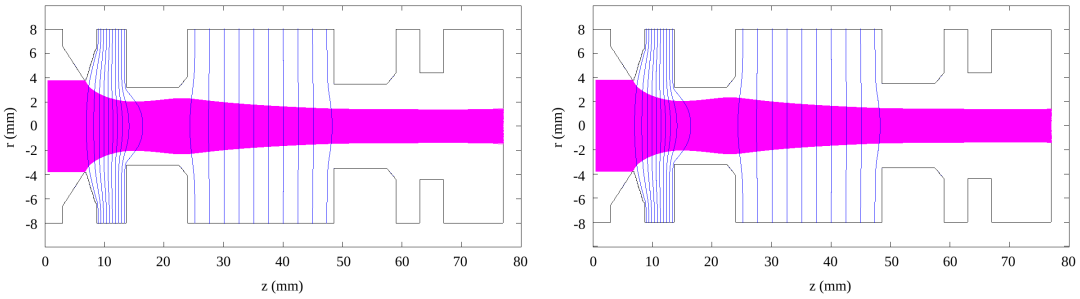

(a) Hydrogen beam: $V_{\text{acc}} = 16\,\text{kV}$, $V_{\text{extr}} = 1375\,\text{V}$.

(b) Oxygen beam: $V_{\text{acc}} = 40.32\,\text{kV}$, $V_{\text{extr}} = 3475\,\text{V}$.

Figure 6.6: Ray trajectories and equipotential lines obtained using the SLACCAD code (magnetic fields and stripping losses not included).

particular, by using (6.1), one has:

$$\frac{V_{\text{H}^-}^{3/2}}{m_{\text{H}^-}^{1/2}} = \frac{V_{\text{O}^-}^{3/2}}{m_{\text{O}^-}^{1/2}} \tag{6.11}$$

so that the scaled potential to be used in the oxygen beam simulation is:

$$V_{\text{O}^-} = \sqrt[3]{\frac{m_{\text{O}^-}}{m_{\text{H}^-}}} V_{\text{H}^-} \simeq 2.52 \cdot V_{\text{H}^-} \tag{6.12}$$

By using an acceleration potential $V_{\text{acc}} = 40.32\,\text{kV}$ and an ion mass $m_{\text{ion}} = 16\,\text{a.m.u.}$, the minimum divergence is found for $V_{\text{extr}} \simeq 3475\,\text{V}$ and is 7.8 mrad; the beam trajectories obtained using these parameters as well as the equipotential lines are shown in Figure 6.6(b).

6.3.2 EAMCC code and simulation results

The next step is to include the magnetic fields present in the acceleration column, which are necessary in order to deflect the coextracted electron current: for this purpose, the 3-dimensional EAMCC code (electrostatic accelerator Monte Carlo code) has been used [55].

This code takes as input the electrostatic potential map obtained in SLACCAD and the magnetic field map obtained from other numerical simulations and calculates the trajectories of an ensemble of macroparticles in these fields [56]. As previously said in NIO1 both the EG and the PA have permanent magnets embedded between each hole in the grid with alternating polarization for one hole to the next. The alternating polarization means that the simulation domain in EAMCC has to include two adjacent beamlets to properly describe all the particle trajectories. This is done as follows: a macroparticle is allowed to cross two holes (each with the correct EG magnetic field,

i.e., alternating in direction). A macroparticle leaving the calculation domain into what would be a neighboring hole is reinjected symmetrically into the domain. Collisions of particles are described using a Monte-Carlo method and include the following processes:

- electron and heavy particles collisions with accelerator grids;
- negative ion stripping reactions;
- ionization of the background gas.

Together with the co-extracted electrons, the secondary particles generated in the collisions are traced until they leave the accelerator or collide with a grid, producing a power density that can be calculated in the post-processing analysis: these profiles are interesting for the design of the grids and the dimensioning of the cooling system.

In order to give a first estimate of the power loads in this low current density regime, a H^- beam accelerated by $V_{\text{extr}} = 1.375\,\text{kV}$ and $V_{\text{acc}} = 16\,\text{kV}$ at a source operation pressure $p = 0.3\,\text{Pa}$ has been simulated, where the electrostatic potential is the one given by SLACCAD, the magnetic field is the one obtained by OPERA considering a residual field density $B_R = 1\,\text{T}$ for the magnets embedded in the EG (having size $L_x = 4\text{mm}$, $L_z = 5.2$ mm and $L_y = 64$ mm) and the background gas density in the acceleration column is the one in Figure 6.7. The trajectories calculated by EAMCC are shown in Figure 6.8, where the electrons are represented in red, the H^- ions in blue, the neutral H^0 in black, the H^+ ions in purple and the H_2^+ ions in green: as can be seen a lot of secondary particles are produced, which cross the simulation domain and are reinjected at the opposite side. Moreover the hydrogen beam is strongly deflected on the extraction grid by the magnetic field, so only a portion of it crosses the last grid: this is due to the fact that the voltage imposed at the accelerator grids is lower than the nominal one, so the H^- ions are slower and their Larmor radius is smaller; the beam crosses the last electrode about in its center because the magnetic field generated by the permanent magnets revers its direction after the EG, but is tilted with respect to the axis. If one wants to operate in hydrogen in a pure volume production configuration, it is then necessary to substitute the magnets installed in the grids with weaker ones: the magnetic field has to be strong enough as to deflect the majority of the co-extracted electrons on the EG, still maintaining a reasonable clearance a the EG aperture. Alternatively, the fraction of H^- ions colliding with the grids at low current can be minimized by using a beam optics with a high clearance, that is at a higher acceleration voltage as shown in Figure 6.5(b): this however results in a higher beam divergence as can be seen in Figure 6.5(a).

The power density deposition profiles for the hydrogen beam in Figure 6.8 on the acceleration grids are plotted in Figure 6.9: as can be seen the main power load is on the extraction and the post-acceleration grid, where the maximum power density is about $20\,\text{W}\,\text{cm}^{-2}$. As can be seen in Table 6.1 at the low current densities considered in this section ($j = 30\,\text{A}\,\text{m}^{-2}$) the power deposited on the electrodes by the secondary particles is negligible (below 10 W): the beam-gas and beam-surface interactions can

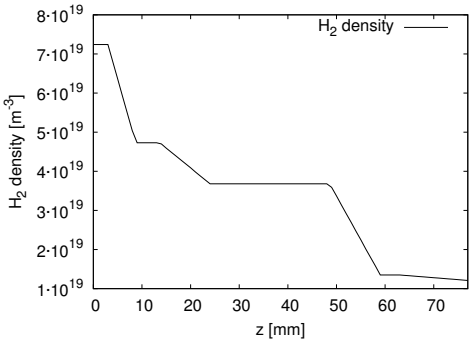

Figure 6.7: Background gas density profile at a source operation pressure of 0.3 Pa.

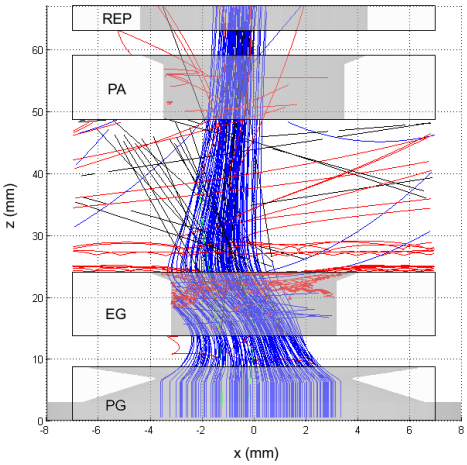

Figure 6.8: Particle trajectories for a H^- beam, $V_{acc} = 16\,kV$, $B_R = 1\,T$ and $p_{source} = 0.3\,Pa$.

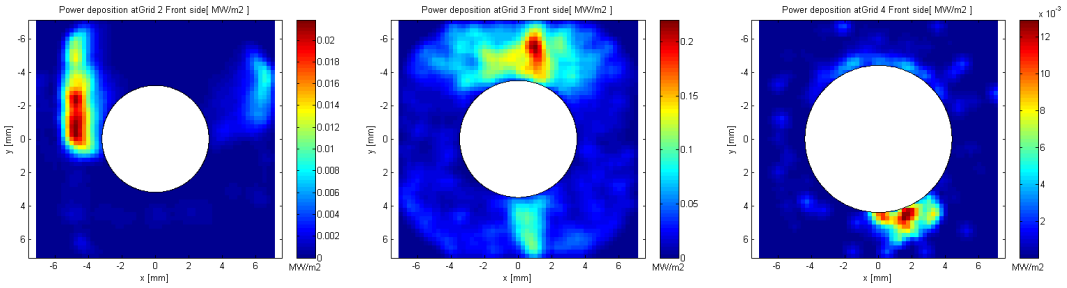

(a) Extraction grid. **(b)** Post-acceleration grid. **(c)** Grounded grid.

Figure 6.9: Power density deposition profiles on the front side of the acceleration grids in NIO1 for a H^- beam, $V_{extr} = 1.375\,kV$, $V_{acc} = 16\,kV$ and source pressure $p = 0.3\,Pa$.

then be neglected so that the EAMCC code, which in principle does not describe O^- interactions, can be used also in the oxygen beam case by changing only the ion mass.

In the following simulations then the secondary particle production is not included (the background gas density is set to 0) and the ion trajectories are evolved by considering the electric and magnetic fields only in order to evaluate the beam deflection.

As previously said, for a hydrogen beam at low current density the strength of the magnets in the EG has to be reduced, in particular an appropriate scaling for the magnetic field strength can be found from the expression for the Larmor radius r_L:

$$r_L = \frac{v\,m}{e\,B} = \frac{\sqrt{2\,e\,V_{extr}\,m}}{e\,B} \tag{6.13}$$

Table 6.1: Power deposited on the grids, transmitted back to the source and transmitted through the the REP for a H^- beam, $V_{extr} = 1.375\,kV$, $V_{acc} = 16\,kV$ and source pressure $0.3\,Pa$.

	PG [W]	EG [W]	PA [W]	REP [W]	Back [W]	Transmitted [W]
e^-	$1.39 \cdot 10^{-6}$	0.371	2.42	0.279	0	1.69
H^-	0	5.69	4.26	0.0077	0	112
H^0	0.0022	0.187	1.01	0.0163	0.0027	10.5
H^+	$2.28 \cdot 10^{-4}$	0.0404	0.0057	$3.26 \cdot 10^{-5}$	0.0933	0.289
H_2^+	0	0.0698	0	0	0.891	$6.31 \cdot 10^{-5}$
Total	**0.0024**	**6.36**	**7.70**	**0.303**	**0.987**	**124.5**

In order to have an ion beam deflection comparable to the one obtained in the case of high current density, the ion Larmor radius in the two cases has to be equal, in particular the following relationship has to be satisfied:

$$\frac{\sqrt{V_{extr}}}{B} = \frac{\sqrt{V'_{extr}}}{B'} \tag{6.14}$$

where the prime indicates the quantities relative to the low current case. As previously said, when a scaling $R_I = I/I'$ is adopted, a corresponding scaling in the extraction voltage has to be done to preserve the perveance (see (6.9)), in particular:

$$\frac{V_{extr}}{V'_{extr}} = R_I^{2/3} \tag{6.15}$$

When this equation is substituted in (6.14), the following expression for the magnetic field scaling is obtained:

$$\frac{B'}{B} = R_I^{-1/3} \tag{6.16}$$

In particular, for $j_{H^-} = 300\,A\,m^{-2}$ and $j'_{H^-} = 30\,A\,m^{-2}$, $R_I = 10$, so that $B' \simeq 0.46\,B$. The magnetic field calculated by OPERA considers a residual field density $B_R = 1\,T$: since the ferrite magnets that can be used in place of the magnets embedded in the EG have a $B_R \simeq 0.4\,T$, a correct scaling for a low current hydrogen beam can be obtained by multiplying the magnetic field calculated by OPERA by a factor of 0.4.

A H^- beam and an O^- beam have then been simulated using the following parameters:

- number of rays = 500
- emitter radial extent = 3.8 mm
- ion starting longitudinal energy = 3 eV

- ion starting transverse energy = 0 eV
- ion starting z position = 0.5 mm
- ion time step = $1 \cdot 10^{-10}$ s

The electric potentials used in the simulation are those in Figure 6.6; the magnetic field is the one calculated by OPERA for the oxygen beam, while for the hydrogen beam the same field has been scaled by a factor 0.4; the results obtained are those in Figure 6.10.

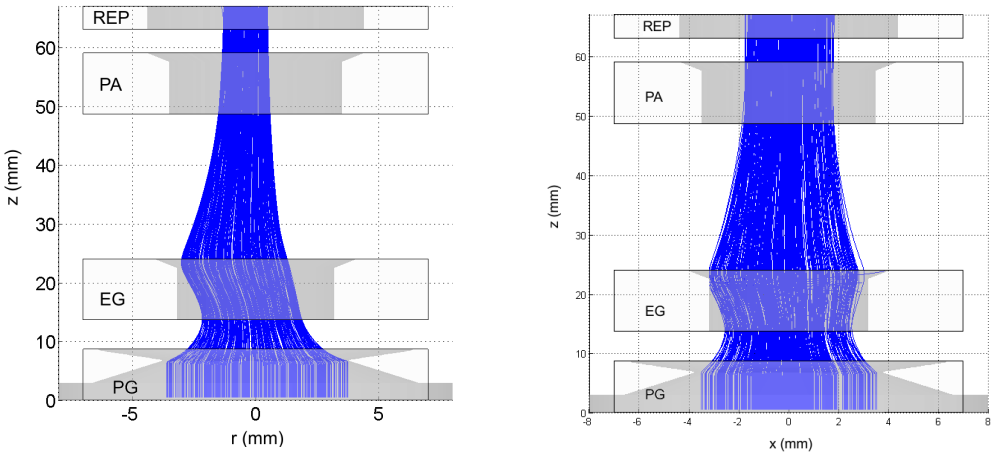

(a) Hydrogen beam, $B_R = 0.4$ T. **(b)** Oxygen beam, $B_R = 1$ T.

Figure 6.10: Particle trajectories from EAMCC simulation.

As can be easily seen the hydrogen beam is still deflected by the magnetic field, but thanks the the scaling used it no longer collides with the extraction grid. As previously said a higher clearance could be obtained by using a higher acceleration voltage, at the expense of the beam divergence.

The oxygen beam on the other hand is not substantially deviated even when using the magnets with $B_R = 1$ T because of the higher mass of the ions involved ($m_O \simeq 16 m_H$), but has a larger envelope than the one found in the SLACCAD simulation (see Figure 6.6(b)) so the more external part of the beam slightly collides with the extraction grid. During operation in air then it is sufficient to use a higher accelerating voltage to reduce the beam radius without the need to substitute the permanent magnets embedded in the grids.

It is to be noted that this code is not self-consistent, in particular the real electric potential in the acceleration column would be different from the one calculated in the axial-symmetric approximation especially at high beam deflections as in the hydrogen case: however, in more symmetric beams such as in the oxygen case, the use of the SLACCAD potential instead of a self-consistenly calculated one is still a good approximation.

Even though for the low current density hydrogen beam the profiles obtained in the

SLACCAD and the EAMCC simulation are substantially different, the two can be correlated as shown in Figure 6.11, where a hydrogen beam with magnets in the EG having $B_R = 1\,\mathrm{T}$ has been considered: as it can be seen there is a linear dependence between the fraction of particles transmitted (particles that cross the REP) calculated by EAMCC and the clearance at the extraction grid found in the SLACCAD simulation; these values are the ones calculated at the minimum of the beam divergence for each V_{acc} used.

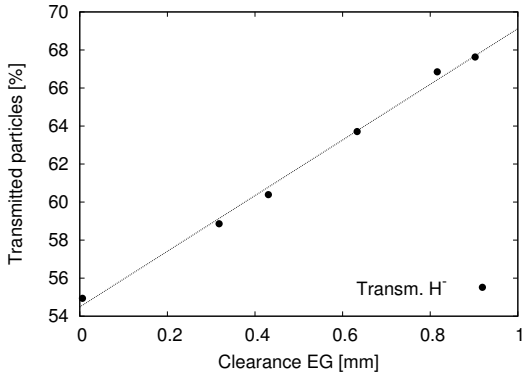

Figure 6.11: Linear dependence between the fraction of transmitted particles as calculated by EAMCC and the beam clearance at the EG as calculated by SLACCAD (hydrogen beam, $B_R = 1\,\mathrm{T}$).

CHAPTER 7

Conclusions

Development and optimization of radiofrequency negative ion sources, like the recently installed NIO1, require a deep understanding of the crucial issues concerning this kind of ion sources. In particular the following aspects have been examined and modeled in the present thesis:

- radiofrequency power coupling to a low pressure plasma;
- filtering of the electron distribution function, which is necessary in order to obtain cold plasmas ($T_e < 2\,\mathrm{eV}$);
- negative ion beam extraction also in the context of current density values that are strongly different from the optimal ones.

In order to study the inductive coupling between the coil and the plasma in the driver region, two heating mechanisms have been taken into consideration: the first is a local ohmic heating due to electron collisions with ions and neutrals inside the plasma, the second is a nonlocal or stochastic heating due to the non-uniformity of the electric field inside the plasma; to describe the latter effect a stochastic collision frequency has been defined and an analytical expression (that depends on the product of the electron density and the electron temperature) for this quantity has been found. Local and nonlocal effects have been modelled altogether by an effective collision frequency, defined as the sum of the electron-neutral and electron-ion collision frequencies and the stochastic collision frequency. The analytic model proposed for the inductive coupling, which assumes uniform electron temperature and density in the driver region, gives an estimate of the power coupling efficiency as a function of the plasma temperature and density. Even if the model is greatly simplified, the value of the capacitors used during the first experimental measurements in NIO1 is in the same order of magnitude as the results of the simulation.

A model for the profile of plasma parameters in the whole source has then been proposed: this assumes a quasi-neutral plasma in which only electrons and one ion species are present and considers the diffusion and energy equations for the electrons;

the plasma confinement effect, due the magnetic multipole configuration in NIO1, has been included in the model by setting different particle and energy fluxes at the walls where magnets are present. The model has been implemented in a multiphysics software for a hydrogen, nitrogen and oxygen gas separately: the input power density profile used in the energy equation for a hydrogen gas is calculated by considering the electric field generated by the coil in vacuum and the expression for the effective collision frequency calculated in the preceding model. In future the model could be improved using the absorbed power density profile obtained by simulating the electric field produced by the coil in the plasma.

The dependence of plasma parameter profiles on gas pressure and absorbed power has been studied. It is found that at fixed pressure for all these gases the electron temperature does not change with the absorbed power, while the dependence of the electron density on the absorbed power is linear, a behaviour that is compatible with the experimental measurements made on NIO1. When the power is fixed, with decreasing gas pressure there is a steepening in the profiles of plasma parameters and an increase in the electron temperature; the electron density instead at low pressures (below 1 Pa) increases with increasing pressure in the absence of magnetic confinement or remains constant when the magnets are considered, while at high pressures the electron density shows a decrease with increasing gas pressure. In particular at an operation pressure $p_{\mathrm{gas}} = 0.3\,\mathrm{Pa}$ and absorbed power $P_{\mathrm{abs}} = 2\,\mathrm{kW}$, $T_e \simeq 11\,\mathrm{eV}$ and $n_e \simeq 2 \cdot 10^{17}\,\mathrm{m}^{-3}$ in a hydrogen discharge, which are values compatible with those obtained in other experiments.

A sample of electrons following a Maxwellian distribution with temperature 10 eV has then been evolved through the magnetic filter field generated by the current flowing in the plasma grid in NIO1 by the use of a Monte Carlo approach, where elastic, Coulomb and ionizing collisions have been considered. From the electron energy probability function calculated by the simulation, the electron temperature and density across the magnetic filter have been computed: the results show that the electron density experiences a decrease of a factor of 20 from the electron starting point to the sheath edge and that there is an effective electron cooling when approaching the plasma grid, in particular the electrons reach a final temperature of about 4 eV with a 500 A current flowing in the plasma grid. The value shown by the simulation in this simplified magnetic configuration is however slightly in excess with respect to the optimal range for H^- production, which requires temperatures lower than 2 eV. A further decrease in electron temperature can be achieved by increasing the strength of the magnetic filter field, for example by adding dipole components into the front magnetic multipole assembly.

Finally, a hydrogen and an oxygen beam have been simulated in a scenario of a strongly off-normal condition of the source, in particular the extracted negative ion current density was assumed $30\,\mathrm{A\,m^{-2}}$ (a typical expected value for the first operations of NIO1 without caesium) instead of $300\,\mathrm{A\,m^{-2}}$ (which is the design value in the case of caesium operation). The electrode potentials to be used for optimal focusing of the hydrogen beam have been found according to the constant perveance scaling, but it

has been shown that the magnets embedded in the extraction grid cause a significant deflection of the extracted ions onto the extraction grid itself due to the relatively low acceleration voltage used unless a corresponding scaling in the strength of the magnets is applied. This scaling however is not necessary for oxygen, where the beam is only slightly deviated because of the higher acceleration voltage used and the higher ion mass. For this reason, when operating with a hydrogen plasma in a volume production configuration (that is with no caesium), the permanent magnets in the extraction system should be subsituted with ones having a 60% weaker strength.

In conclusion, the model developed in this thesis will be helpful in guiding the experimental activity and optimization of NIO1 with the perspective of a better understanding of the physics involved in large neutral beam injectors like those for the ITER project.

Bibliography

[1] M. Kikuchi, K. Lackner, and M. Tran, eds.: *Fusion Physics*. Vienna: International Atomic Energy Agency (IAEA), 2012: pp. 7–8.

[2] K. Miyamoto: *Plasma Physics for Nuclear Fusion*. Cambridge, Massachusetts: MIT Press, 1989: pp. 3–11.

[3] J. Wesson: *Tokamaks*. Oxford: Clarendon Press, 2004: p. 4.

[4] EFDA, European Fusion Development Agreement, glossary webpage. URL: `http://www.efda.org/glossary/tokamak`.

[5] G. Brown (Ed.): *The Physics and Technology of Ion Sources*. Weinheim: Wiley-VCH Verlag GmbH & Co. KGaA, 2004: pp. 159–187.

[6] R. V. Lovelace: Lowfrequency stability of highcurrent particle rings. *Physics of Fluids (1958-1988)*, **19** (1976): p. 723. DOI: `10.1063/1.861531`.

[7] G. Grieger, H. Renner, and H. Wobig: Wendelstein stellarators. *Nuclear Fusion*, **25**(9) (1985): p. 1231. DOI: `10.1088/0029-5515/25/9/040`.

[8] J. H. Harris, J. L. Cantrell, T. C. Hender, B. A. Carreras, and R. N. Morris: A flexible heliac configuration. *Nuclear Fusion*, **25**(5) (1985): p. 623. DOI: `10.1088/0029-5515/25/5/005`.

[9] ITER official website. URL: `http://www.iter.org`.

[10] M. A. Lieberman and A. J. Lichtenberg: *Principles of Plasma Discharges and Materials Processing*. New York: John Wiley & Sons, 1994: p. 137.

[11] R. S. Hemsworth and T. Inoue: Positive and negative ion sources for magnetic fusion. *IEEE Transactions on Plasma Science*, **33**(6) (2005): pp. 1799–1813. DOI: `10.1109/TPS.2005.860090`.

[12] ITER EDA Documentation Series 22: *Summary of the ITER Final Design Report*. Vienna: IAEA, 2001: p. 21.

[13] M. Cavenago et al.: Construction of a versatile negative ion source and related developments. *AIP Conf. Proc.*, **1515** (2013): p. 157. DOI: `10.1063/1.4792782`.

[14] M. Cavenago, V. Antoni, T. Kulevoy, S. Petrenko, G. Serianni, and P. Veltri: 'Development of Small Multiaperture Negative Ion Beam Sources and Related Simulation Tools'. *Negative Ions, Beams and Sources*. Vol. 1097. AIP, 2009: p. 149. DOI: 10.1063/1.3112508.

[15] M. Cavenago et al.: Installation of a versatile multiaperture negative ion source. *Review of Scientific Instruments*, **85** (2014): 02A704. DOI: 10.1063/1.4824809.

[16] A. Mimo: *Diagnostics for negative ion source NIO1*. Master thesis. Università degli Studi di Padova, Physics and Astronomy Department, 2014.

[17] A. Lieberman and V. A. Godyak: From Fermi Acceleration to Collisionless Discharge Heating. *IEEE Transactions on Plasma Science*, **26**(3) (1998): p. 955. DOI: 10.1109/27.700878.

[18] Y. P. Raizer: *Gas Discharge Physics*. Berlin, Heidelberg, New York: Springer-Verlag, 1991: pp. 35–40.

[19] J. Yoon, M. Song, J. Han, S. Hwang, W. Chang, B. Lee, and Y. Itikawa: Cross Sections for Electron Collisions with Hydrogen Molecules. *Journal of Physical and Chemical Reference Data*, **37**(2) (2008): p. 918. DOI: 10.1063/1.2838023.

[20] R. K. Janev, W. D. Langer, K. Evans Jr., and Douglass E. Post Jr.: *Elementary Processes in Hydrogen-Helium Plasmas*. Berlin, Heidelberg, New York: Springer-Verlag, 1987: pp. 34–54,172. DOI: 10.1007/978-3-642-71935-6.

[21] I. Hutchinson: *Collisions in plasmas*. Lecture notes. 2003. URL: http://ocw.mit.edu/courses/nuclear-engineering/22-611j-introduction-to-plasma-physics-i-fall-2006/readings/chap3.pdf.

[22] V. Vahedi, M. A. Lieberman, G. DiPeso, T. D. Rognlien, and D. Hewett: Analytic model of power deposition in inductively coupled plasma sources. *Journal of Applied Physics*, **78**(3) (1995): p. 1446. DOI: 10.1063/1.360723.

[23] R. B. Piejak, V. A. Godyak, and B. M. Alexandrovich: A simple analysis of an inductive RF discharge. *Plasma Sources Sci. Technol.*, **1**(10) (1992): p. 180. DOI: 10.1088/0963-0252/1/3/006.

[24] H. Nagaoka: The inductance coefficients of solenoids. *Journal of the College of Science*, **27**(3) (1909): p. 31.

[25] COMSOL Multiphysics official website. URL: http://www.comsol.com.

[26] Ts. Paunska, A. Shivarova, and Kh. Tarnev: A small radius hydrogen discharge: An effective source of volume produced negative ions. *Journal of Applied Physics*, **107**(8) (2010): p. 083301. DOI: 10.1063/1.3369277.

[27] A. V. Phelps: Cross sections and swarm coefficients for nitrogen ions and neutrals in N_2 and argon ions and neutrals in Ar for energies from 0.1 eV to 10 keV. *Journal of Physical and Chemical Reference Data*, **20**(3) (1991): p. 563. DOI: 10.1063/1.555889.

[28] G. Roberson, M. Roberto, J. Verboncoeur, and P. Verdonck: Global model simulations of low-pressure oxygen discharges. *Brazilian Journal of Physics*, **37**(2a) (2007): pp. 457–465. doi: 10.1590/S0103-97332007000300019.

[29] M. Cavenago and S. Petrenko: Models of radiofrequency coupling for negative ion sources. *Review of Scientific Instruments*, **83** (2012): 02B503. doi: 10.1063/1.3670601.

[30] A. R. Choudhuri: *The Physics of Fluids and Plasmas*. Cambridge: Cambridge University Press, 1998: p. 43.

[31] Ts. Paunska, H. Schlüter, A. Shivarova, and Kh. Tarnev: Low pressure hydrogen discharges. *Physics of Plasmas*, **13** (2006): p. 023504. doi: 10.1063/1.2172541.

[32] G. Matthieussent and J. Pelletier: *Microwave Excited Plasmas*. Ed. by M. Moissan and J. Pelletier. Amsterdam: Elsevier, 1992. Chap. 11-12. doi: 10.1002/ctpp.2150340111.

[33] Y. Itikawa: Cross Sections for Electron Collisions with Nitrogen Molecules. *Journal of Physical and Chemical Reference Data*, **35**(1) (2006): p. 33. doi: 10.1063/1.1937426.

[34] Y. Itikawa: Cross Sections for Electron Collisions with Oxygen Molecules. *Journal of Physical and Chemical Reference Data*, **38**(1) (2009): pp. 1–20. doi: 10.1063/1.3025886.

[35] L. Schiesko, P. McNeely, P. Franzen, U. Fantz, and the NNBI Team: Magnetic field dependence of the plasma properties in a negative hydrogen ion source for fusion. *Plasma Physics and Controlled Fusion*, **54** (2012): p. 105002. doi: 10.1088/0741-3335/54/10/105002.

[36] K. Behringer and U. Fantz: Spectroscopic diagnostics of glow discharge plasmas with non-Maxwellian electron energy distributions. *Journal of Physics D: Applied Physics*, **27**(10) (1994): p. 2128. doi: 10.1088/0022-3727/27/10/021.

[37] V. Vahedi and M. Surendra: A Monte Carlo collision model for the particle-in-cell method: applications to argon and oxygen discharges. *Computer Physics Communications*, **87** (1995): pp. 179–198. doi: 10.1016/0010-4655(94)00171-W.

[38] D. Wünderlich, R. Gutser, U. Fantz, and NNBI-Team: *Transport of charged particles in the magnetic filter field of RF sources for the production of negative hydrogen ions*. 20^{th} ESCAMPIG Conf. Proc. 2010. url: http://www.escampig2010.ipb.ac.rs/papers/P3.27.pdf.

[39] W. Press, S. Teulkolsky, W. Vetterling, and B. Flannery: *Numerical Recipes in C: The Art of Scientific Computing*. Cambridge: Cambridge University Press, 1992: p. 290.

[40] C. K. Birdsall and A. B. Langdon: *Plasma Physics via Computer Simulations*. Philadelphia: Institute of Physics Publishing, 1991: p. 62.

[41] S. Gasiorowicz: *Quantum Physics, 3rd Ed.* New York: Wiley, 2003: p. 248.

[42] K. Nanbu: Theory of cumulative small-angle collisions in plasmas. *Physical Review E*, **55**(4) (1997): p. 4642. doi: 10.1103/PhysRevE.55.4642.

[43] C. B. Opal, W. K. Peterson, and E. C. Beaty: Measurements of Secondary Electron Spectra Produced by Electron Impact Ionization of a Number of Simple Gases. *Journal of Chemical Physics*, **55** (1971): p. 4100. doi: 10.1063/1.1676707.

[44] V. A. Godyak, R. B. Piejak, and B. M. Alexandrovich: Electron energy distribution function measurements and plasma parameters in inductively coupled argon plasma. *Plasma Sources Science and Technology*, **11** (2002): p. 532. doi: 10.1088/0963-0252/11/4/320.

[45] A. Aanesland, J. Bredin, P. Chabert, and V. Godyak: Electron energy distribution function and plasma parameters across magnetic filters. *Applied Physics Letters*, **100** (2012): p. 044102. doi: 10.1063/1.3680088.

[46] C. D. Child: Discharge From Hot CaO. *Physical Review (Series I)*, **32**(5) (1911): pp. 492–511. doi: 10.1103/PhysRevSeriesI.32.492.

[47] I. Langmuir and K. T. Compton: Electrical Discharges in Gases Part II. Fundamental Phenomena in Electrical Discharges. *Review of Modern Physics*, **3**(2) (1931): pp. 191–257. doi: 10.1103/RevModPhys.3.191.

[48] S. Ono, H. Kato, and S. Teii: Simulation and Experiment of Low-Pressure Oxygen-Nitrogen Mixture Gas Glow Discharge Plasma. *Combustion Science and Technology*, **133** (1998): pp. 151–160. doi: 10.1080/00102209808952033.

[49] J. Kim, G. Kim, T. Chung, G. Yeom, and K. Kwon: Characterization of an Oxygen plasma by using a Langmuir probe in an inductively coupled plasma. *Journal of the Korean Physical Society*, **38**(3) (2001): pp. 259–263.

[50] Vector Fields OPERA-3D software, Cobham plc, Brook Road, Wimborne, Dorset, BH21 2BJ, UK. url: http://operafea.com/.

[51] F. Taccogna, P. Minelli, and S. Longo: Three-dimensional structure of the extraction region of a hybrid negative ion source. *Plasma Sources Science and Technology*, **22**(4) (2013): p. 045019. doi: 10.1088/0963-0252/22/4/045019.

[52] W. B. Herrmannsfeldt: *Electron trajectory program*. Tech. rep. SLAC-226. Stanford Linear Accelerator Center, 1979.

[53] J. Pamela: A model for negative ion extraction and comparison of negative ion optics calculations to experimental results. *Review of Scientific Instruments*, **62**(5) (1991): pp. 1163–1172. doi: 10.1063/1.1141995.

[54] P. Veltri, M. Cavenago, and C. Baltador: '*Design of the new extraction grid for the NIO1 negative ion source*'. Submitted to AIP Conf. Proceedings of the IV International Symposium on Negative Ions, Beams, and Sources, Garching bei Munchen (DE). 2014.

[55] G. Fubiani, H. P. L. de Esch, A. Simonin, and R. S. Hemsworth: Modeling of secondary emission processes in the negative ion based electrostatic accelerator of the International Thermonuclear Experimental Reactor. *Physical Review ST Accelerator and Beams*, **11** (2008): p. 014202. doi: 10.1103/PhysRevSTAB.11.014202.

[56] M. Cavenago and P. Veltri. Accepted for publication on Plasma Source, Science and Technology. 2014.

[57] J. T. Gudmundsson: *Electron excitation rate coefficients for the nitrogen discharge*. Tech. rep. RH-09-2005. University of Iceland, 2005.

[58] J. T. Gudmundsson: *Notes on the electron excitation rate coefficients for argon and oxygen discharge*. Tech. rep. RH-21-2002. University of Iceland, 2002.

[59] L. Brieda: *Particle Push in Magnetic Field (Boris Method)*. url: http://www.particleincell.com/blog/2011/vxb-rotation.

APPENDIX A

Source modelling

A.1 Matching circuit

Here the detailed calculation for the expression given in Section 3.2.1 for the capacitors to be used in the matching box (see Figure 3.9 for the notation).

$$\frac{1}{Z_{eq}} = \frac{1}{iX_2} + \frac{1}{R_L + i(X_L + X_1)} = -\frac{i}{X_2} + \frac{R_L - i(X_L + X_1)}{R_L^2 + (X_L + X_1)^2} \tag{A.1}$$

To have the maximum power transfer $Y_{eq} = G_{eq} + iB_{eq} = 1/R_T$:

$$G_{eq} = \frac{R_L}{R_L^2 + (X_L + X_1)^2} \qquad = \frac{1}{R_T} \tag{A.2}$$

$$B_{eq} = -\frac{1}{X_2} - \frac{(X_L + X_1)}{R_L^2 + (X_L + X_1)^2} = 0 \tag{A.3}$$

The reactance X_1 of the capacitor in series with the coil is obtained from the first equation:

$$R_L R_T = R_L^2 + (X_L + X_1)^2 \Rightarrow X_L + X_1 = \sqrt{R_L(R_T - R_L)} \tag{A.4}$$

From the second one and using (A.4) one has the reactance X_2 of the capacitor in parallel with the coil:

$$X_2 = -\frac{R_L^2 + (X_L + X_1)^2}{X_L + X_1} = -\frac{R_L R_T}{\sqrt{R_L(R_T - R_L)}} \tag{A.5}$$

A.2 Energy loss per electron-ion pair created

The electron energy loss per electron-ion pair created ε_L has been used in Section 4.2 and is defined as:

$$k_{iz}\,\varepsilon_L \equiv k_{iz}\,\varepsilon_{iz} + \sum_i k_{exc,i}\,\varepsilon_{exc,i} + k_{el}\,\frac{3\,m_e}{m_i}\,T_e \tag{A.6}$$

where k_j is the reaction rate for the process j and ε_j is its threshold energy, in particular at the RHS of (A.6):

- k_{iz} and ε_{iz} are respectively the ionization reaction rate and the ionization energy;
- $k_{exc,i}$ and $\varepsilon_{exc,i}$ are respectively the reaction rate and the energy threshold for the excitation process i;
- k_{el} is the elastic collision reaction rate, which is multiplied by the the mean energy lost per electron for a polarization scattering [10].

A.2.1 Hydrogen discharge

For a molecular hydrogen discharge, the processes considered are those in Table A.1. The reaction rates corresponding to these processes are taken from [20] whereas for elastic collisions it is obtained averaging the elastic cross section in [19] over a maxwellian distribution function. A summary of the reaction rates is plotted in Figure A.1; in Figure A.2 the electron energy loss per electron-ion pair created obtained using (A.6).

Table A.1: Reaction rates for electron collisions in H_2 .

process	$\varepsilon_{threshold}$ **[eV]**
$e + H_2 \longrightarrow 2e + H_2^+$	15.43
$e + H_2 \longrightarrow e + H_2[\nu = 1]$	0.516
$e + H_2 \longrightarrow e + H_2[\nu = 2]$	1.182
$e + H_2 \longrightarrow e + H_2[B^1\Sigma_u^+]$	11.18
$e + H_2 \longrightarrow e + H_2[C^1\Pi_u]$	12.29
$e + H_2 \longrightarrow e + H_2[E,F^1\Sigma_g^+]$	12.3
$e + H_2 \longrightarrow e + 2H[G]$	4.52
$e + H_2 \longrightarrow e + H[G] + H[2s]$	14.7
$e + H_2 \longrightarrow e + H[2p] + H[2s]$	24.9
$e + H_2 \longrightarrow e + H[G] + H[n = 3]$	16.6

A.2.2 Nitrogen discharge

For a molecular nitrogen discharge, the processes considered are those in Table A.2. The reaction rates corresponding to these processes and the elastic collisions are taken

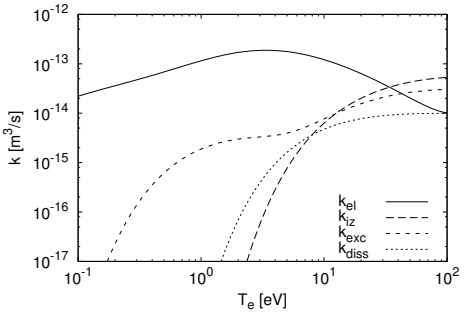

Figure A.1: Reaction rates for electron collisions in molecular hydrogen.

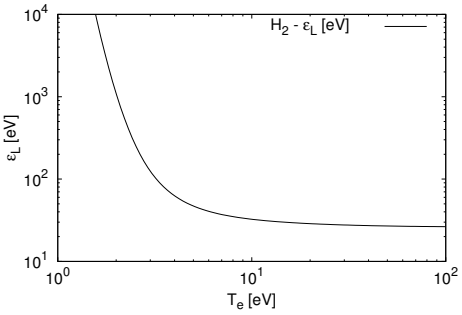

Figure A.2: Electron energy loss per electron-ion pair created in H_2.

from [57]. A summary of the reaction rates is plotted in Figure A.3; in Figure A.4 the electron energy loss per electron-ion pair created obtained using (A.6).

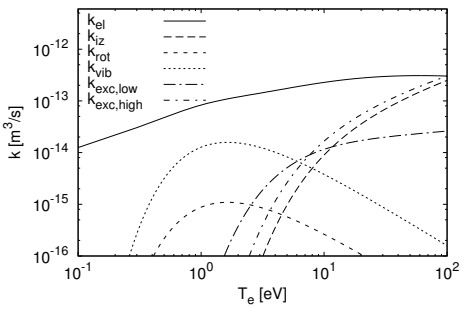

Figure A.3: Reaction rates for electron collisions in molecular nitrogen.

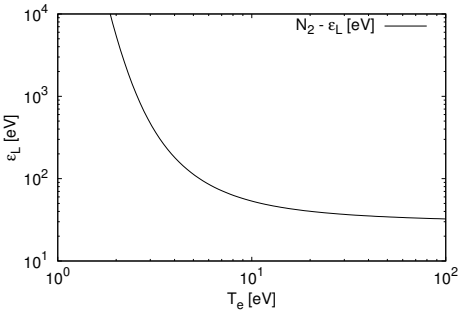

Figure A.4: Electron energy loss per electron-ion pair created in N_2.

A.2.3 Oxygen discharge

For a molecular oxygen discharge, the processes considered are those in Table A.3. The reaction rates corresponding to these processes and the elastic collisions are taken from [58]. A summary of the reaction rates is plotted in Figure A.5; in Figure A.6 the electron energy loss per electron-ion pair created obtained using (A.6).

Table A.2: Reaction rates for electron collisions in N_2 .

process	$\varepsilon_{threshold}$ **[eV]**
$e + N_2 \longrightarrow 2e + N_2^+$	15.6
$e + N_2 \longrightarrow e + N_2[r > 0]$	0.02
$e + N_2 \longrightarrow e + N_2[\nu = 1]$	0.29
$e + N_2 \longrightarrow e + N_2[\nu = 2]$	0.59
$e + N_2 \longrightarrow e + N_2[\nu = 3]$	0.88
$e + N_2 \longrightarrow e + N_2[\nu = 4]$	1.17
$e + N_2 \longrightarrow e + N_2[\nu = 5]$	1.47
$e + N_2 \longrightarrow e + N_2[\nu = 6]$	1.76
$e + N_2 \longrightarrow e + N_2[\nu = 7]$	2.06
$e + N_2 \longrightarrow e + N_2[\nu = 8]$	2.35
$e + N_2 \longrightarrow e + N_2[A^3\Sigma_u^+](\nu = 0 - 4)$	6.17
$e + N_2 \longrightarrow e + N_2[A^3\Sigma_u^+](\nu = 5 - 9)$	7.0
$e + N_2 \longrightarrow e + N_2[B^3\Pi_g]$	7.35
$e + N_2 \longrightarrow e + N_2[W^3\Delta_u]$	7.36
$e + N_2 \longrightarrow e + N_2[A^3\Sigma_u^+](\nu > 10)$	7.80
$e + N_2 \longrightarrow e + N_2[B'^3\Pi_u^-]$	8.16
$e + N_2 \longrightarrow e + N_2[a'^1\Sigma_u^-]$	8.40
$e + N_2 \longrightarrow e + N_2[a^1\Pi_g]$	8.55
$e + N_2 \longrightarrow e + N_2[w^1\Pi_u]$	8.89
$e + N_2 \longrightarrow e + N_2[C^3\Pi_u]$	11.03
$e + N_2 \longrightarrow e + N_2[E^3\Sigma_g^+]$	11.88
$e + N_2 \longrightarrow e + N_2[a''^1\Sigma_g^+]$	12.25

Table A.3: Reaction rates for electron collisions in O_2 .

process	$\varepsilon_{threshold}$ **[eV]**
$e + O_2 \longrightarrow 2e + O_2^+$	12.06
$e + O_2 \longrightarrow e + O_2[r > 0]$	0.02
$e + O_2 \longrightarrow e + O_2[\nu = 1]$	0.19
$e + O_2 \longrightarrow e + O_2[\nu = 2]$	0.38
$e + O_2 \longrightarrow e + O_2[a^1\Delta_g]$	0.977
$e + O_2 \longrightarrow e + O_2[b^1\Sigma_g^+]$	1.627
$e + O_2 \longrightarrow e + O_2[c^1\Sigma_u^-, A^3\Sigma_u^+]$	4.5
$e + O_2 \longrightarrow e + O(3P) + O(3P)$	6.0
$e + O_2 \longrightarrow e + O(3P) + O(1D)$	8.4
$e + O_2 \longrightarrow e + O(1D) + O(1D)$	9.97
$e + O_2 \longrightarrow e + O + O^*(3P)$	14.7

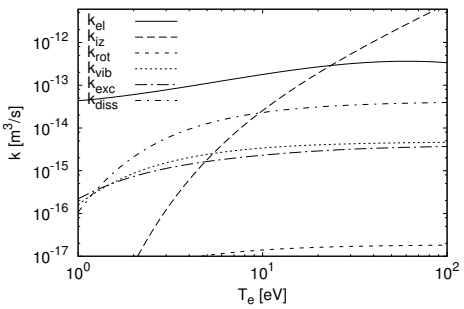

Figure A.5: Reaction rates for electron collisions in molecular oxygen.

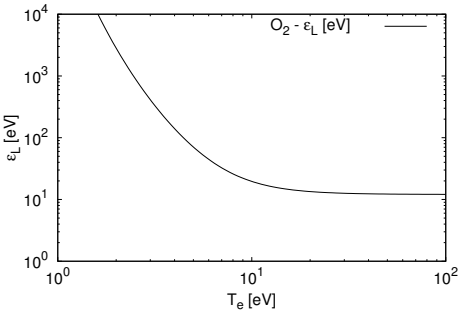

Figure A.6: Electron energy loss per electron-ion pair created in O_2.

APPENDIX B

Magnetic filter

B.1 Boris method

The system to be integrated is the following one:

$$\begin{cases} \frac{d\vec{x}}{dt} = \vec{v} \\ \frac{d\vec{v}}{dt} = \frac{q}{m}\left(\vec{E} + \vec{v} \times \vec{B}\right) \end{cases} \tag{B.1}$$

In order to obtain the correct solution, which conserves the energy over the orbits, velocity is displaced by a half time step with respect to the position and instead of updating the velocity from time "$n - 1/2$" to "$n + 1/2$" using the velocity at "$n - 1/2$", the average velocity at time "n" is used. The particle is then pushed from "n" to "$n + 1$" using the average velocity, which is the velocity at time "$n + 1/2$" [59]:

$$\begin{cases} \frac{\mathbf{x}^{n+1} - \mathbf{x}^n}{\Delta t} = \mathbf{v}^{n+1/2} \\ \frac{\mathbf{v}^{n+1/2} - \mathbf{v}^{n-1/2}}{\Delta t} = \frac{q}{m}\left[\mathbf{E} + \frac{\mathbf{v}^{n+1/2} + \mathbf{v}^{n-1/2}}{2} \times \mathbf{B}\right] \end{cases} \tag{B.2}$$

Firstly Boris noticed that in the velocity equation the electric field can be eliminated by defining two vectors $\mathbf{v}^-$ and $\mathbf{v}^+$:

$$\begin{cases} \mathbf{v}^{n-1/2} & = \mathbf{v}^- - \frac{q\mathbf{E}}{m}\frac{\Delta t}{2} \\ \mathbf{v}^{n+1/2} & = \mathbf{v}^+ + \frac{q\mathbf{E}}{m}\frac{\Delta t}{2} \end{cases} \tag{B.3}$$

When these definitions are substituted into the original equation, one obtains pure rotation:

$$\frac{\mathbf{v}^+ - \mathbf{v}^-}{\Delta t} = \frac{q}{2m}(\mathbf{v}^+ + \mathbf{v}^-) \times \mathbf{B} \tag{B.4}$$

An efficient way to solve this equation for $\mathbf{v}^+$ exists as explained is the following construction, which is part of the Boris method.

The angle through which the velocity will rotate in the given time step $\Delta t/2$ is:

$$\mathbf{t} \equiv \frac{q\mathbf{B}}{m}\frac{\Delta t}{2} \tag{B.5}$$

The vector $\mathbf{v}'$ bisecting the angle formed by the pre and the (to be yet computed) post-rotation velocity is:

$$\mathbf{v}' = \mathbf{v}^- + \mathbf{v}^- \times \mathbf{t} \tag{B.6}$$

This is perpendicular to both the magnetic field and the vector from $\mathbf{v}^-$ to $\mathbf{v}^+$. This connecting vector is again obtained from geometry as the cross product of $\mathbf{v}'$ and a new vector $\mathbf{s}$, which is $\mathbf{t}$ scaled to satisfy the requirement that magnitude of velocity remains constant in the rotation:

$$\mathbf{s} = \frac{2\mathbf{t}}{1+t^2} \tag{B.7}$$

so that $\mathbf{v}^+$ is obtained through:

$$\mathbf{v}^+ = \mathbf{v}^- + \mathbf{v}' \times \mathbf{s} \tag{B.8}$$

Once $\mathbf{v}^+$ is obtained, the final velocity is obtained through the second expression in (B.3): this is the velocity used to push the particle in space in (B.2).

Ringraziamenti

Tante sono state le persone che in questo periodo di tesi mi sono state accanto, ma un ringraziamento particolare voglio farlo prima di tutto alla mia famiglia: ai miei genitori, che hanno saputo amorevolmente prendersi cura di me sia materialmente che con i loro preziosi consigli, e a mia sorella, che anche nei momenti più critici è sempre riuscita a sollevarmi il morale. Un ringraziamento speciale va poi a Mauro, che mi è stato accanto con estrema pazienza anche in momenti in cui qualsiasi altra persona se ne sarebbe andata, e a tutti i miei amici, in particolare a Monica, che mi hanno sempre fatto sentire il loro sostegno dandomi la grinta per andare avanti.

Naturalmente un grande ringraziamento va anche a tutte le persone che ho conosciuto ad RFX, in particolare a coloro che mi hanno seguita più da vicino durante la mia tesi. Ringrazio in particolare il Dr. Gianluigi Serianni per il suo supporto e i suoi preziosi consigli, che mi hanno fatto crescere sia come fisica che come persona; un ringraziamento speciale va inoltre al Dr. Pierluigi Veltri, che è sempre stato estremamente disponibile e pronto a lasciare qualsiasi cosa stesse facendo per confrontarsi con me sulle problematiche che incontravo durante questa tesi; naturalmente voglio ringraziare anche il Dr. Marco Cavenago, che ha sempre saputo aprirmi prospettive inaspettate in occasione di ogni nostra discussione.

Un ringraziamento va anche al mio collega tesista Alessandro, con cui ho condiviso gioie e dolori dell'esperimento NIO, e a tutti i dottorandi, che mi hanno fatto sentire un po' una di loro, in particolare a Carlo che è sempre stato disponibile a darmi una mano. Insomma, ringrazio veramente tutte le persone che ho avuto l'onore di conoscere ad RFX, per le risate e per le conoscenze condivise, che hanno saputo rendere questo periodo di tesi veramente arricchente.